2022

Structural Studies of the Nucleolar Stages of Ribosome Biogenesis in Yeast

Linamarie Miller

Structural studies of the nucleolar stages of ribosome biogenesis in yeast

A Thesis Presented to the Faculty of
The Rockefeller University
in Partial Fulfillment of the Requirements for
the degree of Doctor of Philosophy

by
Linamarie Miller
June 2022

Structural studies of the nucleolar stages of ribosome biogenesis in yeast

Linamarie Miller, Ph.D.
The Rockefeller University 2022

The ribosome is the RNA-protein machine responsible for the essential task of translating mRNA into proteins. Ribosomes are heterodimers made up of a small subunit (SSU, 40S) and a large subunit (LSU, 60S). At the interface of these subunits, the mRNA is decoded by the small subunit and peptide bond formation is catalyzed by the rRNA of the large subunit. The cell therefore requires the timely and accurate assembly of functional ribosomal subunits, a complex process termed ribosome biogenesis.

In addition to the ribosomal RNAs and ribosomal proteins that make up the mature subunits, eukaryotic cells require over 200 trans-acting factors to assemble ribosomes. This process begins in the nucleolus- a subcompartment of the nucleus- where the ribosomal DNA is transcribed to produce pre-ribosomal RNAs (pre-rRNAs). The newly transcribed pre-rRNAs recruit many assembly factors essential to their early folding, but many of these factors exact roles were largely unknown at the start of this work. Additionally, as the rRNA forms the active centers of the ribosome, the initial steps of rRNA folding and chaperoning are of great interest. Structural biology studies have elucidated snapshots of later stages of assembly, but structural understanding of the very early stages of ribosome assembly were limited at the start of this work, and therefore our understanding of early assembly factor function and rRNA folding was restricted.

To gain insight into the earliest stages of large subunit assembly, we aimed to isolate and structurally characterize an early nucleolar stage of large subunit assembly. The structures of the nucleolar pre-60S provided insights into the roles of many nucleolus-specific assembly factors. Additionally, we observed that the pre-60S rRNA is largely disordered at this stage in assembly. The rRNA domains making up the solvent exposed side of the LSU are in a near-mature conformation, while the rRNA domains that will eventually form the active centers are largely disordered and prevented from folding (Chapter 2). Assembly factors enforce the open architecture of the rRNA while also preventing premature recruitment of later assembly factors. Initial findings towards the study of an even earlier stage of LSU assembly are also described here (Chapter 4).

Among the hundreds of assembly factors are several essential RNA helicases. Their functions and RNA targets are a particularly poorly understood aspect of ribosome biogenesis. One of the most well studied helicases necessary for small subunit assembly is Dhr1. Dhr1 is responsible for removing the U3 small nucleolar RNA (U3 snoRNA) from one of the earliest stable precursors of small subunit assembly called the SSU processome. Structures of the SSU processome revealed that the U3 snoRNA is a key architectural feature of this assembly

intermediate. Basepairing between the U3 snoRNA and the small subunit rRNA prevents folding between the subdomains of the SSU rRNA, ensuring they mature separately at this stage of assembly. Characterization of Dhr1 and its co-activator Utp14 in biochemical and structural studies has laid the foundation for understanding how the activity of this key enzyme is regulated (Chapter 3).

Overall, this work has contributed to the understanding of nucleolar stages of both small and large subunit biogenesis. The studies of the nucleolar pre-60S have elucidated the structures of several nucleolar specific assembly factors and revealed the architecture of early LSU rRNA folding. Biochemical and structural characterization of Dhr1 provided insight into how this RNA helicase is regulated in small subunit biogenesis. Together, these works have expanded our knowledge of the high level of control the cell exhibits over RNA folding and enzyme activity during the earliest stages of ribosome assembly.

Acknowledgments

I would first like to sincerely thank the Klinge Lab for being my scientific home for this project. The supportive and collaborative environment allowed me to learn so much and work through the ups and downs of structural biology studies. Thanks to Sebastian for his clever projects, quick thinking, kindness, and optimism. The first generation of the Klinge Lab welcomed me to Rockefeller. Mirjam, Jonas, Malik, Zahra, Camille, and Antoine made the beginning of my PhD so wonderful. I am so happy and honored to have Zahra as my co-author on the LSU story. I am also so glad to have had Malik as both a labmate and friend since my rotation.

The newer generation of Klinge Lab members, Sameer, Olga, Arnaud, Elizabeth, Chloe, Nathan, Rafal, and Anoosha, have also enriched my time here, and I will miss them greatly. I've been so lucky to share this time in the lab with you all!

I would also like to thank my committee: Seth Darst, Jue Chen, and Chris Lima. Their insight and kindness has been very helpful over the years. Special thanks to Seth and Liz for their kindness during my rotation in their lab and throughout the rest of my time here. Thank you also to John Woolford, for serving as my external examiner.

A special thanks to Deen Oren, for her patience and warmth while teaching me crystallography. I will miss our "fishing" sessions! Thank you to the wonderful team at the Cryo-EM- Mark, Johanna, and Honkit. Thank you to Milica Tesic Mark and Caitlin Steckler from the Proteomics facility. Many thanks to Kelly and Junjie and Brian Chait for working with us on crosslinking studies. Thanks also to the Walz and Hite labs for our discussions during joint lab meetings.

To the rest of the Old Lady Gang, Rachel and Emma, I am thankful that we got to go through this journey together.

I am so happy to have been part of TPCB, and to have gotten to know so many wonderful TPCB students. Thank you to the TPCB office for their support. Thank you also to Derek Tan- your dedication to TPCB was inspiring. Thanks to the Rockefeller Dean's office for all their help and guidance through my time here.

To all my friends from outside Rockefeller, I would not have made it through this PhD process without you and was blessed to have you nearby.

To my family, thank you for always encouraging me through school while also encouraging me to take time for myself when I needed it, and being there for me with food and hugs. Mom and Dad- I would not be where I am today without your love and support. To my sisters, I am immeasurably proud of you and I hope you are a little impressed with me! Uncle Mike- words cannot express how you grateful I am for your help on navigating basically everything! Marie Miller, the Miller matriarch, I think your stories of not being able to attend college really got to me and the twins! I hope you are proud of us.

Table of Contents

Abstract.....i
Acknowledgements.....iii
Table of Contents.....iv
List of Figures.....v
List of Tables.....vii
Chapter 1| Introduction
1.1 The ribosome.....1
1.2 Ribosome biogenesis.....6
1.2.1 Small subunit assembly.....9
1.2.2 Large subunit assembly.....15
1.2.3 Regulation of ribosome assembly.....18
1.3 RNA Helicases are essential for ribosome biogenesis.....19
Chapter 2| Structural characterization of the nucleolar pre-60S
2.1 Purification and Composition of nucleolar pre-60S.....31
2.2 Cryo-EM structure determination of several states of the nucleolar pre-60S.....33
2.3 Further information on nucleolar pre-60S assembly revealed by complementary structures.....43
Chapter 3| Structural and biochemical characterization of Dhr1 helicase and its activation by Utp14
3.1 Dhr1 contains a Dhr1-specific loop.....46
3.2 Biochemical studies of Utp14 activation of Dhr1.....61
Chapter 4| Preliminary studies of the Urb subcomplex and Urb subcomplex-containing pre-60S particle
4.1 Purification of the Urb subcomplex.....73
4.2 Purification and composition of the Urb particle.....76
Chapter 5| Discussion
5.1 The nucleolar pre-60S.....78
5.2 Capturing a 27SA containing pre-60S: The Urb particle/Urb subcomplex.....82
5.3 Dhr1 and Utp14.....83
5.4 The nucleolus: How is early assembly regulated in a membraneless organelle?.....88
5.5 Outlook.....91
Chapter 6| Methods
6.1 General methods 92
6.2 Methods specific to the study of the nucleolar Pre-60S.....95
6.3 Methods specific to the study of the Urb subcomplex/Urb particle.....98
6.4 Methods specific to the study of Dhr1 helicase and Utp14.....100
Chapter 7|Appendix.....105
Chapter 8| References.....110

List of Figures

Figure 1.1 Overview of the eukaryotic ribosome
Figure 1.2 Overview of the eukaryotic small subunit architecture.
Figure 1.4 Schematic of a rDNA locus.
Figure 1.5 Summary of rRNA processing throughout ribosome biogenesis.
Figure 1.6 Co-transcriptional recruitment of assembly factors and formation of the SSU processome
Figure 1.7 Open architecture of the pre-18S rRNA in the SSU processome
Figure 1.8 Cytoplasmic stage of assembly of the pre-small subunit
Figure 1.9 Recruitment of assembly factors at the beginning of large subunit assembly
Figure 1.10 Architecture of the late nucleolar Nog2 particle
Figure 1.11 Motifs of the SF2 family of helicases
Figure 1.12 Overview of DEAD-box helicases
Figure 1.13 Overview of DEAH-box helicases.
Figure 1.14 Overview of conformational changes within the Prp43 helicase core caused by nucleotide and RNA binding
Figure 1.15 Two distinct conformations of the Dhr1 helicase core observed in crystal structures
Figure 2.1 Purification of the 27SB containing pre-60S
Figure 2.2 Negative stain analysis of the nucleolar pre-60S
Figure 2.3 Cryo-EM studies of the nucleolar pre-60S reveal a well resolved core with flexible auxiliary domains
Figure 2.4 Analysis of the cryo-EM data of the nucleolar pre-60S reveals several distinct states
Figure 2.5 Cryo-EM density fit of selected assembly factors
Figure 2.6 rRNA domains of state 2, state 3, and the mature 60S ribosomal subunit
Figure 2.7 A ring of nucleolar assembly factors prevents premature folding of the 25S rRNA
Figure 2.8 State 3 reveals an aspect of control over exosome recruitment to the pre-60S
Figure 2.9 Nucleolar pre-60S structures reveal different intermediates of the polypeptide exit tunnel
Figure 2.10 Schematic of the various states of the pre-60S observed in our work and Kater et al.'s work
Figure 3.1 The Dhr1-loop is conserved among Dhr1 homologs but not other DEAH-helicases
Figure 3.2 Structure of yeast Dhr1 helicase core reveals a loop that occupies the substrate-binding cleft
Figure 3.3 Residues from the RecA1, RecA2, and Ratchet-like domains interact with the loop directly or via coordinating waters
Figure 3.4 The Dhr1-specific loop confers an "open" state to the helicase
Figure 3.5 The Dhr1 specific loop is not essential to cell viability, while the Dhr1 CTD is
Figure 3.6 Dhr1 visualized in context in maturing small subunit processomes from yeast
Figure 3.7 Dhr1 observed in states Post-A1, Dis-A and Dis-B is in the loop-bound conformation
Figure 3.8 Dhr1 and Utp14 binding sites in the maturing SSU processome
Figure 3.9 The binding site for Utp14 is occupied by the 5'ETS before the action of the exosome
Figure 3.10 Identification of a more minimal segment of Utp14 responsible for Dhr1 activation

List of Figures (cont.)

Figure 3.11 Strand displacement assays reveal the minimal segment of Utp14 for activation
Figure 3.12 The activating segment of Utp14 is sequestered between Utp7 and Utp1
Figure 3.13 Regulation of Utp14 binding in maturing SSU processomes is conserved from yeast to humans
Figure 3.14 Several key Dhr1 interactions are conserved in human maturing SSU processomes
Figure 3.15 Structure of the more complete auto-inhibited Dhr1 helicase
Figure 4.1 Preliminary work towards purification and structural characterization of the Urb subcomplex
Figure 4.2 Preliminary work towards purification and structural characterization of the Urb particle
Figure 5.1 Model of pre-60S maturation in the nucleolus
Figure 5.2 Utp14 and Dhr1 are tightly controlled in maturing SSU intermediates to tune Dhr1 helicase activity
Figure 5.3 Prp2 helicase in complex with RNA and its co-activator, Spp2

List of Tables

Table 1.1 List of RNA helicases involved in *S. cerevisiae* ribosome biogenesis.
Table 3.1 Table 3.1 Nomenclature used for Dhr1 and Utp14 constructs.
Table 6.1 Plasmids used to generate affinity tags for endogenous yeast tagging.
Table 6.2 Table 6.2 Yeast strains generated for this work.
Table 6.3 Table 6.3 Northern Blot Probes.
Table 6.4 Plasmids used to determine the viability of Dhr1 constructs.
Table 6.5 Cloning, expression and purification of Dhr1 and Utp14 constructs for crystallography and biochemical assays.
Table 6.6 Sequence for RNA and DNA oligos utilized in the RNA strand displacement assay.
Table 7.1 Cryo-EM data collection parameters and refinement and validation statistics for the nucleolar pre-60S.
Table 7.2 Molecular models of the nucleolar pre-60S.
Table 7.3 Refinement statistics for the auto inhibited Dhr1 core bound to ADP.
Table 7.4 Refinement statistics for auto-inhibited Dhr1CTD at the time of writing.
Table 7.5 Mass spectrometry results from purified Urb particles and purified Urb subcomplexes.

Chapter 1: Introduction

1.1 The ribosome

Living organisms must maintain and express the information stored in their genomes. At the cellular level, these processes are maintained by DNA, RNA, and protein molecules. The information in the genome is stored as DNA, which is replicated by DNA polymerases. The information in the genome is transcribed by RNA polymerases into messenger RNAs (mRNAs), and the translation of mRNAs into proteins completes the transfer of information from the genome to the entirety of the cell. This scheme is referred to as the central dogma of molecular biology (Crick, 1958). The act of translation of mRNAs into proteins is accomplished by the molecular machinery called the ribosome. Every living organism relies on the timely and accurate function of the ribosome to generate proteins and complete the transfer of information from the genome. Therefore, understanding of the workings of the ribosome is a key component of understanding basic cellular function.

The ribosome was first identified in micrographs of various animal cells as a "small particulate component" by George E. Palade in 1955 (Palade, 1955). Great effort was put towards the study of this molecular machine, with great breakthroughs accomplished by the first structures of prokaryotic ribosomes (Ban et al., 2000; Clemons et al., 1999) and eventually eukaryotic ribosomes (Ben-Shem et al., 2011; Klinge et al., 2011; Rabl et al., 2011). These structures revealed the 3D architecture of these RNA-protein complexes and their functional sites. They also confirmed that the ribosome was in fact a ribozyme, as proposed by Noller, Hofferarth, and Zimniak in 1992 (Noller et al., 1992).

As it was observed in early biochemical studies and confirmed in these structural studies, the ribosome is composed of two subunits: the small subunit (SSU) and large subunit (LSU). At the interface of the two subunits, peptide bond formation occurs and mRNA and tRNA bind and transit through the molecular machine (**Fig 1.1**). The SSU is responsible for binding mRNA at this interface, and is responsible for assessing the complementarity between incoming transfer RNA (tRNA) anticodons and the mRNA substrate. This is a process called "decoding" and the occurs at the "decoding center" on the small subunit. The large subunit is responsible for catalyzing the formation of the peptide bond between the amino-acyl moieties on transfer RNAs (tRNAs), and therefore creating polypeptides. The nascent polypeptide chain exits the ribosome through the polypeptide exit tunnel, a feature of the large subunit that begins near the site of peptide bond formation and ends on the solvent exposed side of the large subunit.

The cycle of translation in yeast, which is largely conserved from bacteria to humans, is described briefly here, and reviewed in great detail by Dever, Kinzy, and Pavitt (Dever et al., 2016). To begin translation, the SSU must bind a ternary complex made of the initiation methionine tRNA, and GTP-bound initiation factor eIF2. Several other factors join the 40S and the ternary complex to form the Pre-Initiation Complex, which then binds near the 5' end of an mRNA transcript and scans to find an AUG start codon. When the start site is selected, GTP hydrolysis by eIF2 occurs and releases many of the initiation factors. This release allows for the binding of the LSU, the formation of the 80S, and the start of the elongation cycle. Elongation factor eEF1 delivers an amino-acylated tRNA to the A site of the ribosome. When the codon complements the sequence of the mRNA in that site, GTP hydrolysis by eEF1 causes its release, and allows the tRNA to be fully accommodated in the A site. Here, peptide bond formation can

be catalyzed between the amino acids held at site A and P by the peptidyl transferase center of the LSU. The 60S then swivels relative to the 40S, a process referred to as “ratcheting”, moving the tRNAs amino-acid-binding ends into the P- and E-sites, while the anti-codon portions remain in the A- and P- sites. Elongation factors then bind the ribosome, hydrolyze GTP, and promote translocation, as the anti-codons of the tRNA move into the P- and E-sites, moving the mRNA one codon forward along with them. The tRNA in the E-site then exits the ribosome, and the elongation cycle can continue (**Fig 1.1**).

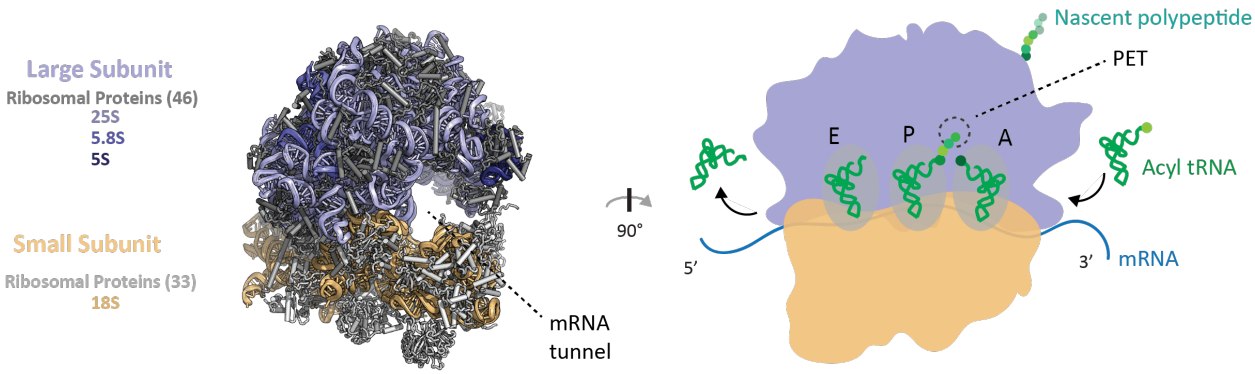

Figure 1.1 Overview of the eukaryotic ribosome. The eukaryotic ribosome is made of a large and small subunit (PDB 4V88). mRNA traverses the ribosomes via the mRNA tunnel. Acyl tRNAs enter the ribosome, are decoded by the small subunit, and bind in the A, P, and E sites. The large subunit forms the polypeptide chains which exit through the polypeptide exit tunnel (PET).

The ribosome is a ribozyme, so the rRNA forms the basis of the previously described key features of the ribosome. The small subunit (40S) contains only one rRNA, the 18S. The 18S can also be subdivided into subdomains, the 5’, the central, the 3’ major, and the 3’ minor (**Fig 1.2A**). The 5’, central, and 3’ minor domains form many inter-domain contacts and form the body of the small subunit, the subunit interface of which binds mRNA and tRNA. The 3’ major domain makes up the head of the small subunit (**Fig 1.2B,C**). The arrangement of the SSU rRNA domains is organized in part by the folding of the central pseudoknot between the 5’ and 3’ major domains. The junction of the head and body of the small subunit creates the pocket for the mRNA, and the decoding center is also located here where the 3’ minor domain meets the 3’ major domain (**Fig 1.2B,C**).

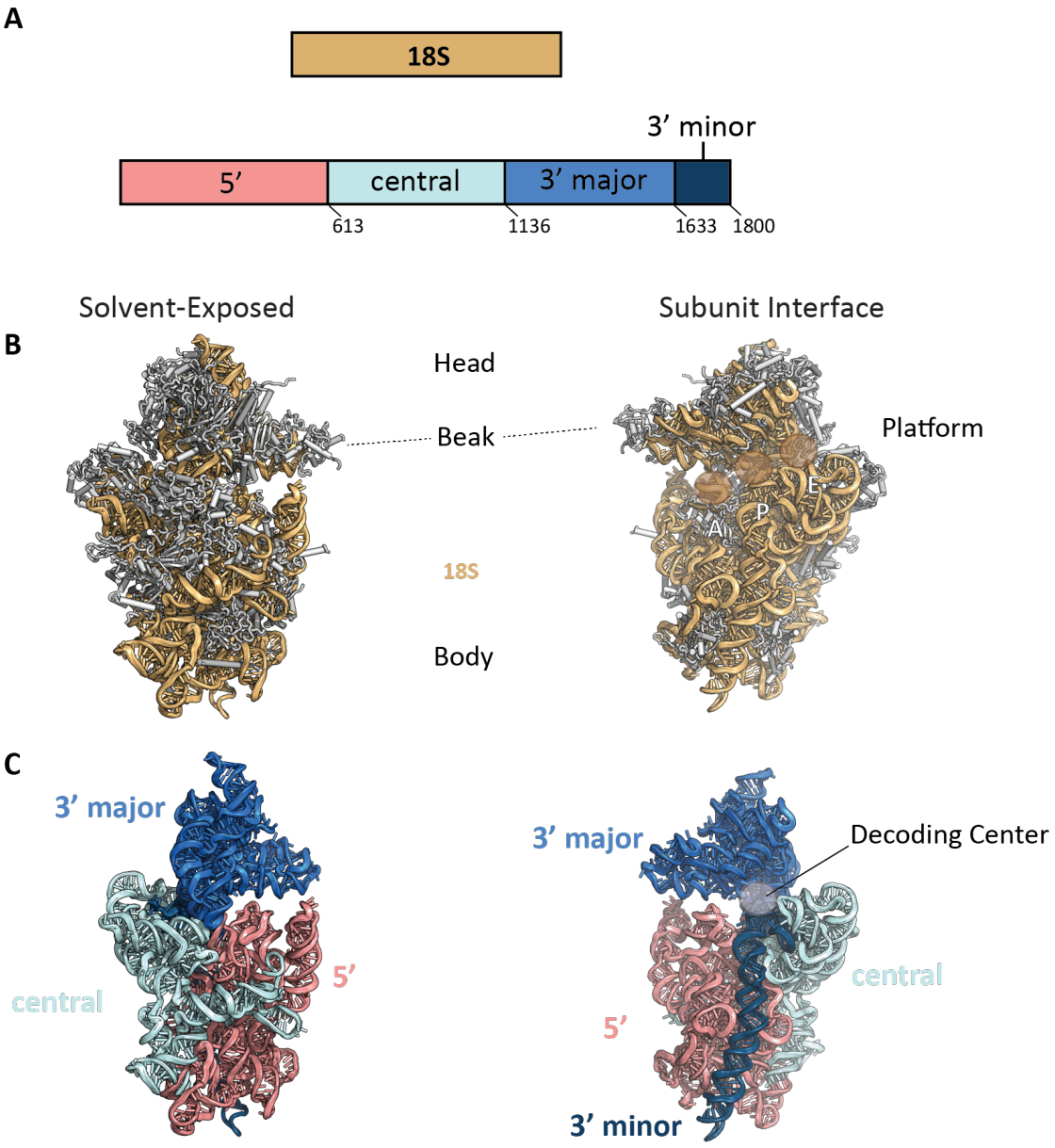

Figure 1.2 Overview of the eukaryotic small subunit architecture. **A**) The 18S is subdivided into four subdomains called the 5', central, 3' minor, and 3' major. This color scheme is used throughout this work. **B**) The SSU with the 18S in orange and the ribosomal proteins in gray, with views of the solvent exposed side and the side that interfaces with the large subunit. **C**) The same views presented in B, but only focusing on the 18S rRNA, which has been recolored to show the arrangements of the subdomains introduced in A. (PDB 4V88)

The eukaryotic large subunit (60S) contains three rRNA species, the 25S, the 5.8S, and the 5S. The 25S can be subdivided into six structural subdomains, I-VI (**Fig 1.3A**). The A, P, and E sites along with the peptidyl transferase center are formed by domain V on the subunit interface of the particle (**Fig 1.3B,C**). The entrance to the polypeptide exit tunnel is located between the A and P sites. The solvent exposed side of the LSU is largely made by domains I, II and the 5.8S. Here, the end of the polypeptide exit tunnel is made by domains I, III, and the 5.8S. Domains III and VI bridge the solvent exposed side and the subunit interface of the LSU. The 5S rRNA is the RNA component of the central protuberance, which binds atop segments of domains II and V (**Fig 1.3B,C**).

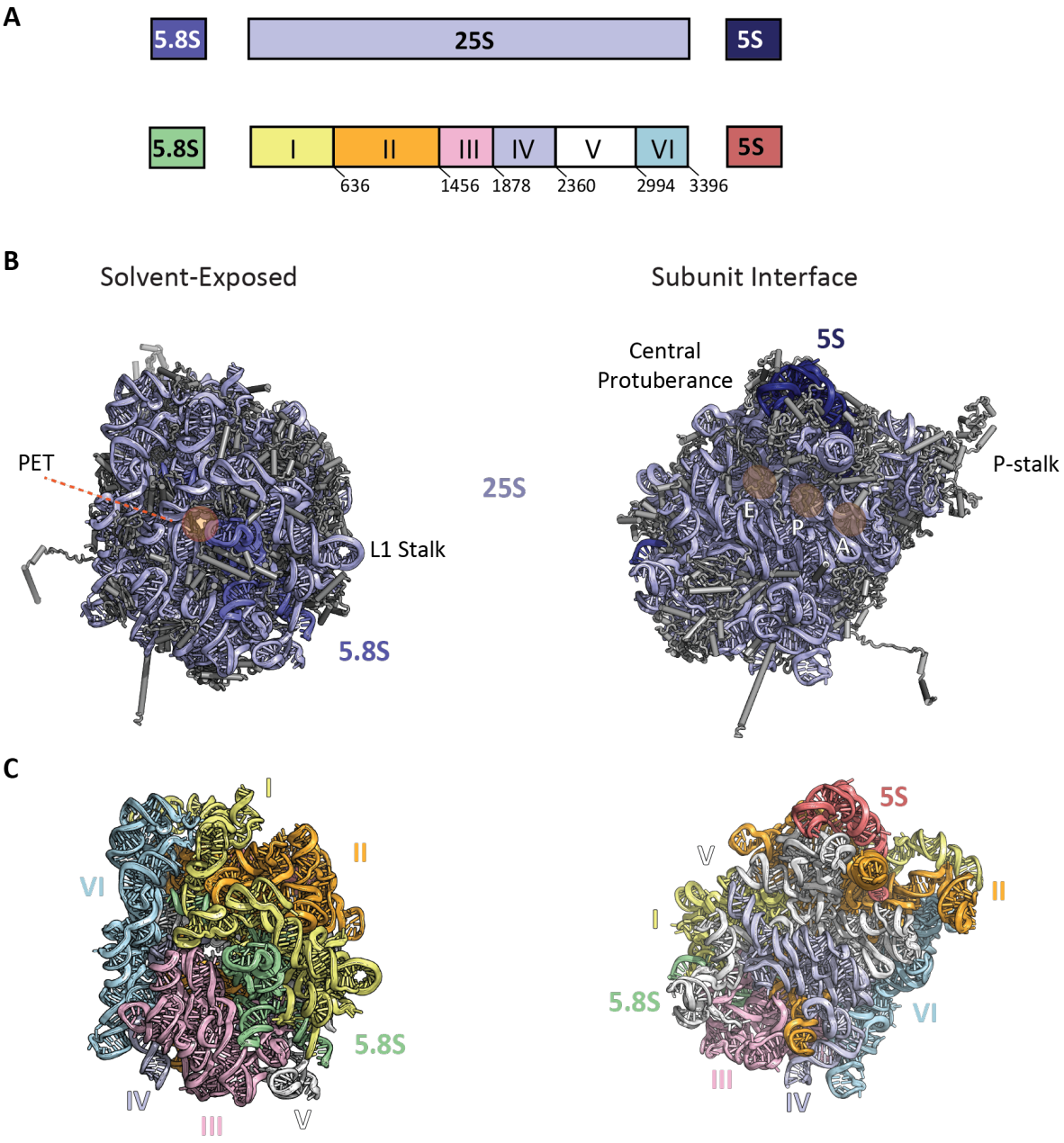

Figure 1.2 Overview of the eukaryotic small subunit architecture. **A**) The 25S is subdivided into six subdomains, I- VI. The 5.8S and 5S are also recolored for clarity in certain figures. This color scheme is used throughout this work. **B**) The LSU with the 25S, 5.8S, and 5S in shades of purple and the ribosomal proteins in gray, with views of the solvent exposed side (left) and the side that interfaces with the small subunit, in the "crown view" (right). **C**) The same views presented in B, but only focusing on the rRNA, which has been recolored to show the arrangements of the subdomains introduced in A. (PDB 4V88)

With an understanding of the basic function and architecture of the ribosome, we can now approach the overarching question of this work: how do eukaryotic cells assemble the complex protein and RNA machinery of the ribosome?

1.2 Ribosome biogenesis

The process of assembling the ribosomal proteins and rRNA into functional ribosomes is referred to as ribosome biogenesis or ribosome assembly. This work will focus on ribosome assembly in *Saccharomyces cerevisiae*, as it can be argued that study of this process has been the most well characterized in yeast. Therefore, in the following sections the proteins and rRNA nomenclature will be that from *S. cerevisiae* unless otherwise noted.

Eukaryotic ribosome biogenesis is a complex process spanning three cellular compartments that requires over 200 trans acting factors in addition to the rRNA and ribosomal proteins present in the mature ribosome. Ribosome biogenesis begins in the nucleolus, a non-membrane bound subcompartment of the nucleus defined by active ribosome assembly. Here, RNA polymerase I and III transcribe the ribosomal DNA (rDNA), which is organized in rDNA repeats located within chromosome XII of the yeast genome (**Fig 1.4**). There are approximately 100-200 of these repeats in the average yeast cell, and each repeat contains all the information for a complete set of rRNA. The segments of mature rRNA sequences are flanked by External Transcribed Spacers (ETSs) and separated by Internal Transcribed Spacers (ITSs). The rDNA repeats are separated from one another by Non-Transcribed Spacers (NTSs). RNA polymerase III is responsible for transcription of the 5S rRNA, while RNA polymerase I transcribes the 18S, 25S, 5.8S, and transcribed spacer regions. The whole RNA polymerase I transcript is referred to as the 35S (**Fig 1.4**).

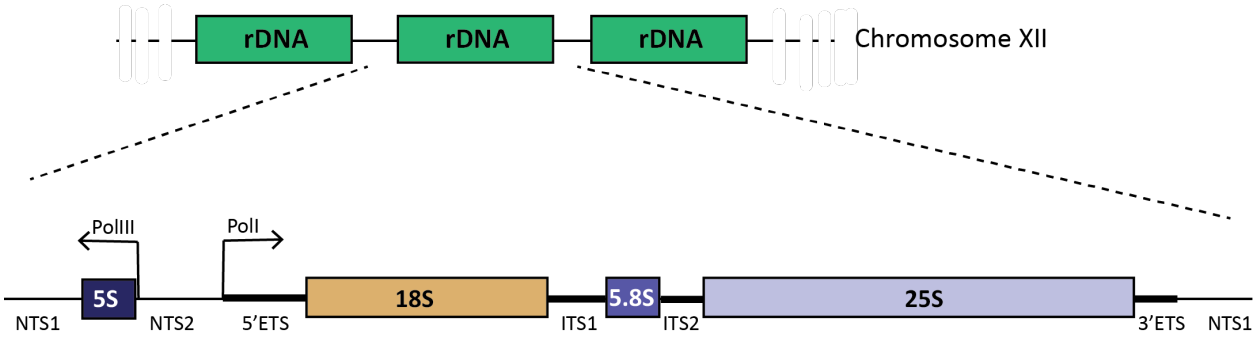

Figure 1.4 Schematic of a rDNA locus. The rDNA repeats are located on chromosome XII in *S. cerevisiae*. Each repeat contains the information for the rRNA and External Transcribed Spacers (ETS) and Internal Transcribed Spacers (ITS). Non-transcribed spacers separate repeats from one another. RNA polymerase I (PolI) transcribes the 18S, the 5.8S, and the 25S, while the 5S is transcribed by RNA polymerase III (PolIII).

However, the action of ribosome assembly factors does not wait for the complete transcription of the 35S. That is to say the very beginning of ribosome biogenesis is a co-transcriptional process. Several key cleavage events within the 35S can or must occur co-transcriptionally. Cleavage events at sites A0, A1, and A2 occur co-transcriptionally, while post-

transcriptional processing involves cleavage at site A3 by the RNAse MRP complex (Lygerou et al., 1996) Large and small subunit maturation is essentially separated after processing within ITS1 (**Fig 1.5**). Cleavage at A1 and A2 is likely performed by Utp24, but the identity of the nuclease for A0 cleavage remains unknown (Tomecki et al., 2015; Wells et al., 2016). Interestingly, co-transcriptional cleavage at site A2 only occurs after transcription has reached domain I or II of the 25S rDNA region, so cleavage here can be co-transcriptional, but not co-incident with transcription (Kos & Tollervey, 2010). In wild type cells, about 70% of these early cleavage events occurs co-transcriptionally (Kos & Tollervey, 2010). Under stress conditions, yeast cells shift to a greater likelihood of post-transcriptional cleavage at cite A3. This creates the 23S rRNA precursor, of which the biological significance remains unknown (Kos-Braun et al., 2017; Talkish et al., 2016). Another co-transcriptional cleavage is the end of rRNA transcription at site B0, where cleavage by Rnt1 releases the 35S or 27SA2 transcript (Kufel et al., 1999). Other key cleavage events happen exclusively post-transcriptionally and are discussed in the context of each subunits' assembly in Chapters 1.2.1 and 1.2.2. Cleavages of the rRNA throughout assembly are well-regulated and irreversible steps in the biogenesis process. The steps of pre-rRNA processing throughout the cell are summarized in **Figure 1.5.**

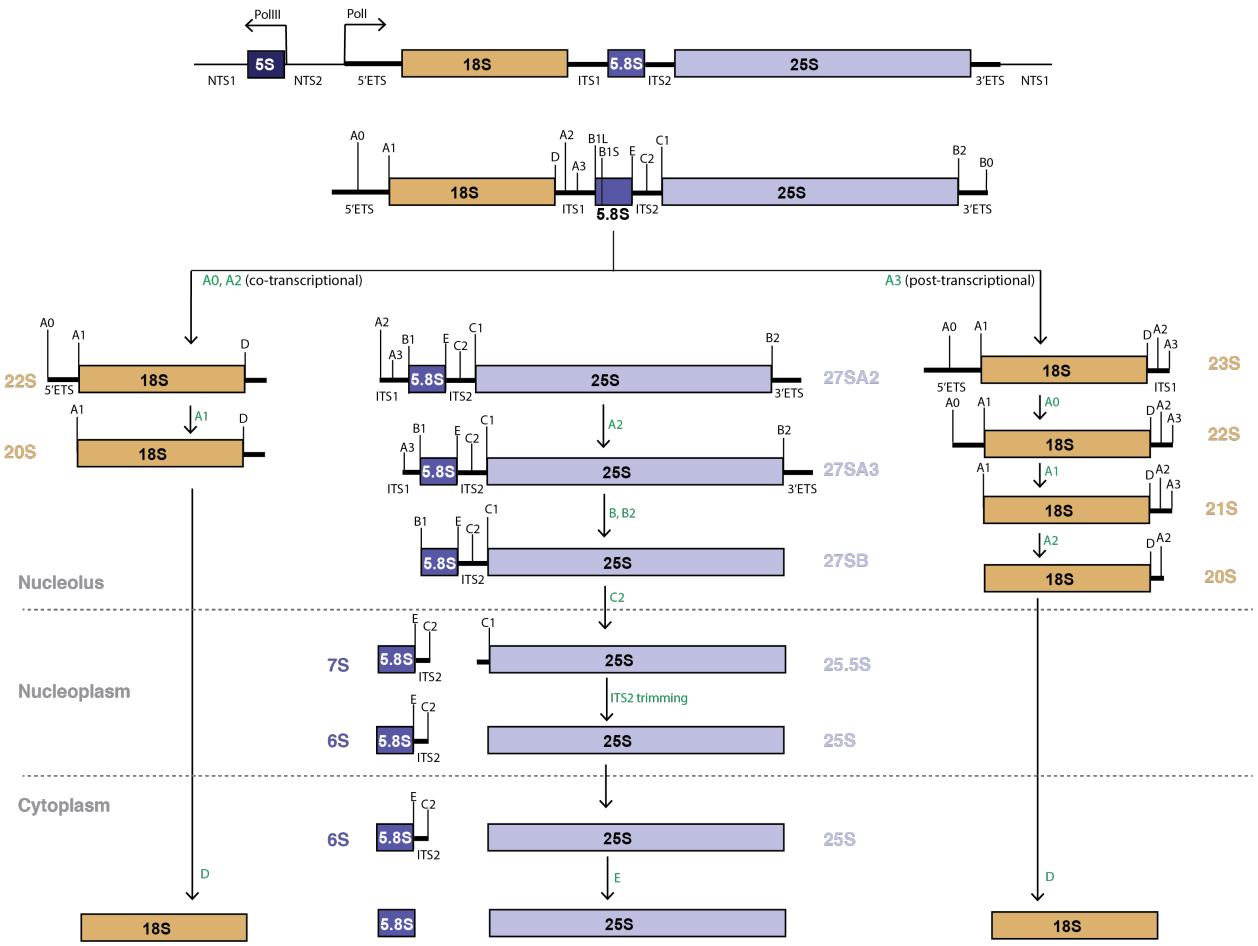

Figure 1.5 Summary of rRNA processing throughout ribosome biogenesis. Processing and cleavage of the pre-rRNAs are key and irreversible steps in ribosome assembly. Cleavage events are highlighted in green text. The corresponding names of the pre-rRNA species are in orange or shades of purple to the side of the pre-rRNA

The processing and cleavage of the pre-rRNAs takes place in the context of pre-ribosomal particles. The nascent rRNA is sufficient to recruit very early assembly factors that will work to chaperone, fold, and process the rRNA and form pre-ribosomal complexes. These particles were visualized decades ago, when Miller and Beatty's micrographs of actively transcribed rDNA revealed terminal knobs on nascent rRNA (Miller & Beatty, 1969). These were recognized as pre-ribosomal particles many years later in 1993 (Mougey et al., 1993). Our understanding of ribosome assembly and the identity and function of assembly factors has expanded greatly since then, with a vast foundation of work utilizing the power of yeast genetics to identify and understand the interaction networks of assembly factors using biochemistry, and affinity purifications coupled with mass spectrometry (Woolford & Baserga, 2013).

The trans-acting factors include non-enzymatic chaperone proteins, GTPases, methylases, RNA helicases (RNA helicases are expanded on in Chapter 1.3), and small nucleolar RNAs (snoRNAs). SnoRNAs are capable of modifying the rRNA. Box C/D snoRNAs form a complex with several proteins (Nop58, Nop56, and two copies each of Nop1, and Snu13) and can direct 2'-O-methylation of the RNA. Nop1 is the methyltransferase, while the snoRNA directs the site of Box C/D complex binding. Box H/ACA snoRNAs can direct psuedouridylation and form a snoRNA protein (snoRNP) complex with two copies each of Gar1, Cbf5, Nop10, and Nhp2. Cbf5 is the catalytic subunit of the Box H/ACA snoRNP. Modifications serve to stabilize rRNA folding and cluster at the active sites of the ribosome. Although not strictly essential, removal of multiple modifications from a cluster of modifications at a functional site can show severe negative cell phenotypes (reviewed in (Sloan et al., 2017). The most abundant, and the most well studied, snoRNA is the U3 snoRNA. It is essential for cell viability, and does not direct any methylation of its target RNA. The importance of the U3 snoRNA is expanded in section 1.2.1 Not all rRNA modifications are directed by snoRNAs. For example, Bud23 (White et al., 2008) and Emg1 (Leulliot et al., 2008) can direct methylation of the small subunit rRNA.

Most recently, using the detailed genetic and biochemical information available in combination with the breakthroughs in cryo-electron microscopy (cryo-EM), we now have many snapshots of the molecular architecture of intermediates in pre-ribosome assembly. These have allowed high resolution details of how the myriad of components within these pre-ribosomal particles function together to create mature ribosomes. Several major themes in ribosome biogenesis have emerged from these structural studies. First, cleavage events are highly-regulated and irreversible steps in the assembly process. Next, the solvent exposed portions of the subunits mature earlier in the biogenesis process than the subunit interfaces. The solvent exposed sides of the subunits serve as platforms for assembly factors to gradually form and protect the ribosomal active sites. Lastly, assembly factors prevent premature association of pre-40S and pre-60S subunits, and assess the completeness of ribosomal subunits during the final stages of assembly in the cytoplasm.

1.2.1 Small subunit assembly

The beginning of the understanding of small subunit biogenesis was pioneered by work which identified the U3 snoRNA and other assembly factors necessary for SSU assembly that are localized to the nucleolus. More detailed tandem affinity purification coupled with mass spectrometry work identified what was termed the small subunit processome (SSU processome), the abundant nucleolar pre-small subunit particle (Dragon et al., 2002). This giant 6 MDa particle contains over 30 assembly factors, several ribosomal proteins, the U3 snoRNA, the 5' ETS, and the 20S/21S/22S pre-rRNA. The recruitment of these components begins with the transcription of the 5' ETS. The 5' ETS is sufficient to recruit the UtpA subcomplex, the U3 snoRNP, UtpB subcomplex, the Mpp10 subcomplex, and several other nucleolar factors. These proteins form the base of the very early pre-SSU, and this pre-ribosomal particle is referred to as the 5' ETS particle (Chaker-Margot et al., 2015; Hunziker et al., 2019). Transcription of the domains of the 18S rRNA recruit more and more early assembly factors and the very first ribosomal proteins (Chaker-Margot et al., 2015). Work expressing fragments of the 18S in yeast has shown that each subdomain of the 18S is sufficient to recruit several assembly factors, including some very transient factors that exit the assembly process before the 18S is fully

transcribed. These subdomains exist as independent modules until transcription of the 18S is complete and the subdomains of the small subunit coalesce to form the SSU processome, the first stable precursor of small subunit assembly (Chaker-Margot et al., 2015; Hunziker et al., 2019) (**Fig 1.6**).

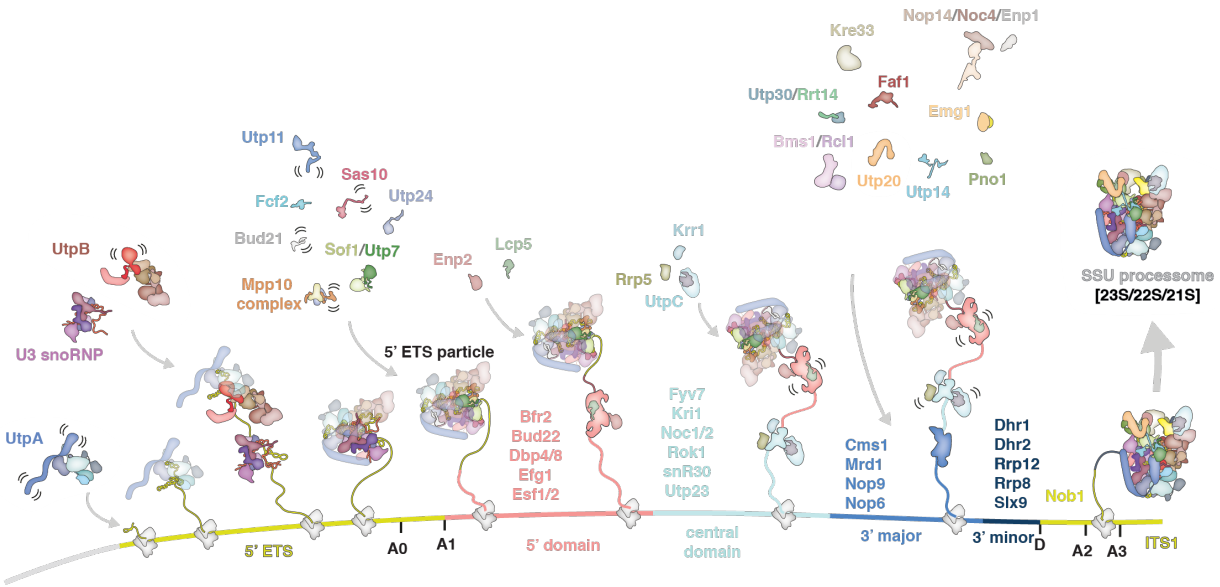

Figure 1.6 Co-transcriptional recruitment of assembly factors and formation of the SSU processome. Diagram of recruitment of assembly factors by each subdomain of the 18S based on mass spectrometry studies from (Chaker-Margot et al., 2015) and (Hunziker et al., 2019). Factors that are visualized in the SSU processome are show in various colors with cartoons of their structure within the processome. Factors recruited by each subdomain that are either disordered or exit the particle before the formation of the SSU processome are written near the portion of the pre-18S that's transcription is responsible for their recruitment.

Structures of the small subunit processome purified from *Saccharomyces cerevisiae* and *Chaetomium thermophilum* have provided great insight into the architecture of these massive pre-ribosomal particles (Chaker-Margot et al., 2017; Barandun et al., 2017; Q. Sun et al., 2017; Kornprobst et al., 2016; Cheng et al., 2017). This work will focus on the most complete structure of the SSU processome from yeast (Barandun et al., 2017). The "base" of the particle is formed by the 5' ETS and the UtpA complex. From the base, the different subdomains of the 18S extend into their own portions of the particle, and do not yet form the tertiary contacts that are important to mature small subunit function (**Fig 1.7A**). This separation of the subdomains is supported by the binding of the U3 snoRNA to the 18S, which prevents these inter-domain contacts and prevents folding of the central pseudoknot (**Fig 1.7B**). The UtpB complex supports the base and side of the particle, while several long, flexible proteins (Mpp10, Utp11, and Sas10) interconnect distant regions of the structure. The rest of the surface of the SSU processome is in part supported by large helical repeat proteins like Nop14, Rrp5, Utp10 (part of UtpA), and Utp20. Several enzymes feature as key architectural components in the particle, but not all of their enzymatic activities are strictly required. The GTPase Bms1 connects the 5' and 3' major domains of the pre-18S and its GTPase activity is essential for cell viability

(Weigierski et al., 2001). The acetyltransferase Kre33 is essential for pre-40S assembly and cell viability, but its acetylation is not strictly essential (Sharma et al., 2015; Sharma et al., 2017). Similarly, the pseudouridine methyltransferase activity of the factor Emg1 is not essential, but its presence in the SSU processome is (Leulliot et al., 2008; Thomas et al., 2011). Other enzymes that are part of the SSU processome are not in proximity to their substrates in the SSU processome structures. The nuclease Utp24 is responsible for A1 and A2 cleavage (Bleichert et al., 2006; Wells et al., 2016), but its active site is not located near the A1 cleavage site in these structures. Similarly, the helicase Dhr1 is necessary for the removal of the U3 snoRNA (Sardana et al., 2014), and although cross-linking data and mass spectrometry data indicated that Dhr1 is recruited to the SSU processome, it is not visualized. It was also unclear how Dhr1 could access the substrate U3 snoRNA in the current structures. Structural data released over the course of this work have helped reveal how the next stages in small subunit assembly allow these enzymes to access their substrates. The next stages of small subunit assembly necessitate removal of the 5' ETS RNA, cleavage at A1 by Utp24, removal of the U3 snoRNA, and disassociation of early assembly factors that have completed their roles. The ETS is degraded by the nuclear exosome and the implications of structures of the exosome acting upon the pre-SSU will be discussed here. Removal of the U3 snoRNA requires the action of the RNA helicase Dhr1, which is discussed in greater detail in Chapter 1.3 and Chapter 3.

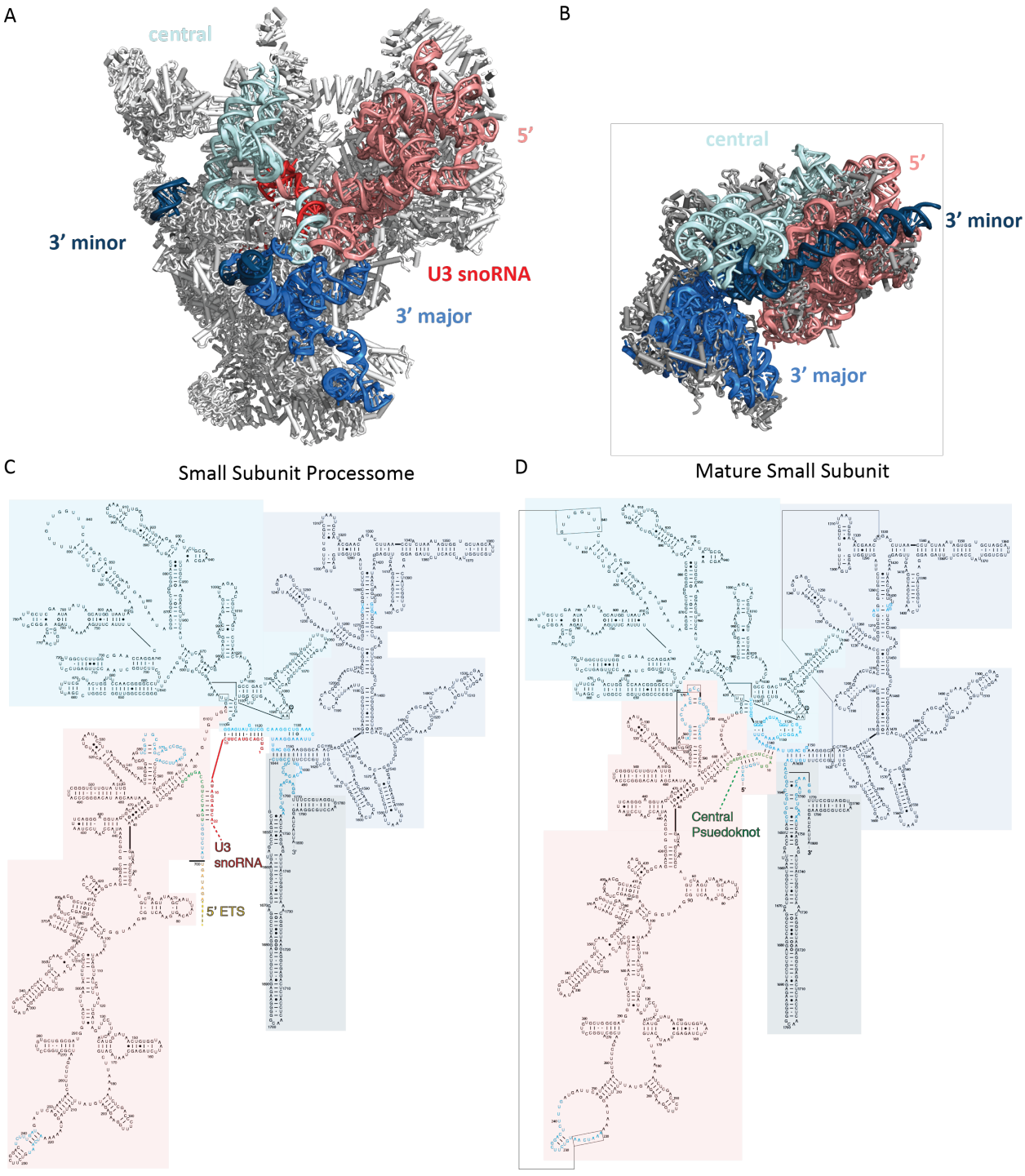

Figure 1.7 Open architecture of the pre-18S rRNA in the SSU processome. A) RNA in the SSU processome (PDB 5WLC) colored by subdomain as in Figure 1.2. Here, the RNA is overlaid on the overall SSU processome structure and the 3' portion of the U3 snoRNA has been removed for clarity. **B**) RNA architecture in the mature small subunit (PDB 4V88). **C**) Diagram of the rRNA in the SSU processome. **D**) Diagram of the rRNA in the mature small subunit. C and D) Portions of the rRNA that are different between the mature SSU and SSU processome are in blue text.

The structures of the exosome bound to maturing SSU processomes confirmed the site of interaction between these two large complexes, but there are still many open questions about exactly how the 5' ETS is processed by the exosome and exactly what triggers this processing (Du et al., 2020; Lau et al., 2021). In both bodies of work, the nuclear exosome complex is recruited to the pre-ribosome via binding of the helicase Mtr4. Mtr4 has a binding surface near Utp6, Utp14, Fcf2, and Utp18. The atomic details of this interaction remain unclear due to limiting resolution. Additionally, although Utp18 contains the Arch Interacting Motif (AIM) that has been shown to be important for binding to the Arch motif of Mtr4 (Thoms et al., 2015), this portion of Utp18 was not visualized in any available structures. Two other assembly factors, Sas10 and Lcp5, have been implicated in exosome recruitment, as they contain domains that, when part of other proteins, interact with the Rrp6 nuclease of the exosome (Mitchell, 2010). But, a direct association between Sas10 or Lcp5 with exosome recruitment remains unclear. The activity of the exosome destabilizes the 5'ETS, triggering rearrangements in the pre-40S that allow Utp24 nuclease to access the A1 cleavage site. Further dissociation of the 5'ETS and of the UtpA and UtpB complexes allows for the action of Dhr1 to remove the U3 snoRNA (Cheng et al., 2020), which is discussed in greater detail in chapter 3.

After the major rearrangements to disassemble the SSU processome caused by A1 cleavage and the removal of both the 5'ETS and the U3 snoRNA, some early assembly factors remain as part of the pre-40S (Rrp12, Enp1, Pno1, and the nuclease Nob1). Other factors bind in the nucleus to aid with further maturation and cytoplasmic export (Ltv1, Tsr1, Dim1, Rio2). Nuclear export of pre-SSUs is a RanGTP-dependent and Crm1 dependent process (reviewed in Peña, Hurt, & Panse, 2017). Rio2 and Ltv1 have nuclear export signals in their C-termini that are hypothesized to recruit Crm1 and RanGTP. Ltv1 is non-essential in yeast, but depletion of Ltv1 causes a reduction in the efficient export of small subunits (Seiser et al., 2006). In vitro studies have found evidence for complex formation between Rio2, RanGTP, and another assembly factor Slx9 (Fischer et al., 2015). In humans, studies have revealed hRio2 is not strictly required for export (Zemp et al., 2009). Together, these imply that there may be at least two complementary mechanisms to ensure efficient export of pre-40S subunits into the cytoplasm.

Structural studies of cytoplasmic pre-40S reveal the arrangement of these proteins after export to the cytoplasm (Heuer et al., 2017; Johnson et al., 2017; Mitterer et al., 2019; Scaiola et al., 2018). Rrp12 is not visualized in these structures, but Rrp12 is important for efficient nuclear export (Moriggi, Nieto, & Dosil, 2014). In the pre-40S structures Enp1 and Pno1 associate with the 3' major domain of the rRNA, in the head region of the SSU (**Fig 1.8**). These structures also reveal information about a number of assembly factors that associated with the pre-40S in the cytoplasm- these are Ltv1, Tsr1, Rio2, and Dim1 (**Fig 1.8**). Ltv1 binds where the early factor Nop14 was bound near Enp1. Ltv1 now works with Enp1 to block rps10 binding which is required for formation of the beak structure in the mature SSU. Enp1, Ltv1 and uS3 form a premature beak structure in these early cytoplasmic particles on the solvent exposed side of the pre-40S. This stops the binding of translation factors and stops premature translation initiation. Dim1, Rio2, and Tsr1 are also positioned on the subunit interface, preventing premature interaction with mature large subunits or the initiation factor eIF1A. Tsr1 occupies the former binding site of Bms1, and although similar in fold, Tsr1 is catalytically inactive (Gelperin et al., 2001; Wegierski et al., 2001). Further, Tsr1 binding may block the binding of Fun12 and Rio1, two enzymes required for the very final steps of SSU assembly. Pno1

is bound near the 3' end of the 20S pre-rRNA to assist Nob1 with D-site cleavage (**Fig 1.8**). The Pno1 binding site also prevents the premature binding of rpS26 (Heuer et al., 2017; Scaiola et al., 2018).

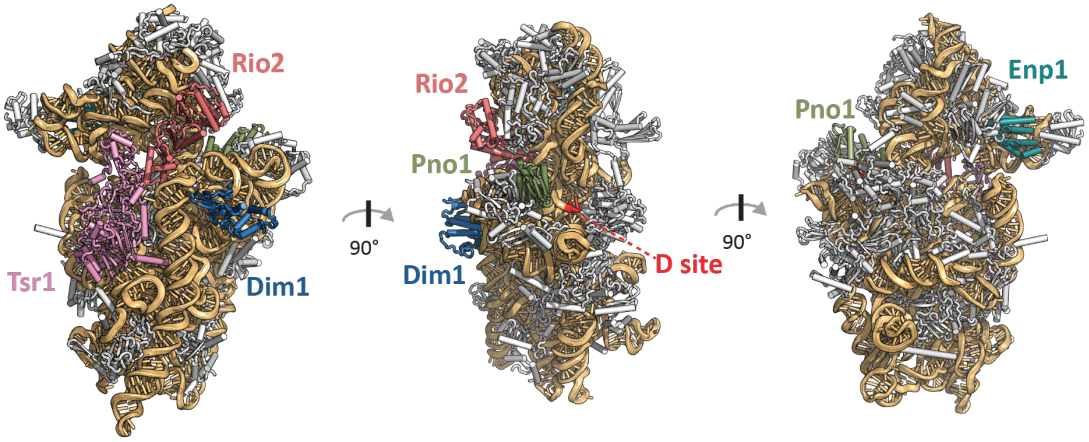

Figure 1.8 Cytoplasmic stage of assembly of the pre-small subunit. Cytoplasmic intermediate of the pre-40S (PDB 6RBD), with the 18S in orange and ribosomal proteins in gray. The D-site is located at the junction of the end of the mature 18S and ITS1. Two residues of ITS1 that are visualized are colored in red.

The final stages of small subunit assembly require "quality-control", where pre-40S test drive translation in order to finish maturation. Pre-40S associate with mature large subunits and form 80S-like complexes for this process. This requires binding of the GTPase Fun12 and the kinase Rio1 (Lebaron et al., 2012). Based on the pre-40S structures and mass spectrometry data from the Karbstein lab ((Strunk et al., 2012), Tsr1 and Rio2 are displaced from the pre-40S by Fun12 and Rio1 binding. The ATPase Fap7 interacts with the 80S complex to cause test-translocation and then promotes the rotated state of the ribosome. This conformation displaces Dim1 (Ghalei et al., 2017). Rio1 ATPase, in conjunction with Rli1 and Dom34, two proteins which cause dissociation of mature small and large subunits during translation, cause dissociation of the pre-40S from the mature 60S (Strunk et al., 2012). The final step of small subunit assembly is the cleavage at site D, and formation of the mature 18S rRNA. Pno1 is located near the D-site (Scaiola et al., 2018; Heuer et al., 2017), and either protects the cleavage site until this point, exiting the particle to allow Nob1 activity, or remains to help position Nob1 for nuclease activity. Although not visualized in pre-40S structures, Nob1 can bind to ITS1 (Lamanna & Karbstein, 2009), (Granneman et al., 2010), and likely leaves with the cleaved spacer, forming the mature 18S and completing small subunit assembly.

1.2.2 Large subunit assembly

The understanding of large subunit assembly has emerged in much the same way as small subunit assembly. Assembly factors associated with particular pre-60S rRNA intermediates were identified, and placing the time of action of these assembly factors was often facilitated by the greater number of distinct stages of pre-60S rRNA processing (**Fig 1.5**). At the start of this work, many cryo-EM structures of large subunit intermediates had greatly contributed to our understanding of LSU assembly from the late nucleolar stages to the very final steps of assembly in the cytoplasm. Our understanding of the very early stages of nucleolar assembly was limited by a lack of structural information. Our contribution to this gap in knowledge is the focus of Chapter 2, and the understanding of LSU assembly in the absence of these data is discussed below.

Large subunit assembly begins with transcription of the 25S region of the rDNA. There are several factors including Rrp5 and Has1 that are important for both large and small subunit assembly. Has1 is a DEAD-box helicase that has been implicated in the release of snoRNA from early SSU biogenesis, and in assembly of domain I of the 25S in early LSU assembly (Dembowski, et al., 2013; Emery et al., 2004). The C-terminal region of Rrp5 is visualized in the structures of the SSU processome, whereas biochemical data has identified the N-terminal regions of Rrp5 as important for cleavage at A3 and large subunit biogenesis (Lebaron et al., 2013; Venema & Tollervey, 1996; Hierlmeier et al., 2013) Depletion of Rrp5 prevents cotranscriptional processing of nascent rRNA and reduces pre-ribosomal particle compaction (Lebaron et al., 2013). Although these proteins offer intriguing opportunities for “cross-talk” between small and large subunits during the very beginning of the transcription of the LSU rRNA, mechanistic details of this level of regulation are currently unknown.

Although the understanding of the intricacies of the very beginning of large subunit assembly are still open questions, the factors that function in early pre-60S assembly have been identified. Work expressing fragments of the pre-60S rRNA containing ITS1, the 5.8S, ITS2, and portions of the 25S in yeast has helped identify how each domain of the 25S rRNA recruits assembly factors. Expression of constructs containing domain I recruits several assembly factors, as does expression up to domain II. These include factors implicated in both small and large subunit assembly like Rrp5 and the DEAD-box helicase Has1. These transcripts also recruited the “A factors”, the assembly factors needed for the processing of the 27SA into the 27SB rRNA (Woolford & Baserga, 2013). In contrast, constructs expressing truncations up to domain III, IV, and V recruit almost no new factors. The expression of domain VI, and a construct leading into the 3’ETS ending at site B0 once again recruit additional assembly factors, including some of the “B factors” which are assembly factors needed for cleavage at site C2 (**Fig 1.9**). At the start of this work, the roles of many of these early factors that are recruited during the very beginning of assembly were unclear. It was also of great interest to understand how domains III, IV, and V fold and assemble at the beginning of large subunit biogenesis as they do not recruit assembly factors when they are first transcribed (Chaker-Margot and Klinge, 2019). The lack of assembly factor binding by these domains is in contrast to small subunit assembly, where each subdomain of the 18S recruits many factors, and acts as an independent module until coalescing into the SSU processome after the 18S transcript is done being transcribed (Hunziker et al., 2019). The work presented in Chapter 2 characterizes the structure of early nucleolar pre-60S which begin to rationalize the pattern of assembly factor binding by the pre-

60S transcripts and contributes to the understanding of the earliest stages of LSU pre-rRNA binding.

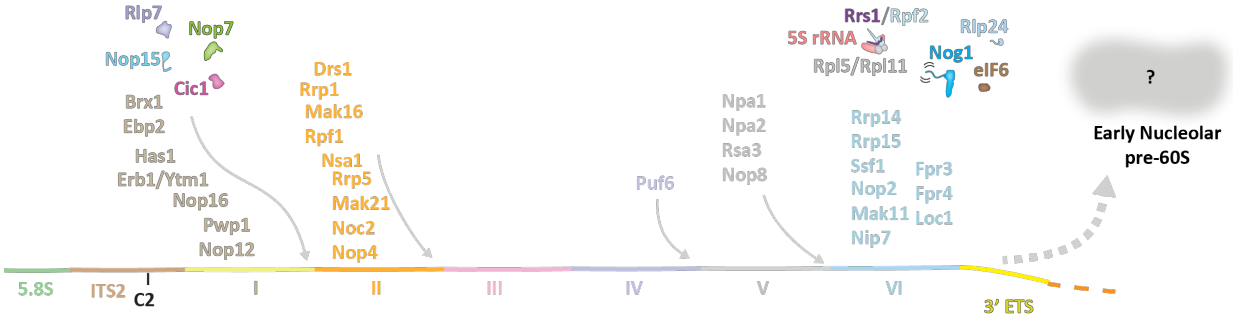

Figure 1.9 Recruitment of assembly factors at the beginning of large subunit assembly. Diagram of recruitment of large subunit assembly factors based on mass spectrometry studies expressing fragments of the pre-60S rRNA (Chaker-Margot & Klinge, 2019). Factors visualized in the late-nucleolar Nog2 particle (PDB 3JCT) are shown with their cartoon structures. Factors that have not been visualized/ had not been visualized at the start of this work are written above the subdomain of the rRNA that's transcription leads to their recruitment.

Structures of late nucleolar/ early nuclear pre-60S provided context for many of the A and B factors discussed above, and great insight into the pre-rRNA architecture and progression of assembly at this early stage (Wu et al., 2016). These assembly intermediates were isolated by affinity purification using the factor Nog2, an essential GTPase (Saveanu et al., 2001). Even at this early stage in assembly, a large majority of the 25S and 5.8S rRNAs are folded in a near mature conformation. The most notable exception is the remodeling of the central protuberance module, which contains the 5S rRNA and nearby sections of domain II and V on the subunit interface of the particle. Meanwhile, the nascent polypeptide exit tunnel and tRNA binding sites are chaperoned and blocked by assembly factors.

The 5S RNP (the 5S rRNA and ribosomal proteins L5 and L11), its chaperone factors Rrs1 and Rpf2, and helices H80 and H82-H88 of domain V are found rotated approximately 180 degrees from their mature location. The binding of the GTPase Nog2 stabilizes this flipped conformation, and also blocks the tRNA binding sites on the subunit interface of this particle. Nog1, another GTPase, has its N-terminal region located near the peptidyl transferase center, and disrupts base pairing in H89 of domain V. Nog1 continues around the circumference of the particle to the exit of the polypeptide tunnel, where its C-terminus inserts into the channel (**Fig 1.10**). Nog1 may protect this region from non-specific interaction, aid in tunnel assembly, and/or probe the completeness of tunnel assembly.

Another major feature of this particle is the intact ITS2 region, where the very beginning and end portions of the spacer are chaperoned by Cic1, Nop15, Rlp7, and Nop7, and Nop53 (Fig **1.10**).

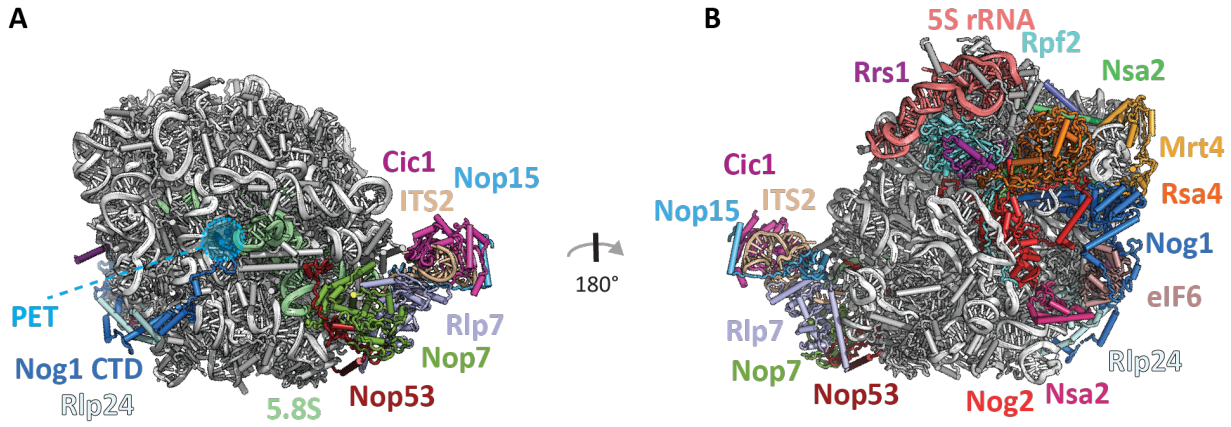

Figure 1.10 Architecture of the late nucleolar Nog2 particle. The Nog2 particle (PDB 3JCT) is presented with the pre-25S and ribosomal proteins in gray, and assembly factors, the 5.8S, and ITS2 in colors. **A**) The solvent exposed side of the Nog2 particle. The nascent Polypeptide Exit Tunnel (PET) is occupied by the Nog1 CTD. Arx1 is removed from this view, as it occludes the view of the PET. **B**) The subunit interface of the Nog2 particle. the 5S rRNA is rotated approximately 180 degrees from its mature conformation.

The cleavage of the ITS2 spacer at cite C2 must occur in the nucleolus, and is accomplished by the endonuclease Las1 working with kinase Grc3 (Castle et al., 2013; Pillon et al., 2017). This generates the 7S and the 25.5S rRNA intermediates (**Fig 1.5**). The 3' end of the 7S species is processed by the nuclear exosome, while the 5' end of the 25.5 is trimmed by the Rat1 and Rai1 nucleases (Allmang et al., 2000; Gasse, Flemming, & Hurt, 2015). It was hypothesized that some of the ITS2 associated assembly factors must leave for Las1 machinery and the nuclear exosome to access their substrates. The structural details of what conditions must occur in the pre-ribosome to allow Las1 recruitment and cleavage remain elusive, although biochemical understanding of Las1 and Grc3 function in vitro has been relatively better studied. Near-atomic structures of reconstituted nuclear exosome bound to pre-60S have been elucidated, and have contributed to our understanding of this stage of ITS2 processing. In this work from the Hurt and Conti labs, the authors reconstituted pre-60S particles purified using Nop53 as bait, and combined it with catalytically inactive nuclear exosome complex (Schuller et al., 2018). Overall, the composition of the particles was similar to the Nog2 particles previously described, the ITS2 region where the exosome binds being the exception. As hypothesized, all of the ITS2 factors have been either removed or disordered except for Nop7. Interestingly, Nop53, which was used as bait to purify the pre-60S and is known to recruit Mtr4 helicase via its Arch Interacting Motif (Thoms et al., 2015), is not visualized. Still, Mtr4 helicase is the major point of contact between the pre-60S and the exosome complex. It contacts residues in domain I and domain V of the 25S. The only clear non-Mtr4 mediated contact between the exosome and the pre-60S is between the last remaining ITS2 factor Nop7 and the exosome factor Rrp47.

Another critical step of assembly in the nucleoplasm is the rotation of the 5S into its mature position. This requires a series of enzymatic steps and rearrangements within the pre-LSU. The binding of the assembly factors Sda1 partially overlaps with the Rpf2, and therefore

may trigger release of Rpf2/Rrs1, allowing for partial rotation of the 5S (Wu et al., 2016). Rotation is completed and stabilized by binding of Rix1 and Mdn1. Mdn1 is a AAA ATPase, and its activity leads to GTP hydrolysis by Nog2, which triggers the release of Nog2 and all nearby assembly factors. The pre-60S must now become competent for export into the cytoplasm. A key assembly factor and export factor, Nmd3, can bind when Nog2 has exited the particle. Nmd3 binds on the subunit interface, directly contacting several of the large subunit active sites like the still immature peptidyl transferase center. Arx1 is another export factor that binds near the polypeptide exit tunnel and first associates with the particle late in the nucleolus, where it likely can only bind if proper incorporation of the ribosomal proteins that make up its binding surface have occurred (Bradatsch et al., 2012). The last export factors, Mex67 and Mtr2, can bind once Yvh1 phosphatase activity triggers release of Mtr4 from near the P0 stalk (Lo et al., 2009; Sarkar et al., 2016). The pre-60S can now transit through the nucleopore to the cytoplasm.

In the cytoplasm, the final ribosomal proteins are incorporated into the pre-60S, and the 60S active centers undergo their last maturation steps. First, the AAA-ATPase Drg1 is recruited to the LSU by Rlp24. Drg1 ATPase activity catalyzes the replacement of Rlp24 by its homolog, the ribosomal protein L24, and also causes the release of Nog1 and several other assembly factors (Kappel et al., 2012; Lo et al., 2010; Pertschy et al., 2007). Meanwhile, Rei1 has associated with the particle, inserting into the polypeptide exit tunnel that was vacated by Nog1 (Ma et al., 2017; Kargas et al., 2019). Rei1 also interacts with Arx1, and they both are removed from the pre-60S by the ATPase Ssa1 and its co-chaperone Jjj1 (Hung & Johnson, 2006; Demoinet et al., 2007; Meyer, Hoover, & Craig, 2010; Meyer et al., 2007; Lo et al., 2010). Upon Rei1 exit, the polypeptide exit tunnel is then occupied by Reh1. Recruitment and association of the ribosomal protein L16 shifts Nmd3 binding, and Lsg1 and Nmd3 leave the pre-60S with a mature peptidyl transferase center (Kargas et al., 2019). It is still unclear how Lsg1 GTPase activity plays a role in this dissociation, or what triggers Reh1 to exit the pre-60S. Finally, eIF6, the assembly factor that joins the pre-60S in the nucleolus and prevents association with the small subunit, is removed by Efl1 GTPase and Sdo1 (Weis et al., 2015). The binding of Sdo1 is incompatible with Nmd3 and Lsg1 binding, so the ability of these factors to bind the pre-60S may serve as the final checkpoint for LSU biogenesis (Kargas et al., 2019). These factors remove eIF6, and complete the process of large subunit assembly.

1.2.3 Regulation of ribosome assembly

Rapidly growing yeast cells produce approximately 2000 ribosomes per minute (Warner, 1999). High levels of this resource intensive process are therefore highly dependent on nutrient availability. The most major component of this regulation is the Target of Rapamycin (TOR) kinase. TOR activity coordinates cell growth under high nutrient availability and favorable environmental conditions (Reviewed by Rohde et al., 2001 and Loewith & Hall, 2011). The activity of all three RNA polymerases can be affected by nutrient availability via TOR signaling. Rapamycin treatment or low nutrient availability can induce the degradation of Rrn3, a RNA polymerase I transcription factor. In the absence of Rrn3, RNA PolI forms inactive homodimers, which are stored in the cell until favorable nutrient conditions reoccur (Torreira et al., 2017). PolI activity may also be regulated at the elongation stage in a TOR signaling and amino acid limitation linked manner, via regulation of the Paf1C transcription elongation factor (Zhang et

al., 2010). RNA PolIII activity is repressed by Maf1, which is a downstream target of TOR, so nutrient availability also effects the production of the 5S rRNA (Upadhya, Lee, & Willis, 2002). TOR signaling can also regulate ribosome biogenesis by controlling ribosomal protein levels. Proper processing of rRNAs is dependent on ribosomal proteins, and TOR signaling is required for the expression of ribosomal proteins, as treatment with rapamycin decreases r-protein levels to a greater extent than overall protein levels (Reiter et al., 2011; Powers & Walter, 1999).

There is also evidence of ribosome assembly factors playing a role in the regulation of PolI activity and ribosomal protein gene expression. Control of ribosome assembly must be coordinated with the cell cycle and replication and new evidence implicates the SSU assembly factor Rio1 kinase in this process, where Rio1 downregulates PolI activity during both S phase and Anaphase (Iacovella et al., 2015). This offers intriguing evidence for cross-talk between assembly and PolI regulation. Another small subunit assembly factor, Utp22, is has been implicated in regulation of ribosome biogenesis. Ifh1 is a transcription factor which increases expression of ribosomal protein genes. Utp22 can remove Ifh1 from the genomic DNA under growth inhibiting conditions, thereby stopping ribosomal protein gene expression. Interestingly, this may be a TOR-independent regulation mechanism. Further, RNA PolI activity stops Utp22 from removing Ifh1 from ribosomal protein genes, therefore tuning the production of ribosomal proteins with that of ribosome biogenesis (Albert et al., 2016).

1.3 RNA Helicases are essential for ribosome biogenesis

As discussed in the previous sections, a portion of the assembly factors necessary for ribosome biogenesis are RNA helicases. The precise function of many of these assembly factors remains elusive, and an understanding of these functions is necessary for a complete understanding of the ribosome assembly process. The general biology of DEAD- and DEAH-box RNA helicases is introduced below, followed by a specific discussion of helicases involved in ribosome assembly, with a focus on the DEAH-box helicase Dhr1.

1.3.1 DEAD-box and DEAH-box RNA Helicases

RNA and DNA helicases are categorized into superfamilies. The original classification into three SFs was done by Gorbalenya and Koonin and based on the primary sequence of putative helicases (Gorbalenya & Koonin, 1993). The classification was expanded into its current form by Singleton, Dillingham, and Wigley and now sorts the DNA and RNA helicases and translocases into six superfamilies (SF1-SF6) (Singleton, Dillingham, & Wigley, 2007). All these proteins contain tandem RecA-like folds that exist either in the same polypeptide chain or between subunits of a larger assembly. These proteins convert chemical energy to mechanical energy via NTP binding and hydrolysis that is coupled to protein conformational change. The largest two superfamilies, SF1 and SF2, contain proteins where the two RecA domains are in a single polypeptide chain. The characterization of the subfamilies within SF1 and SF2 has been further refined by Fairman-Williams, Guenther, and Jankowsky in 2010 (Fairman-Williams, Guenther, & Jankowsky, 2010).

Most RNA helicases are categorized into SF2, and are further subdivided into subfamilies. For this work, the two most important SF2 subfamilies of helicases are the DEAD-box and DEAH-box proteins (Fairman-Williams, Guenther, & Jankowsky, 2010). They are named

for the Aspartate-Glutamate-X-Histidine (DEAH) or Aspartate-Glutamate-Alanine-Aspartate (DEAD) conserved motifs. These proteins contain the two Rec-A domains arranged in tandem, and these RecA domains contain several well conserved motifs that are important for function (**Fig 1.11**). The functional sites for NTP binding and hydrolysis are well-conserved within each subfamily. Binding sites for the substrate nucleic-acid backbone are also well conserved, but less conserved than the NTP binding sites (Fairman-Williams et al., 2010). Biochemical and structural studies have revealed that additional nucleic acid binding can occur at variable regions of the helicases, which adds to the functional diversity of these proteins (Sloan & Bohnsack, 2018). Several members of these helicase families have been well studied, and have therefore provided a framework for how each subfamily works on its RNA substrates. Each group will be discussed in more detail below.

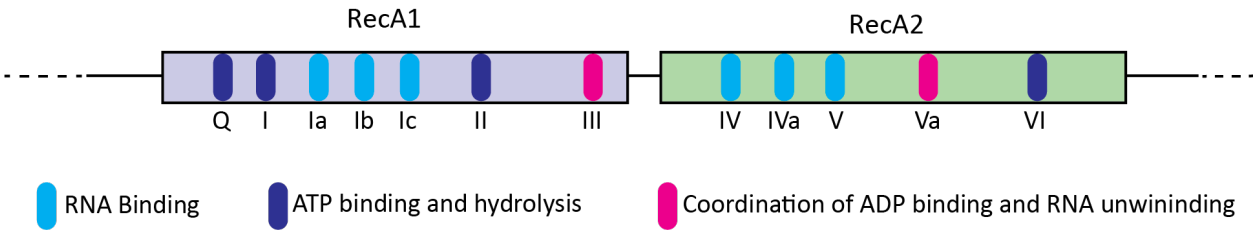

Figure 1.11 Motifs of the SF2 family of helicases. The key conserved motifs of SF2 family of helicases and their relative locations within the RecA1 and RecA2 domains.

DEAD-boxes

The DEAD-boxes are the largest member of the SF2 family. The DEAD-box helicase core contains only the two tandem RecA domains linked by a short, flexible linker (Fairman-Williams et al., 2010). DEAD-boxes also can contain N- and/or C-terminal extensions with various biological roles that will be elaborated on below (**Fig 1.12A**).

The two RecA domains of the DEAD-box core must bind and hydrolyze ATP and bind RNA substrate. Motifs necessary for binding nucleotide line the binding surface of each RecA and the closure of the RecA domains creates a functional ATPase site (Theissen et al., 2008). RNA binding occurs on both domains as well, but on another, solvent exposed surface (Andersen et al., 2006; Bono et al., 2006; Collins et al., 2009; Sengoku et al., 2006). Studies on a diverse set of DEAD-boxes have revealed that the RecA1 domain has higher affinity for nucleotide than the RecA2. But, there is no consensus on which RecA primarily binds substrate RNA. Additionally, some DEAD-boxes cannot bind RNA in the absence of NTP binding, while others can (Samatanga & Klostermeier, 2014; Lorsch & Herschlag, 1998; Dreyfus, & Linder, 1999).

Given the biochemistry and structural data available, the general mechanism of DEAD-boxes is described as RNA “clamping” (**Fig 1.12B**). DEAD-boxes bind onto short, exposed RNA duplexes and unwind these features by disrupting the secondary structure, not by processive unwinding activity. The enzymes bind onto their substrate RNA and nucleotide, and closure of the core creates a functional ATPase site. This core closure distorts the substrate RNA structure and one RNA strand to stay tightly held to the enzyme, while the other strand no longer base

pairs and is released from the helicase. Opening of the core and the release of ADP, inorganic phosphate, and the ssRNA allows the catalytic cycle to begin again (Andersen et al., 2006; Bono et al., 2006; Collins et al., 2009; Del Campo & Lambowitz, 2009; Moeller, Basquin, & Conti, 2009; Sengoku et al., 2006).

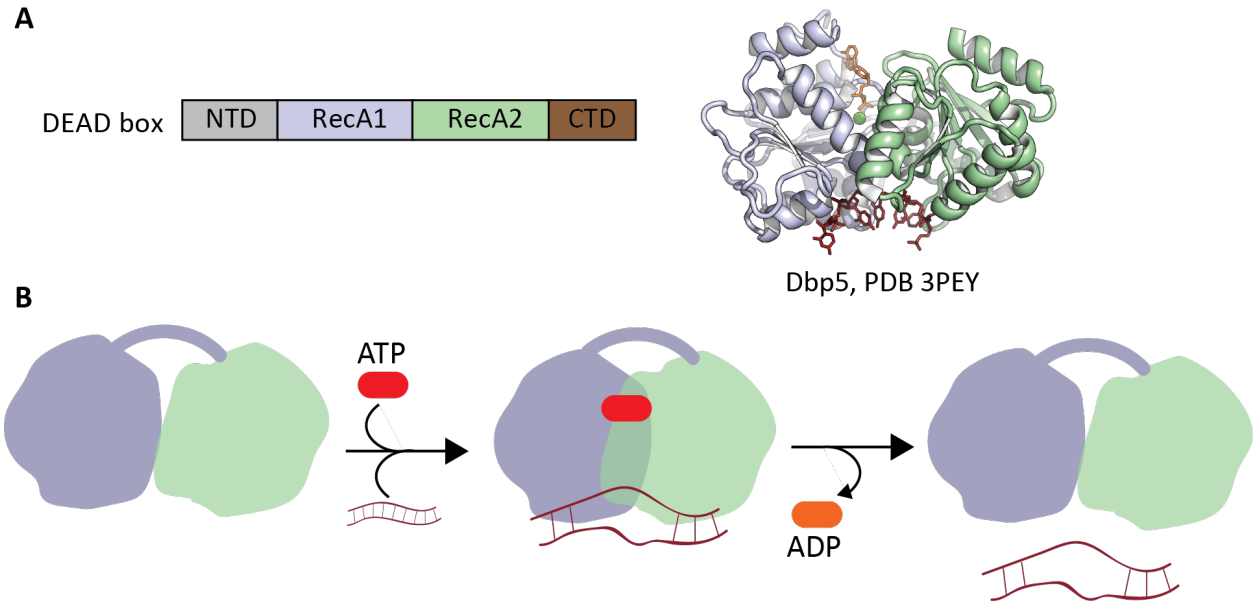

Figure 1.12 Overview of DEAD-box helicases. A) Domain architecture of a DEAD-box helicase. NTD and CTDs are variables between helicases. An example of a DEAD-box helicase, Dbp5, bound to single stranded RNA and ADP BeF_3. **B**) A simplified schematic of the DEAD-box catalytic cycle, where the helicase core undergoes conformation change after dsRNA and ATP binding which disrupts dsRNA basepairing. ATP hydrolysis releases ADP and the unwound RNA substrate.

In addition to the helicase core, DEAD-box proteins can contain N- and C-terminal extensions that can impact function and interaction with binding partner proteins. Some well-studied examples will be elaborated below.

Mss116 is a DEAD-box required for the splicing of mitochondrial group I and group II introns (Huang et al., 2005). Mss116 and its homologs contain a C-terminal extension that can create additional kinking in the retained strand of the substrate RNA, which increases unwinding efficiency (Del Campo & Lambowitz, 2009). The human DEAD-box protein DDX19 is essential for mRNA nuclear export, and contains an N-terminal extension that is auto-inhibitory. This N-terminal extension inserts a helix into the ATP binding site when the enzyme is bound to ADP, preventing closure of the core, and therefore preventing catalysis (Collins et al., 2009).

Due to the ability of DEAD-boxes to “clamp” onto dsRNA substrates before ssRNA release, it has been hypothesized that DEAD-boxes can work as RNA clamps and as RNA-protein assembly platforms. In these cases, a DEAD-box will be kept in the RNA-bound state by its

binding partner proteins. This has been observed for the DEAD-box eIF4A-III. This helicase forms the core of the exon-junction complex by remaining bound to the nascent mRNA after splicing (Tange, Nott, & Moore, 2004). The protein complex MAGOH-Y14 binds to eIF4A-III and stabilizes its ADP-Pi bound state, preventing the release of RNA substrate (Ballut et al., 2005; Nielsen et al., 2009). This allows the exon junction complex to remain tethered to the mRNA after splicing and to travel as a complex into the cytoplasm, until it is removed by the ribosome during the first round of translation (Tange et al., 2004). Additionally, the EJC complex is an example of a protein co-factor affecting RNA substrate affinity. Early studies found that EJC component MLN51 increases the affinity of eIF4A-III for RNA (Ballut et al., 2005). Crystal structures of reconstituted EJC revealed MLN51 contacts both the RecA1 and RecA2 domains of eIFA-III and interacts with the ssRNA bases (Bono et al., 2006; Andersen et al., 2006).

DEAH-boxes

In addition to the tandem RecA domains requisite to be part of Superfamily 2, DEAH-box proteins also contain a degenerate Winged-Helix domain, an OB fold, and a Ratchet-like domain C-terminal to the RecA2 domain. These five domains define the DEAH helicase core (**Fig 1.13A**). DEAH-boxes, like DEAD-boxes, also often contain N- and/or C-terminal extensions on the helicase core. The mechanism of DEAH box function is currently less well explored than that of DEAD-boxes, but it is generally agreed upon that DEAH-boxes are processive helicases that bind 3’ single stranded overhangs of RNA substrates.

Available structures of DEAH boxes have provided an understanding of the overall structure and function of these helicases and how they contrast with the DEAD-box family. Collectively, the structures reveal that NTP binding occurs between RecA domains, using the same conserved sites as the DEAD-boxes. In structures lacking nucleotide, the RecA domains are in an “open” conformation. Nucleotide binding causes the RecA domains to close and form a functional ATPase site, while the overall core remains open for substrate RNA binding. Substrate RNA is contacted by the RecA domains, the OB fold, and the Ratchet-like domains, and mostly occurs through non-specific binding to the phosphate backbone. With nucleotide and RNA substrate bound, the OB-fold, Ratchet-like, and Winged-Helix domains rotate closer to the RecA domains and enclose the RNA substrate (reviewed in Gilman, Tijerina, & Russell, 2017). Further, RNA bound structures revealed two motifs called the “Hook-turn” and “Hook-loop” within the RecA1 and RecA2 domains that contact the ssRNA. When the RecA2 domain shifts open after NTP hydrolysis, movement of these motifs allows for an additional nucleotide at the 5’ end of the substrate RNA to be accommodated into the RNA binding channel. This allows the DEAH-boxes to translocate along their substrates (reviewed in K. E. Bohnsack et al., 2021; **Fig 1.12B**).

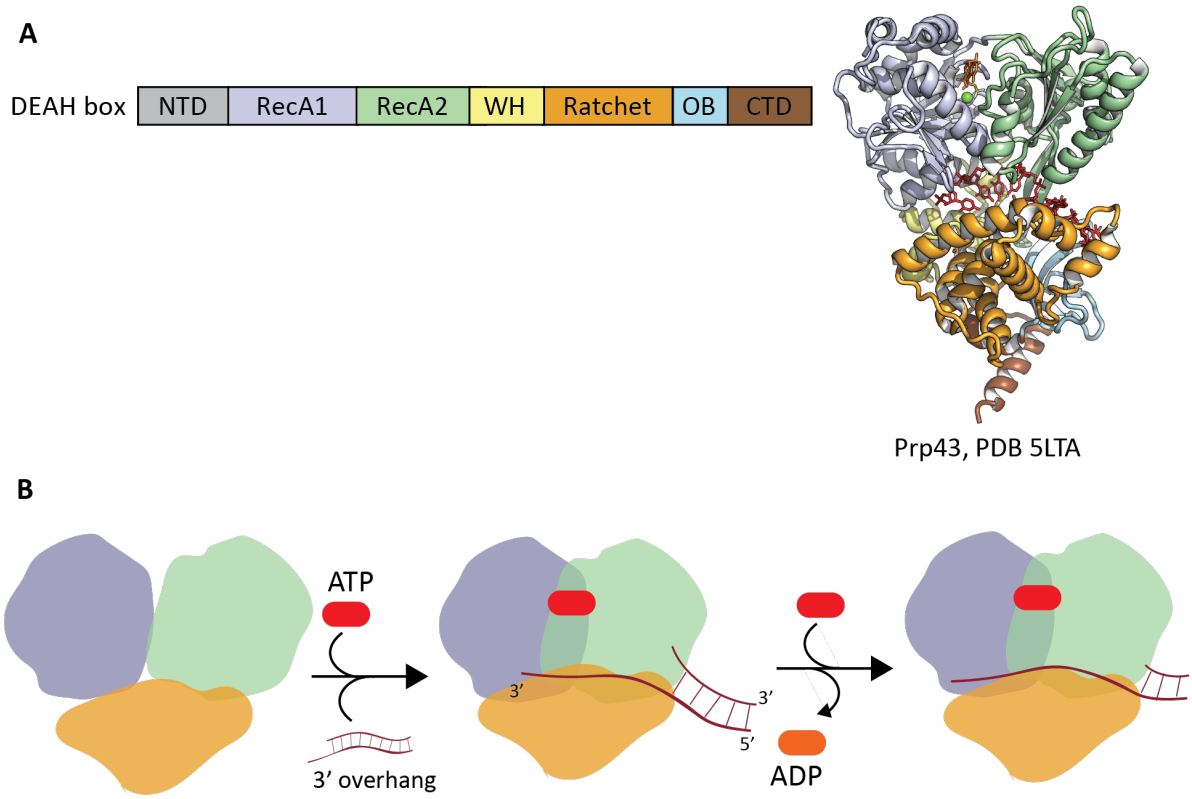

Figure 1.13 Overview of DEAH-box helicases. **A**) Domain architecture of a DEAH-box helicase. NTD and CTDs are variables between helicases. An example of a DEAH-box helicase, Prp43, bound to single stranded RNA and ADP-BeF_3. **B**) A simplified schematic of the DEAH-box catalytic cycle, where the helicase core engages with a 3' single stranded overhang of the RNA substrate. Binding of ATP and RNA forces the substrate through the RNA substrate channel as the helicase core compacts. Release of nucleotide allows the core to become more open, and accommodate an additional base at the 5' of the substrate RNA. Another cycle of ATP binding and hydrolysis closes the core and pushes another base of RNA past the RecA1 domain, which allows the helicase to translocate along the RNA and disrupt basepairing in the double stranded region of the substrate.

One of the most well studied of DEAH-box helicases is Prp43. Prp43 is required for the disassembly of the intron-lariat spliceosome during the final stage of splicing (Arenas & Abelson, 1997; Fourmann et al., 2016). Prp43 has also been implicated for roles in ribosome biogenesis and apoptosis (M. T. Bohnsack et al., 2009; Lebaron et al., 2005). Structural studies of Prp43 have greatly contributed to our general understanding of DEAH-box structure. Co-crystal structures of Prp43 with ATP analogs, ADP, and/or RNA have revealed some of the movement of the helicase core that must occur throughout substrate unwinding (Tauchert et al., 2017; Walbott et al., 2010). Overall, the RecA domains relative to the C-terminal module (Ratchet-like, OB fold, and Winged-helix) are most open when bound to ATP alone, become more compact when bound to ATP and RNA, and then the most compact when only bound to ADP (**Fig 1.14**). The most open structures are interpreted as ATP-bound and primed for substrate binding. Once RNA substrate binds, the overall structure compacts to allow for unwinding, as described above (Tauchert et al., 2017).

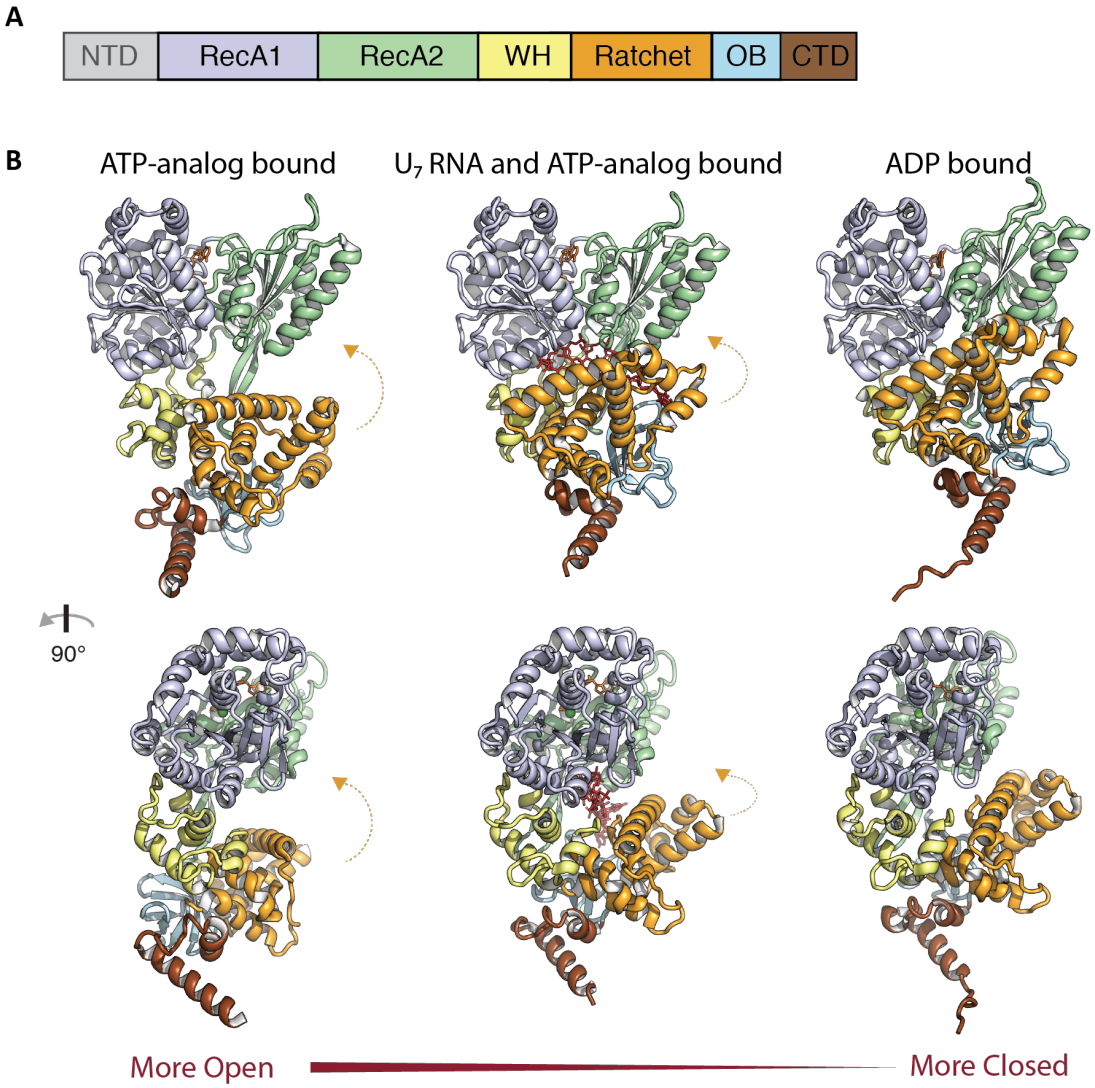

Figure 1.14 Overview of conformational changes within the Prp43 helicase core caused by nucleotide and RNA binding. A) Diagram of DEAH-box helicase domains. B) Comparison of various Prp43 crystal structures. The ATP-analog bound structure (PDB 5LTK) has the most open core, RNA and ATP-analog bound structure (PDB 5LTA) is in an intermediate state, and ADP bound Prp43 (PDB 5DOU) has the most compact core.

There is also data on how Prp43 is activated and regulated by a family of binding proteins called "G-patch" proteins, which contain a highly-conserved G-rich sequence. Bioinformatics and biochemical studies have identified several G-patch proteins and their targets (K. E. Bohnsack et al., 2021). Thus far, all G-patches identified in yeast activate Prp43 except for one: Spp2. Spp2 activates another DEAH-box involved in spliceosome assembly, Prp2 (Silverman et al., 2004; Warkocki et al., 2015). The co-crystal structure of *C. thermophilum* Prp2 and Spp2 reveals that co-activator binding causes a slight rotation of the Prp22 ratchet domain

closer to the RecA domains (Studer et al., 2020). But, recent cryo-EM structures of *S. cerevisiae* Spp2 bound Prp2 reveal no overall changes in Prp2 helicase conformation (Bai et al., 2021). The exact mechanism of how Spp2 effects Prp2 activity remains elusive. More structural studies involving substrate RNA and different DEAH-boxes and their G-patches will contribute to a better understanding of this activation mechanism and an overall understanding of DEAH-box function.

DEAH-boxes are activated by cofactors besides G-patch proteins, but the mechanistic details of these activations are not well understood (reviewed in Sloan & Bohnsack, 2018). Dhr1, a helicase involved in ribosomal small subunit biogenesis, is both recruited to its substrate and activated by the protein Utp14, which does not contain any G-patch motif (Zhu et al., 2016). In the next section, an overview of the RNA helicases important for ribosome assembly will be provided, with a focus on the understanding of Dhr1 function before the start of this work.

1.3.2 **RNA Helicases involved in eukaryotic ribosome biogenesis**

As discussed in Chapter 1.2, ribosome biogenesis is a complex process that necessitates the coordinated rearrangement of the rRNA, and timely recruitment and removal of ITS, ETS, and snoRNA elements. These steps require the action of RNA helicases, summarized in Table 1. The exact RNA targets of many of these helicases remains unclear, and only one of these, Mtr4, has been structurally characterized in the context of its target at the start of this work (Schuller et al., 2018). The helicases Mtr4, Dbp6, and Dhr1 are of the greatest interest to this work. Mtr4 and Dbp6 are discussed briefly below, while Dhr1 is introduced in greater depth in section 1.3.3. The contributions of this work towards the understanding of Dhr1 function can be found in Chapter 3.

Table 1.1 List of RNA helicases involved in *S. cerevisiae* ribosome biogenesis. Contains the names of helicases implicated in ribosome biogenesis in the yeast *S. cerevisiae* and literature sources where the proven or purported function is described. The more extensively characterized helicases that have been discussed in detail in other locations in this text are also specified in the "source" column.

Yeast Protein	SSU or LSU biogenesis	Classification	Sources
Prp43	SSU, LSU	DEAH-box	Leeds, Small, Hiley, Hughes, & Staley, 2006; Combs, Nagel, Ares, & Stevens, 2006; M. T. Bohnsack et al., 2009; Pertschy et al., 2009
Dhr1	SSU	DEAH-box	See Chapter 1.3.3, Chapter 3
Dhr2	SSU	DEAH-box	Colley, Beggs, Tollervey, & Lafontaine, 2000
Dbp2	LSU	DEAD-box	Bond, Mangus, He, & Jacobson, 2001
Dbp3	LSU	DEAD-box	Weaver, Sun, & Chang, 1997
Dbp4	SSU	DEAD-box	Soltanieh, Lapensée, & Dragon, 2014; Kos & Tollervey, 2005
Dbp6	LSU	DEAD-box	Kressler, la Cruz, Rojo, & Linder, 1998; la Cruz, Kressler, Linder, Deloche, & Lacombe, 2004; see Chapter 4
Dbp7	LSU	DEAD-box	Daugeron & Linder, 1998
Dbp8	SSU	DEAD-box	Daugeron & Linder, 2001
Dbp9	LSU	DEAD-box	Daugeron, Kressler, & Linder, 2001
Dbp10	LSU	DEAD-box	Burger, Daugeron, & Linder, 2000
Drs1	LSU	DEAD-box	Ripmaster, Vaughn, & Woolford, 1992
Mak5	LSU	DEAD-box	Zagulski, Kressler, Bécam, Rytka, & Herbert, 2003; Brüning et al., 2018
Spb4	LSU	DEAD-box	la Cruz, Kressler, Rojo, Tollervey, & Linder, 1998; Brüning et al., 2018
Has1	SSU, LSU	DEAD-box	Emery et al., 2004; Dembowski et al., 2013; Brüning et al., 2018
Rok1	SSU	DEAD-box	Khoshnevis et al., 2016
Rrp3	SSU	DEAD-box	O'Day, Chavanikamannil, & Abelson, 1996
Fal1	SSU	DEAD-box	Kressler, la Cruz, Rojo, & Linder, 1997
Mtr4	LSU	Ski2	Allmang et al., 1999; Allmang et al., 2000; Du et al., 2020; Lau et al., 2021; Schuller et al., 2018

Mtr4 and the nuclear exosome

Mtr4 is the Ski2-like helicase component of the nuclear exosome. The Ski2 family of helicases is reviewed by Johnson and Jackson (Johnson & Jackson, 2013). The conserved helicase core of the Ski2 family contains a RecA1, RecA2, a Winged Helix, and a Ratchet domain with a Ski-2 family specific insertion within the Winged Helix domain called the Arch domain. The nuclear exosome degrades the 3' ends of various RNA species to maintain RNA quality control in the cell. Additionally, the action of the nuclear exosome associated with the Mtr4 helicase is required for the biogenesis of both the small and large subunits. In ribosome biogenesis, association of Mtr4 with the exosome may aid in both targeted recruitment of the exosome to pre-ribosomes and also aid in the unwinding of complex pre-rRNA structures to facilitate processing by the exosome. In LSU biogenesis after C2 cleavage the Mtr4-exosome degrades the 7S pre-rRNA to form the mature end of the 5.8S rRNA. First, Mtr4 helicase engages with the LSU and channels the ITS2 rRNA into the exosome core. Next, processive exonuclease Rrp44 shortens the 7S rRNA to the 5.8S rRNA with 30 additional nucleotides. Those final 30 nucleotides are degraded by the distributive exonuclease Rrp6 (Allmang et al., 1999; Briggs, Burkard, & Butler, 1998; Fromm et al., 2017). Recruitment of the exosome to the LSU is accomplished by Nop53, which contains an Arch Interacting Motif (AIM) that interacts with Mtr4 helicase. The nuclear exosome associated with the pre-60S has been visualized in a structure from the Conti and Hurt labs (Schuller et al., 2018). Here, the exosome is trapped on a nuclear pre-LSU that has undergone C2 cleavage. Although Nop53 was used as the bait to isolate the pre-60S, Nop53 density was not well ordered and not observed in the structure. Other areas of Mtr4 binding were visualized- Mtr4 contacts domain V of the pre-25S and also contacts the base of the premature L1 stalk. Therefore Mtr4 binding may sense the overall state of the pre-60S, and only be recruited to the exosome when both the ITS2 region and domain V are at the appropriate stage of assembly (Schuller et al., 2018).

The exact function of the exosome in small subunit assembly is less clear, despite recent structures of the exosome docked onto maturing SSU processomes (Du et al., 2020; Lau et al., 2021). Here, pre-40S purified from yeast in both pre-A1 and post-A1 cleavage states show that the exosome associates near Utp14, Utp6, and Utp18. Utp18 contains the AIM and like Nop53, the AIM region of Utp18 was not ordered and therefore not visualized in the structure. The exosome is positioned near the 3' end of the 5'ETS, and may contribute degradation of portions of the 5' ETS, but it is unclear exactly what portions are degraded by the exosome while it is docked on the pre-SSU particles (Du et al., 2020; Lau et al., 2021). This is discussed in the context of small subunit biogenesis in Chapter 1.2.

Dbp6 and the Urb subcomplex

Dbp6 is a member of the DEAD-box family of helicases and currently its role in ribosome biogenesis is unclear. Dbp6 was discovered as a genetic and physical interactor of other nucleolar assembly factors that were essential for large subunit assembly and associated with the earliest large subunit pre-rRNA species, the 27SA (Kressler et al., 1998 ; Rosado et al., 2004; Dez et al., 2004; Rosado et al., 2007). Key work identified that Dbp6 interacts stably with the proteins Nop8, Rsa3, Urb1, and Urb2, even in the absence of RNA (Rosado et al., 2007). We refer to this complex of proteins as the "Urb Subcomplex". Although all proteins in this complex except Rsa3 have been identified as essential, the exact role of these factors besides

importance to processing of the 27S remains unclear. Preliminary study on the Urb subcomplex and Urb subcomplex containing Pre-60S (Urb particle) are discussed in Chapters 4.

1.3.3 Dhr1 is essential for small subunit biogenesis.

The early stages of small subunit biogenesis are discussed in Chapter 1.2. Early studies of the U3 snoRNA revealed that it is an essential component of the small subunit processome, and that its removal is necessary for small subunit biogenesis to progress into the nuclear stages. In the small subunit processome, the rRNA domains of the 18S are splayed apart from one another while the central pseudoknot is prevented from forming, in part due to base-pairing with the U3 snoRNA (**Fig 1.7**, for an overall discussion of small subunit biogenesis, see Chapter 1.2). Key features of the mature small subunit are the compact nature of its rRNA domains and the central pseudoknot. So, in order for small subunit biogenesis to progress past the formation of the small subunit processome, the U3 snoRNA must be removed. Dhr1 is the helicase responsible for removal of the U3 snoRNA and is also one of the most extensively studied helicases required for ribosome biogenesis. It was discovered by Alan Colley and colleagues as an essential nucleolar protein needed for proper cleavage at A1 and A2 sites on the pre-rRNA that also co-precipitated with the U3 snoRNA (Colley et al., 2000). Dhr1 had a putative helicase fold, and a collaborative work from the Tollervey, Correll, and Johnson labs confirmed Dhr1s in vitro RNA unwinding activity (Sardana et al., 2015). Using an ATP hydrolysis deficient mutant of Dhr1, they observed pre-ribosomes where A2 cleavage did not occur, a lack of r-proteins binding near the central pseudoknot, and the persistence of the U3 snoRNA. These observations were rationalized as an effect of a lack of U3 snoRNA removal caused by the inactive Dhr1 helicase. Additionally, protein-RNA crosslinking (Crosslinking and Analysis of cDNA, CRAC) revealed crosslinks between Dhr1 and the U3 snoRNA, confirming a physical interaction between Dhr1 and U3 snoRNA (Sardana et al., 2015).

As the potential role of Dhr1 in ribosome biogenesis was becoming more clear, further work was identifying the protein interaction network of Dhr1. Genetic and biochemical work from the Johnson lab explored the interactors of Bud23, a methyltransferase responsible for the methylation of m7G1575. Although non-essential, deletion of Bud23 creates a severe growth defect in yeast and leads to a reduction in 40S levels (White et al., 2008). Sardana et al. began identifying the genetic interactors of Bud23, implicating Bud23 in the early stages of small subunit biogenesis. Several Dhr1 mutants were identified as suppressors of the ΔBud23 phenotype. Yeast two-hybrid assays implicated the first 467 residues of Dhr1 as essential for interaction with Bud23. Exactly how Dhr1 and Bud23 effect each other's function remained unclear. Another genetic interactor of Bud23 identified was Utp14 (Sardana, White, & Johnson, 2013). Utp14 was originally identified as a component of the SSU processome and at the time its exact function was unknown (Dragon et al., 2002). Further study found that Utp14 interacts with Dhr1 by yeast two hybrid analysis (Zhu et al., 2016).

The structure of the SSU processome also revealed Utp14 to be a key structural factor, which weaves through the particle binding both protein and RNA components. Protein-protein crosslinking also confirmed contacts between Utp14 and Dhr1 and that Dhr1 was present in the SSU processome, though not visualized in the EM density. The exact trigger for Dhr1 activity is not known, and at the start of this work it remained unclear exactly where Dhr1 docks on to the U3 snoRNA to begin translocation in the 3' to 5' direction. It is likely that some rearrangements

in the SSU processome structure must occur before Dhr1 can access its RNA substrate and begin its activity. Structural snapshots of this stage of SSU assembly were very recently solved, and they are discussed in the context of the data produced in this work in Chapter 3.1.4.

Dhr1 has been most extensively studied in yeast, but some foundational work has been performed on the human homolog, DHX37 (Choudhury et al., 2019). It is largely in agreement with the data from yeast, except that the N-terminal domain interaction with Bud23 may not occur as the segments of Dhr1 necessary for this interaction are not conserved in human DHX37. But, the DHX37 CTD is necessary for interaction with human Utp14, in agreement with yeast studies. Additional biochemistry found that the activation of DHX37 is also in agreement with some yeast studies where DHX37's RNA dependent ATPase activity was increased by Utp14.

Although Dhr1 was not visualized in the context of the SSU processome, it has been structurally characterized in isolation by the Graille lab and Jinek lab (Boneberg et al., 2019; Roychowdhury et al., 2019). The structure of *S. cerevisiae* Dhr1 revealed the overall structure of the core and the C-terminal domain in the absence of nucleotide. Here, the helicase core was in an open conformation relative to RNA bound structures of DEAH-boxes (**Fig 1.15**). Additionally, in vivo studies found that the CTD of Dhr1 is essential for cell growth. In ATPase assays, though, constructs of Dhr1 lacking the CTD had similar RNA stimulated ATPase activities compared to full length Dhr1. Deletion of the CTD impaired Utp14 binding in in vitro pulldown assays. Boneberg et al. studied the murine homolog of Dhr1, DHX37. They crystallized the helicase core and CTD of DHX37 in the presence of a polyuridine RNA. This RNA bound structure of DHX37, like the RNA bound structure of Prp43, has the helicase core in a closed conformation, grasping the RNA strand in a sequence non-specific manner (**Fig 1.15**). The RecA domains are splayed apart from each other, relative to the Prp43-RNA structure, but this appears to be a crystal packing artefact. The authors also biochemically characterized DHX37 and murine Utp14. They found that Utp14 stimulates DHX37 RNA-dependent ATPase activity, increases DHX37 affinity for RNA, and further increases DHX37 affinity for RNA in the presence of ADP or AMPPNP. Additionally, a more minimal fragment of Utp14 (residues 555-619) responsible for the activation of DHX37 ATPase activity was identified. The role of the DHX37 CTD was also explored. They confirmed that the CTD of DHX37 is necessary, but not sufficient for stable interaction with Utp14 in pull down assays, and for the stimulation of DHX37 RNA-depending ATPase activity. Like Roychowdhury et al.'s work on *S. cerevisiae* Dhr1, the RNA-dependent ATPase activity was similar between DHX37 constructs with and without the CTD.

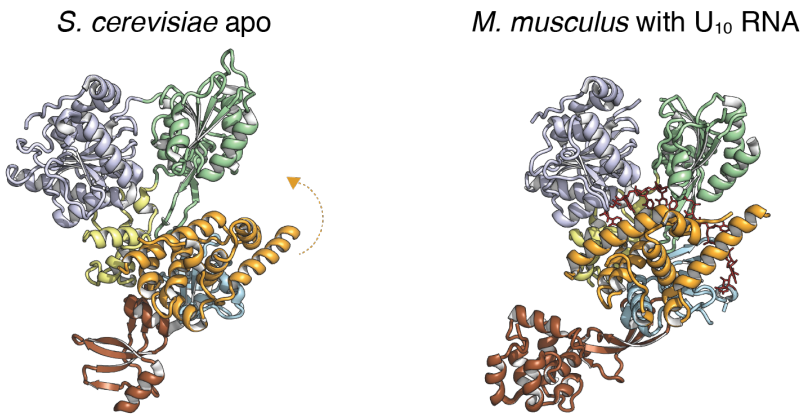

Figure 1.15 Two distinct conformations of the Dhr1 helicase core observed in crystal structures. The *S. cerevisiae* apo structure (PDB 6H57) is in a more open conformation than the *M. musculus* homolog of Dhr1 co-crystallized with single stranded RNA (PDB 6O16).

Despite the wealth of information on Dhr1 and Utp14 both structurally and biochemically, the exact mechanism of how Utp14 stimulates Dhr1 activity is still unclear. The role of the Dhr1 CTD in helicase activity or in the interaction with Utp14 has also not been fully elucidated. This data is necessary to understand how SSU biogenesis continues in the early stages. It will also contribute to the general understanding of how DEAH box helicases are stimulated by their co-activators, which is currently lacking. The interaction between Dhr1 and Utp14 will be further studied in this work in Chapter 3.

Chapter 2:
Structural characterization of the nucleolar pre-60S

At the start of this work, our understanding of the assembly of the large ribosomal subunit (60S) was greatly improved by cryo-EM snapshots of pre-60S particles from the nucleus and cytoplasm (Chapter 1.2.2). Due to a lack of structural information on early nucleolar precursors, there existed a large gap in our understanding of the very beginning of LSU assembly, pre-rRNA folding, and the functional roles of the nucleolar-specific assembly factors. Our goal was to contribute to the understanding of nucleolar large subunit assembly by elucidating the cryo-EM structure of a 27SB pre-rRNA containing pre-60S.

This work was pioneered by Sebastian Klinge and Zahra Sanghai. Sebastian began the search for the ideal protein bait to isolate nucleolar pre-60S. Zahra continued this work, cloning doubly tagged yeast strains and optimizing the purification and cryo-EM grid preparation of the nucleolar pre-60S. Protein-protein cross-linking and mass spectrometry was done in collaboration with Brian T. Chait's lab at Rockefeller. I purified and prepared cross-linked sample which I then provided to Kelly R. Molloy and Junjie Wang of the Chait lab for analysis. Zahra and I collected several cryo-EM datasets of the pre-60S. Zahra, Sebastian, and I worked together to process the EM datasets and build the pre-60S structure. The entire lab greatly aided Zahra and I when swift preparation of the manuscript became necessary in the winter of 2017- Jonas Barandun, Mirjam Hunziker, and Malik Chaker-Margot helped finish the building that needed to be done, helped prepare figures, and correct the manuscript.

2.1 Purification and Composition of nucleolar pre-60S

To enrich for 27SB containing pre-60S, purification of these particles was optimized under nutrient deprivation conditions- yeast cells were grown to high optical density in minimal media with galactose instead of glucose as a nutrient source. This approach was previously used to successfully accumulate the small subunit processome, a 23S rRNA containing species, that was shown to accumulate as cells switch from exponential growth to the stationary phase (Talkish et al., 2016). The optimal pair of assembly factors for purification of the accumulated pre-60S were Nsa1 (tagged with GFP) and Nop2 (tagged with 5x beta-catenin peptide) (**Fig 2.1A**). These proteins had previously been characterized as nucleolar and 27SB associated proteins (Harnpicharnchai et al., 2001).

Mass spectrometry analysis of the purified pre-60S identified several nucleolar specific factors and other factors associated with the 27SB rRNA (**Fig 2.1B**). Northern blotting was used to confirm that these were 27SB containing particles (**Fig 2.1C-E**). Northern blotting also revealed the presence of the 5S at this stage of assembly, which was in agreement with the presence of the 5S chaperoning assembly factors Rpf2 and Rrs1 in our mass spectrometry data (**Fig 2.1E**). The interactions of the proteins within the purified particles was assessed by chemical cross-linking of the sample followed by mass spectrometry analysis.

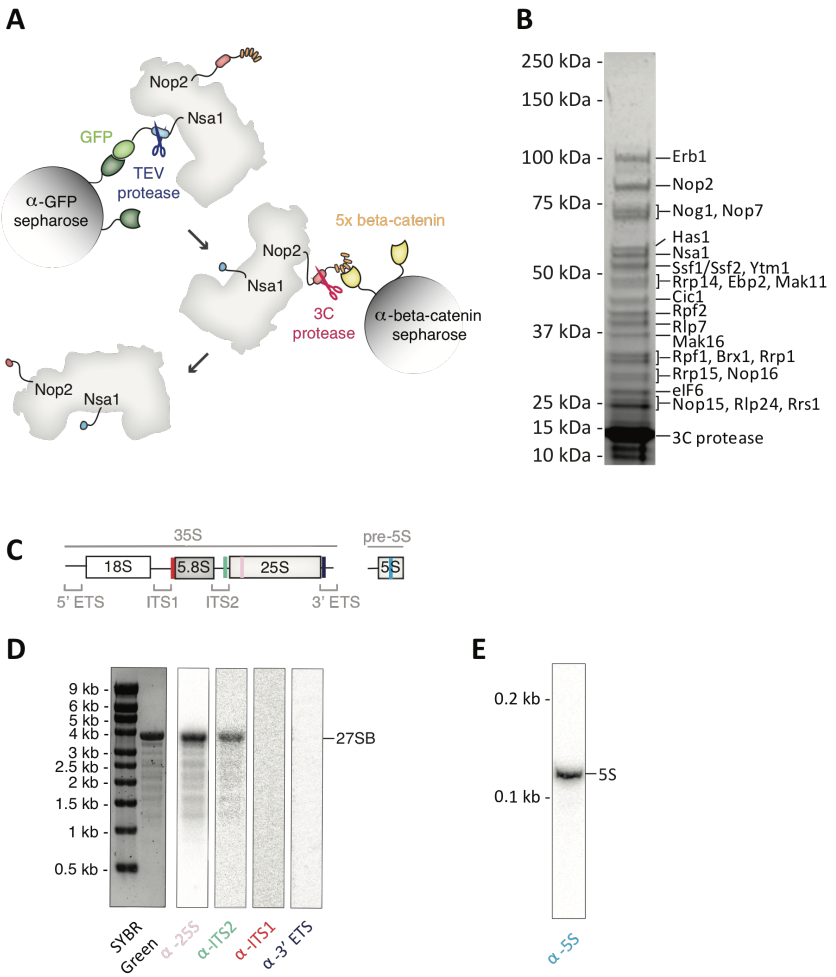

Figure 2.1 Purification of the 27SB containing pre-60S. A) Schematic of two step affinity purification of the pre-60S. **B**) A representative Coomassie-blue stained SDS-PAGE of the purified nucleolar pre-60S particles. Protein labels are based on in solution mass-spectrometry analysis of purified pre-60S particles and the approximate molecular weight. **C**) Diagram of the binding sites where the Northern Blot probes bind. **D**) Total RNA extracted from purified nucleolar pre-60S and visualized on an agarose gel and stained using SYBR-green II. Northern blot analysis was performed for the 25S, ITS2, ITS1 and 3' ETS RNAs. **E**) Total RNA was extracted from purified nucleolar pre-60S, separated on a Urea-PAGE, and Northern Blot analysis was performed for the 5S rRNA.

The 27SB pre-60S particles were assessed for stability and heterogeneity using negative stain electron microscopy. Here, the pre-60S particles looked homogenous in size and not prone to aggregation, but were clearly very flexible and heterogeneous in conformation (**Fig 2.2A**). A small negative stain dataset was collected and processed using EMAN2. 2D classification in ISAC revealed particles that appeared to have a several domains with some degree of mobility in their arrangements relative to one another (**Fig 2.2B**). Still, the relatively high concentration, homogenous size, and lack of aggregation made this pre-60S particle a promising target for structure determination using cryo-EM.

A

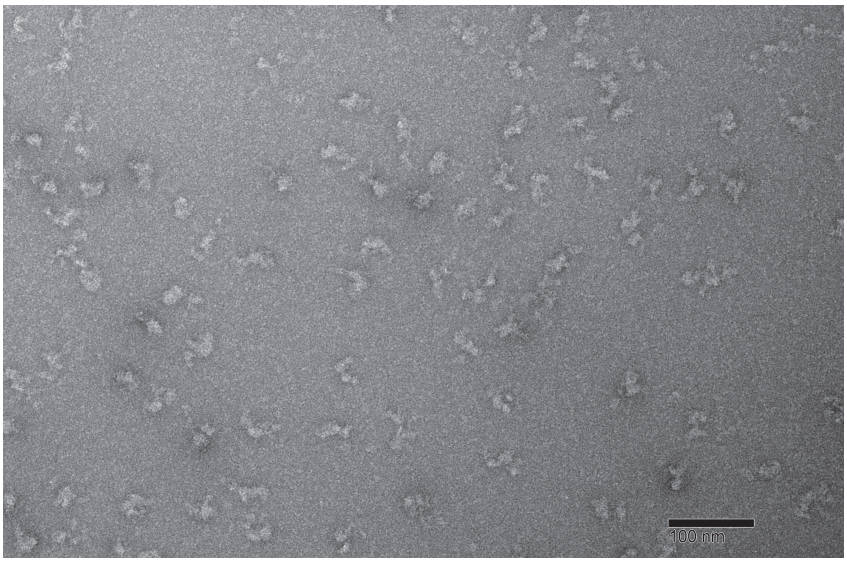

B

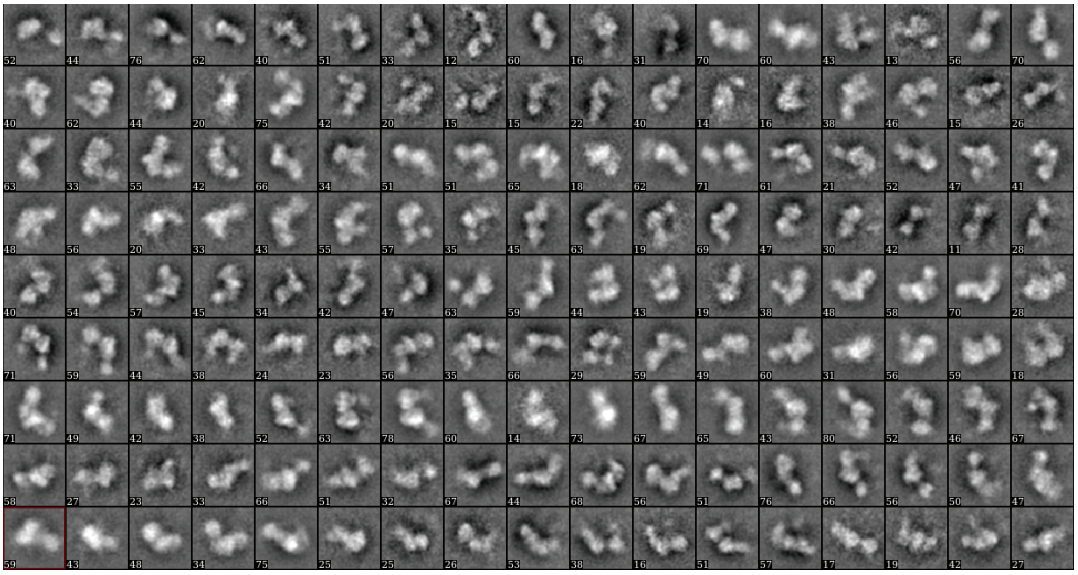

Figure 2.2 Negative stain analysis of the nucleolar pre-60S. A) Representative negative stain image of nucleolar pre-60S particles stained with 0.75% uranyl formate, imaged at ~52,000X magnification on a CM-10 transmission electron microscope. **B**) ISAC 2D classification of a negative stain data set of the nucleolar pre-60S. The 2D classification utilized 6,900 of the 8,500 picked particles.

2.2 Cryo-EM structure determination of several distinct states of the nucleolar pre-60S

Cryo-EM grid preparation was the most optimal using Lacey Carbon support grids. Cryo grid preparation was optimized using small datasets collected on the Talos Arctica microscope (**Fig 2.3A**). 2D classification of the particles from these datasets revealed a well-resolved knife shaped core linked to two areas that are smeared out and poorly resolved (**Fig 2.3B**). In attempts to reduce biases in orientations of the particles in the ice, cryo-EM grids were prepared where the purified pre-60s particles were supplemented with Triton X-100 detergent

to a final concentration of 0.1%. The sample was also supplemented with 5 mM $MgCl_2$, as we hypothesized magnesium could help stabilize RNA and reduce the observed flexibility in the sample. These supplemented samples were used in grid preparations for 3 out of 4 large data collections performed on the Titan Krios.

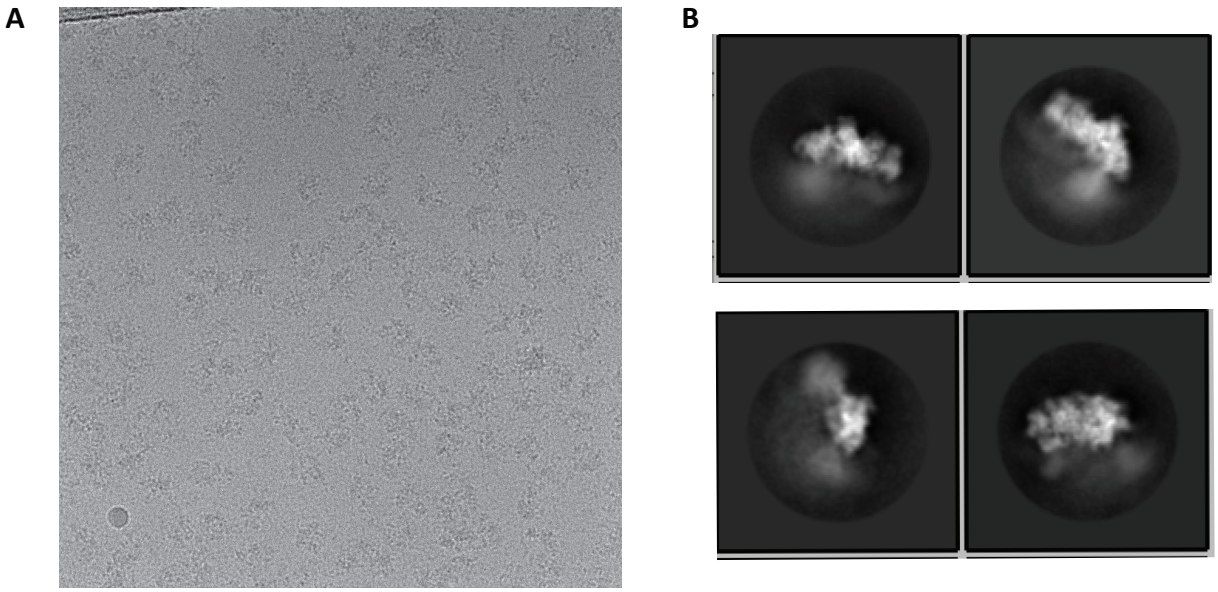

Figure 2.3 Cryo-EM studies of the nucleolar pre-60S reveal a well resolved core with flexible auxiliary domains. **A**) A cryo-EM micrograph of the nucleolar pre-60S sample. **B**) A selection of 2D averages of the pre-60S displaying the well resolved core and two flexible domains.

The processing of the large EM datasets was performed using Relion2, and is summarized in **Fig 2.4**. Here, effective 3D classification was initially achieved by analyzing our smaller Arctica datasets in Cryosparc, and utilizing Cryosparc's initial model generation tool (Punjani et al., 2017).

3D classification of the manually and computationally curated pre-60S particle datasets led to the discovery of a high-resolution core (3.4 Å) that was further sub-classified into three states, which were determined at resolutions of 4.3 Å (state 1), 3.7 Å (state 2) and 4.6 Å (state 3) (**Fig 2.4**, Table 7.1). These three states, together with cross-linking and mass spectrometry data, resulted in the identification of 21 ribosome assembly factors (Table 7.2).

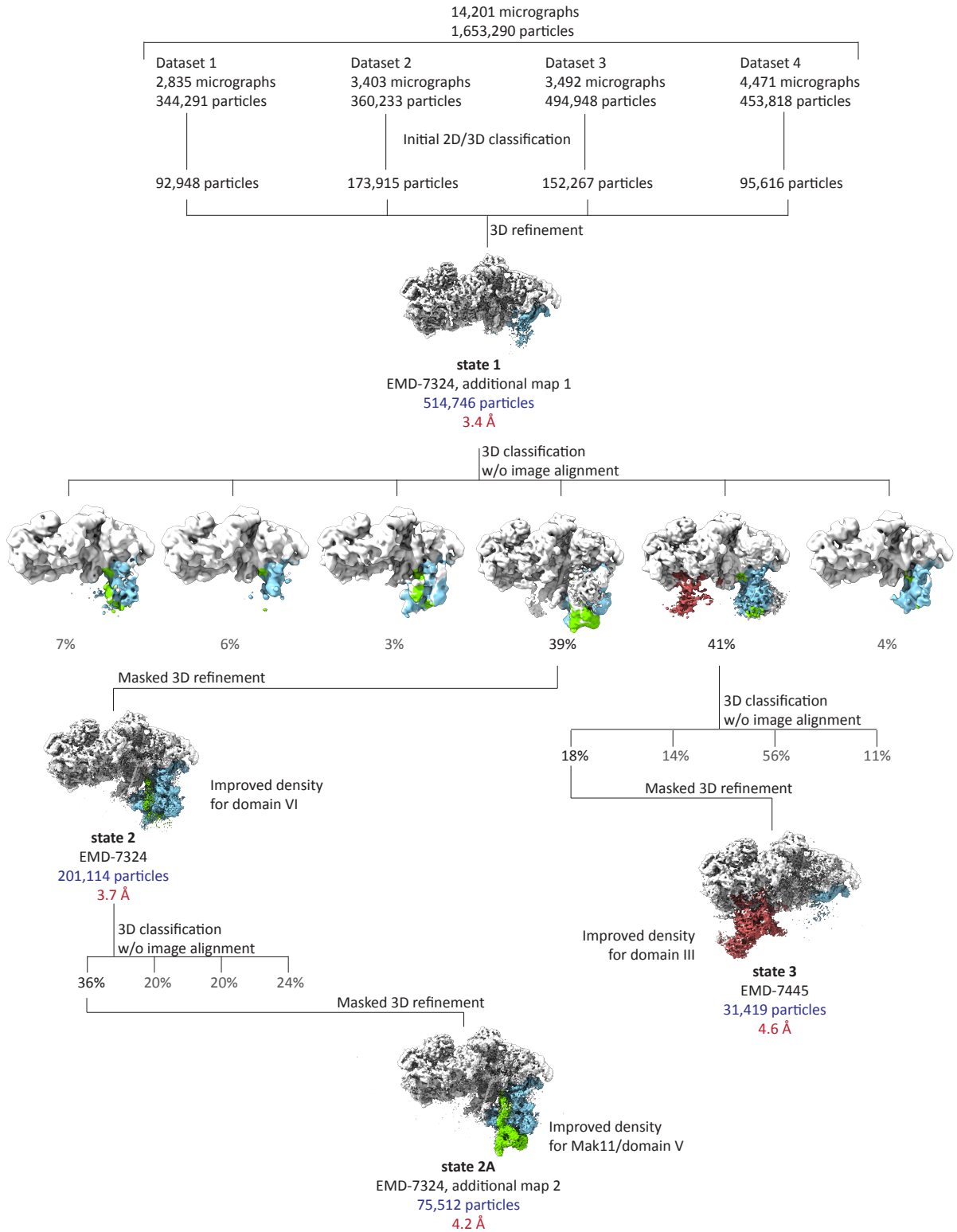

Figure 2.4 Analysis of the cryo-EM data of the nucleolar pre-60S reveals several distinct states. Schematic describing the cryo-EM data-processing workflow. Density regions corresponding to domain III (red), domain VI (blue) and Mak11 (green) are colored.

Atomic models could be completed for 18 of these proteins, while homology and poly-alanine models were used for proteins such as Ebp2, Mak11, and Ytm1, which were located in more flexible regions (Table 7.2, **Figure 2.5**).

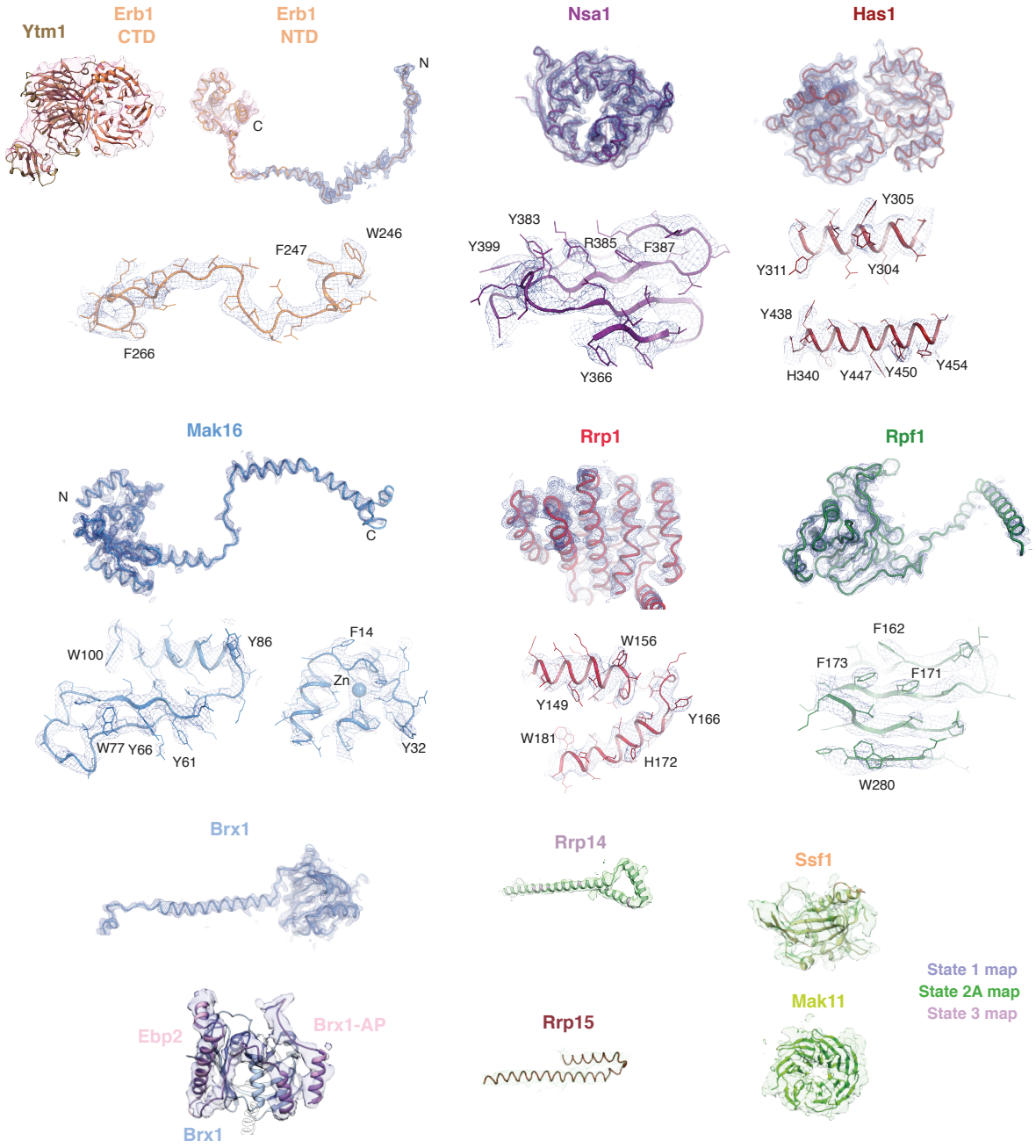

Figure 2.5 Cryo-EM density fit of selected assembly factors. Models of assembly factors visualized for the first time in our structures are shown here with their corresponding electron density from the state 1, state 2A, or state 3 map.

We observed three different conformational states of the 27SB rRNA. State 1 includes ordered density for ITS2 and domains I, II, and the 5.8S rRNA. State 2 additionally revealed density for domain VI, which is present in a near-mature folded state, but is in a conformation that is more distant from domain I than in the nuclear or cytoplasmic pre-60S particles (**Fig 2.6**). In contrast to state 2, state 3 lacks an ordered domain VI but features domain III (**Fig 2.6**). Although present, the majority of domains IV, V, and the 5S RNP were poorly resolved in all of the reconstructions, due to conformational flexibility. Low-resolution features corresponding to parts of domain V (helices 74–79) and its proximal assembly factor Mak11 can be seen in states 2 and 2A (**Fig 2.4**). The mature large subunit's solvent exposed side is largely made up of domains I and II, while the opposite side which interfaces with the small subunit is largely made up of domains IV and V. The subunit interface of the LSU contains the entrance for the polypeptide exit tunnel, sites to accommodate the amino-acyl ends of tRNA, and the peptidyl transferase center (**Figure 1.2**). Therefore, at the early stages of assembly in the nucleolus, the solvent exposed side of the LSU matures more rapidly than the subunit interface.

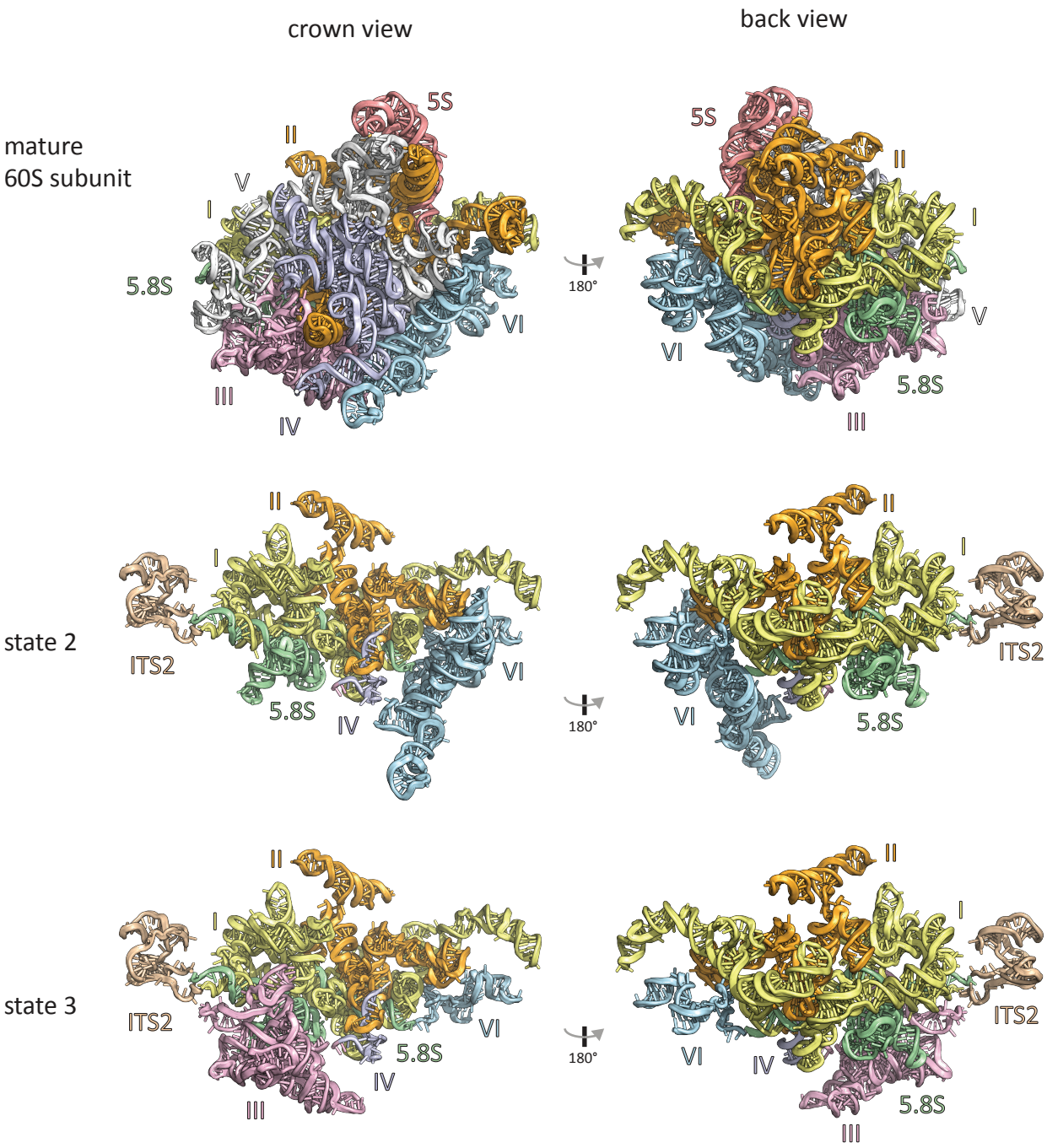

Figure 2.6 rRNA domains of state 2, state 3, and the mature 60S ribosomal subunit. The 5.8S rRNA, the 5S rRNA, and the domains of the 25S rRNA are color-coded and displayed in the crown and back view for each structure.

A striking feature of the nucleolar pre-60S particle is its open architecture where the solvent-exposed domains I, II and VI are encapsulated by a series of nucleolar assembly factors as visualized in state 2 (**Fig 2.7A**). Domains I, II, and VI are chaperoned by eight early ribosome assembly factors, which form a ring-like structure at the solvent-exposed side (**Fig 2.7B**). In particular, Brix- domain containing factors (Brx1, Rpf1 and Ssf1) act in conjunction with their respective binding partners (Ebp2, Mak16 and Rrp15) to interconnect these junctions and sterically prevent premature RNA-protein and RNA-RNA contacts (**Fig 2.7B**) This may be most clearly demonstrated at the site of Brx1•Ebp2 heterodimer binding, near the interface of domains I and II. Brx1•Ebp2 stabilize these domains while preventing the premature assembly of the LSU by steric hindrance. In this region, the domain I helix 22 base-pairs with domain V (helix 88) near a separate region of domain IV (helix 68) during later stages of LSU assembly (**Fig 2.7C,D).** In our structures, Brx1 remodels helix 22 of domain I to block the premature formation of this tertiary structure with helix 88. Further, Brx1 prevents the mature conformations of domain IV (helix 68), domain II (expansion segment 9) and the C-terminal region of Rpl13 in this region (**Fig 2.7C,D**). Folding of domains IV and V is critical for the formation of the subunit interface of the mature large subunit. In the mature ribosome, H68 and H69 contact the central and 3' minor domains of the 18S (Yusupov et al., 2001). Brx1•Ebp2 binding may be enforcing a more gradual maturation of these regions. Additionally, the binding site of Brx1•Ebp2 therefore proves that the flexibility in domains IV and V observed in our structures is not an artefact caused by the purification or data processing, but an important feature of the nucleolar stages of assembly.

Architectural support for the major interface between domains I and II is provided by the Brix-domain protein Rpf1 and its zinc-binding interaction partner Mak16 along with the helical repeat protein Rrp1 and the beta-propeller Nsa1. Rpf1 and Nsa1 occupy a region near the domain I binding site of Rpl17, while Mak16 and Rrp1 interface predominantly with ribosomal proteins Rpl4 and Rpl32 within domain II (**Fig. 2.7B**). Domains I, II, and VI are further chaperoned by the Rrp14 and the Brix-domain protein Ssf1 and its binding partner Rrp15. While the long C-terminal helix of Rrp14 bridges domains II and VI, the Ssf1•Rrp15 complex is positioned at the interface of domains I and VI (**Fig 2.7B**).

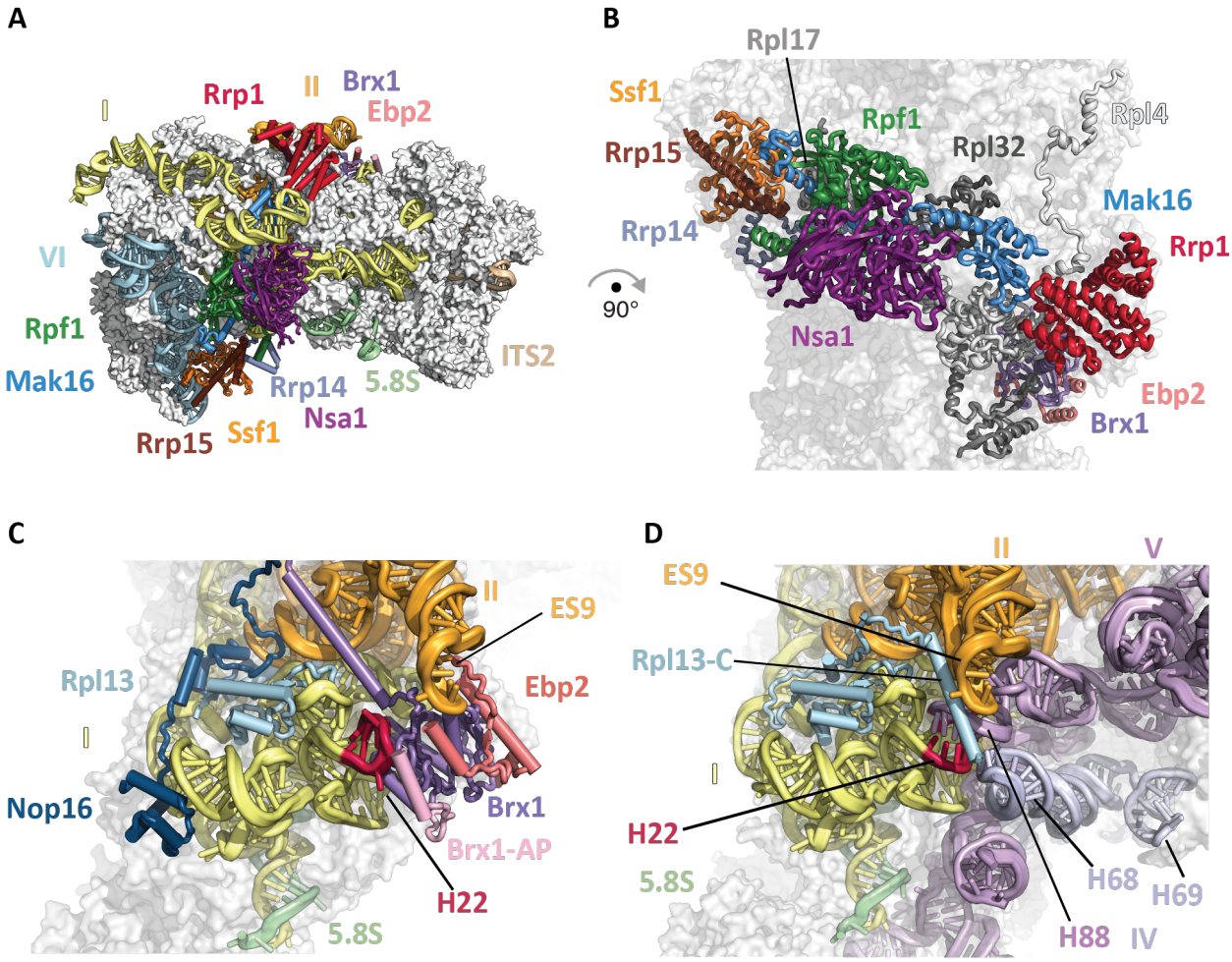

Figure 2.7: A ring of nucleolar assembly factors prevents premature folding of the 25S rRNA. (**A**, **B**) Assembly factors chaperone areas of domains I, II and VI and interact with ribosomal proteins. (**C,D**) Brx1 and Ebp2 remodel domain I (helix 22) to prevent binding of domain V (helix 88) and domain IV (helix 68) (**C**). These interactions exist in the Nog2-particle (PDB 3JCT) (**D**).

In state 3, we have identified the Erb1•Ytm1 heterodimer bound to domain III via Rpl27 (**Fig 2.7A**). For reasons discussed towards the end of this section (Chapter 2.3) and Chapter 5.1.2, we now believe state 3 may not be a true assembly intermediate of the pre-60S. Still, we can gain insight from the well resolved areas of this particle, in particular in the region of ITS2 and the nascent polypeptide exit tunnel. The N-terminal region of Erb1 (residues 239–397) wraps around the entire ITS2-domain I interface and is positioned underneath Nop16 and Has1 (**Fig 2.8A,B**). This location is in agreement with previous cross-linking data and explains why deletions within this region prevent the incorporation of Erb1 into pre-60S particles (Granneman, Petfalski, & Tollervey, 2011; Konikkat, Biedka, & Woolford, 2017). Nop16 interconnects RNA elements of the 5.8S rRNA and regions of domain I, and additionally contains a bipartite binding site by interacting with ribosomal proteins Rpl8 and Rpl13 (**Fig 2.8B**). The DEAD-box helicase Has1 is positioned at the interface of Rpl8, Cic1, Nop16 and Erb1 (**Fig 2.8B**). Assembly factors Cic1, Rlp7, Nop7, and Nop15 appear both in the nucleolar pre-60S particle and the Nog2-particle in largely the same conformation (**Fig 2.8B,C**).

The N-terminal segment of Erb1 employs molecular mimicry by binding to Nop7 in a similar fashion as Nop53 in the Nog2 particle, which uses a structurally related motif to bind to Nop7. This steric hindrance is exacerbated by the alternate conformation of the Rlp7 N-terminus that further prevents Nop53 binding (**Fig 2.8D,E**). Therefore, the coordinated mechanical removal of Erb1 and its proximal factors Ytm1, Nop16, and Has1 by Mdn1 is required before Nop53 can bind to the Nog2-particle and recruit the exosome-associated RNA helicase Mtr4 for ITS2 processing (Thoms et al., 2015; Baßler et al., 2010). The Has1 helicase may have acted upon its substrate at an earlier stage during the 27SA to 27SB transition. Alternatively, it may remodel flexible RNA elements in its vicinity for the ensuing 27SB processing (Dembowski et al., 2013). Unfortunately, our structures do not provide more insight into the potential targets of Has1's essential helicase activity.

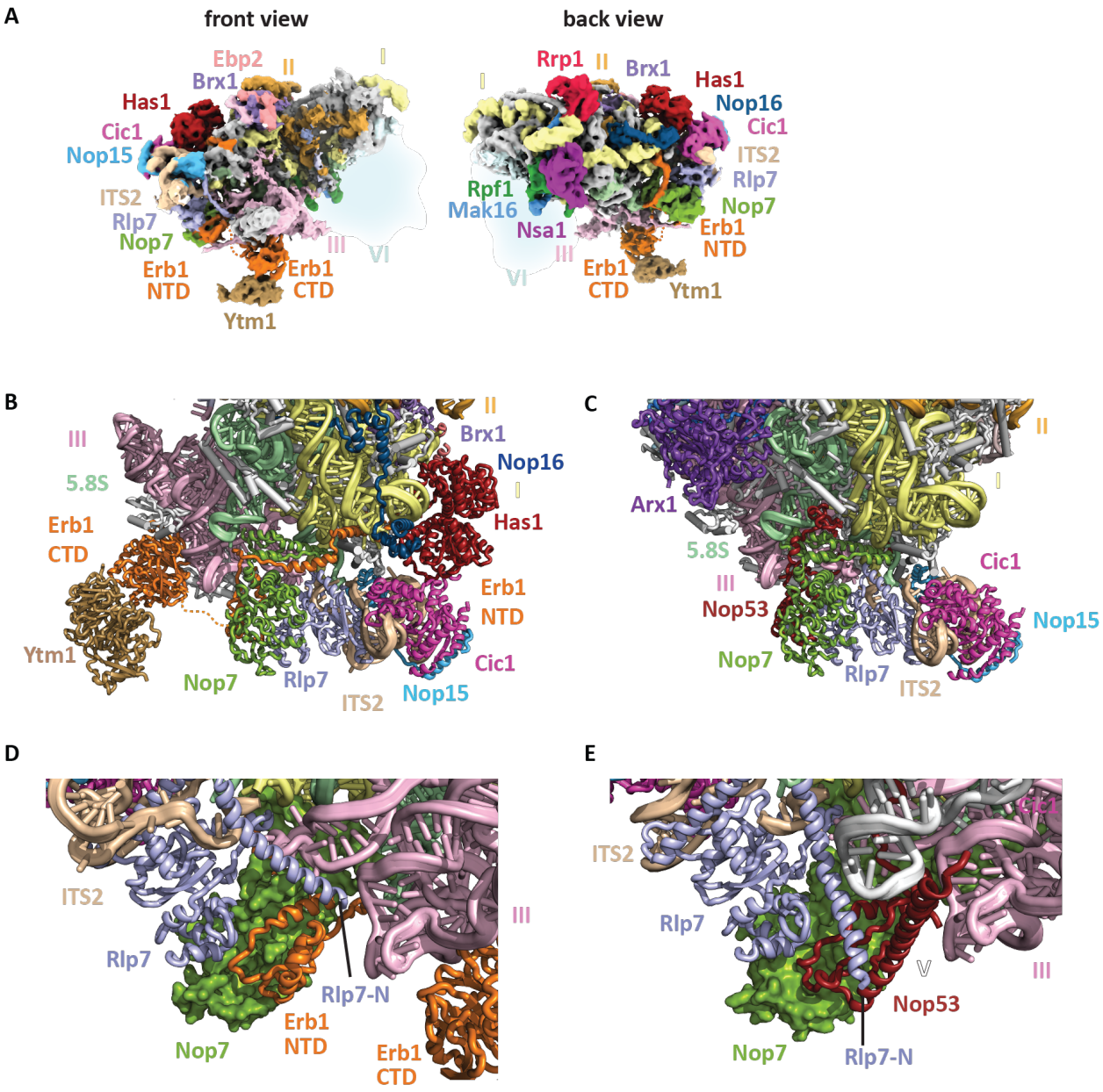

Fig 2.8 State 3 reveals an aspect of control over exosome recruitment to the pre-60S A) Two views of the state 3 cryo-EM map. (**B,C**) Cartoon representation of the ITS2 region in state 3 of the nucleolar pre-60S particle (**B**) and the Nog2-particle (PDB 3JCT) (**C**). (**D, E**) Focus on the region near Nop7 and Rlp7 near ITS2. The N-termini of Erb1 and Rlp7 in the nucleolar pre-60S particle prevent the binding of Nop53 (**D**), which binds to Nop7 in the Nog2-particle (**E**).

Examination of states 2 and 3 reveals two assembly intermediates of the polypeptide exit tunnel (**Fig 2.9A,B**). Ssf1, Rrp15, and Rrp14 are ordered in state 2 where they chaperone domains I and VI, that line two sides of the forming polypeptide exit tunnel (PET) (**Fig 2.9A**). By contrast, domain VI, Ssf1, Rrp15 and Rrp14 are disordered in state 3. Here, Ytm1 and Erb1 chaperone domain III, which adopts a mature conformation with respect to domain I to form a different intermediate of the PET (**Fig 2.9B**). Subsequent maturation steps of the nucleolar pre-60S must

involve the joining of domains III and VI and the formation of the PET on the solvent exposed side. This may be accompanied by chaperoning of the nascent PET via the insertion of the Nog1 N-terminus and the replacement of Ssf1•Rrp15 by Rpl31, as observed in the Nog2 particle (**Fig 2.9C**). Nog1 has already been recruited to the pre-60S at this point in assembly, poised to chaperone the nascent polypeptide exit once it is formed.

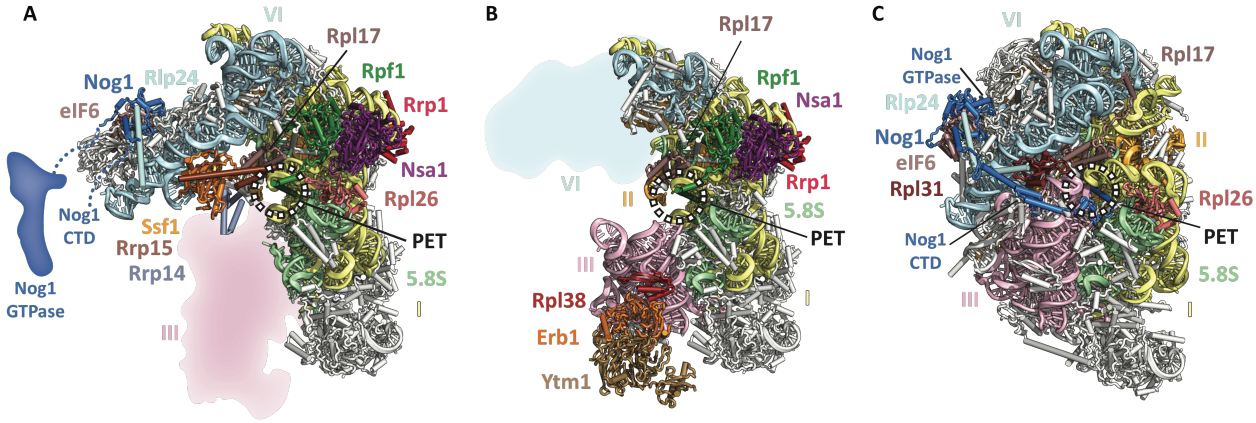

Figure 2.9 Nucleolar pre-60S structures reveal different intermediates of the polypeptide exit tunnel. View of the nascent polypeptide exit tunnel in (**A**) state 2, (**B**) state 3, and (**C**) the Nog2 particle (PDB 3JCT).

2.3 Further information on nucleolar pre-60S assembly revealed by complementary structures

At the time of our publication of the nucleolar pre-60S particles, complementary structures of 27SB pre-60S particles were published by the Ye lab and the Hurt & Beckmann labs. The Ye lab identified one structure that corresponds to our State 2 (Zhou et al., 2018). Structures from the Hurt and Beckmann labs spanned a wider scope of nucleolar assembly, identifying structures corresponding to our State 1 and 2, and two additional states corresponding to later intermediates where domains IV and V become stably folded, referred to as states C through E (Kater et al., 2017) (**Fig 2.10**).

Comparison of our structures to complementary data published by the Hurt and Beckmann labs of nucleolar pre-60S revealed an even more extensive role of Erb1. The Brx1 associated peptide in our state II that could not be confidently identified due to limiting resolution (**Fig 2.7C**) was in fact Erb1. Additionally, states D/E revealed that partial stable folding of domains III, V, and VI can occur while Brx1•Ebp2 is still bound, after the binding of additional factors Nip7, Noc3, Nop2, and Sbp1 (**Fig 2.10**).

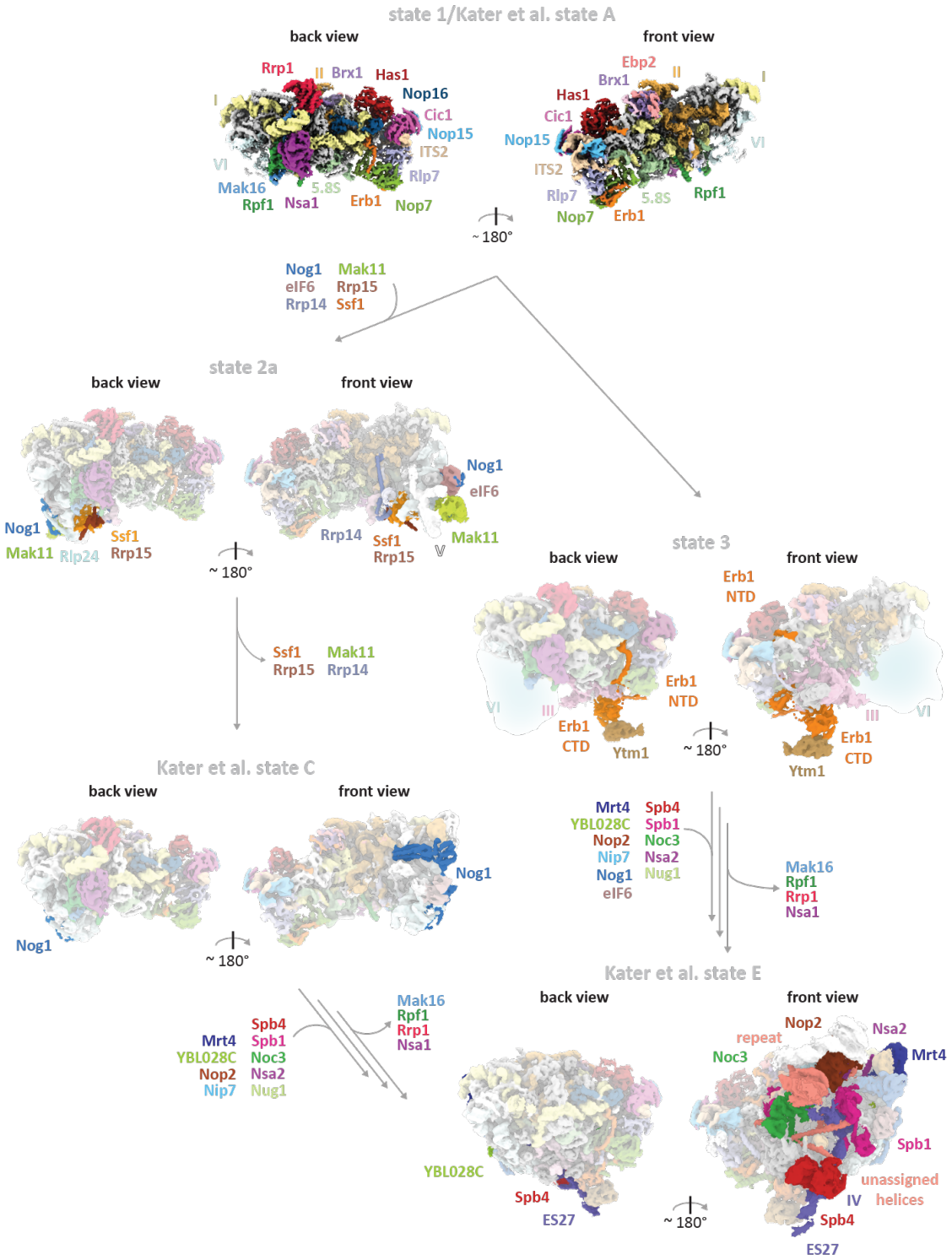

Figure 2.10 Schematic of the various states of the pre-60S observed in our work and Kater et al.'s work. Our state 1 closely resembles state A from Kater et al.'s work. State 2 most closely resembles Kater et al.'s state B, but our state 2a contains additional density for Mak11, Rrp15, Ssf1, Rrp14, Nog1, and eIF6. State 3 was unique to our work, while states C and E were unique to Kater et al.

Both of the complementary works purified their particles from *Saccharomyces cerevisiae* in the exponential growth phase, unlike our pre-60S which were isolated under nutrient stress conditions. Close inspection, which is limited by the resolution of the available data, does not reveal any clear differences between corresponding states despite the difference in purification conditions. The nature of the particles that accumulate under nutrient deprivation is discussed in Chapter 5.1.3. Of note, is that Kater et al. did not find a particle corresponding to our state 3 in their data. In addition to the differences in growth conditions, a key difference in our purifications of the nucleolar pre-60S was buffer composition. Our purifications began with buffer containing 1 mM EDTA whereas Kater et al. purified with buffers containing 5 mM $MgCl_2$. The EDTA in our buffers may have stripped magnesium from some RNA or proteins in our sample, and therefore destabilized certain states or areas of the pre-60S particles we purified. If this is the case, state 3 may be some sort of breakdown product of state D, where Erb1 and Ytm1 are present at the same time as Nsa1/Rpf1/Rrp1/Mak16, but both domains III and VI are folded (Kater et al., 2017). The nature of state 3 is also discussed further in Chapter 5.1.2.

2.4 Conclusions

Nucleolar 60S ribosome assembly necessitates assembly intermediates where different rRNA domains are assembled in a modular fashion. Our understanding of this very early stage of assembly continues the trends observed for later stages of pre-60S assembly, where the solvent exposed side of the pre-60S matures sooner in the biogenesis process than the subunit interface side, where the active sites like the polypeptide exit tunnel and the peptidyl transferase center mature more gradually. The structures of the eukaryotic nucleolar pre-60S highlight the high degree of control that is exerted to prevent the premature formation of inter-domain contacts of ribosomal RNA, illustrate how a chronology of assembly factors is enforced, and illustrate how the nascent active sites of the LSU are protected by assembly factors. These overarching themes exist for nucleolar stages of both small and large subunit biogenesis (Barandun et al., 2017).

Chapter 3:
Structural and biochemical characterization of Dhr1 helicase and its activation by Utp14

The SSU processome is the pre-ribosomal particle containing the pre-18S not yet cleaved at A1, and the U3 snoRNA (see Chapter 1.2.2). The U3 snoRNA basepairs with regions of the 5'ETS and the 5' and central domains of the pre-18S. Binding to U3 is in part responsible for enforcing an open architecture of the pre-18S domains and preventing the folding of the central pseudoknot at this early point in SSU assembly (See Chapter 1.2 and **Fig 1.7).** Therefore, in order for proper maturation and compaction of the 18S domains, removal of the U3 snoRNA from the assembling small subunit is critical. The DEAH-box helicase Dhr1 is the assembly factor responsible for this removal (previous work on the Dhr1 helicase is expanded on in Chapter 1.3). At the start of this work, an understanding of the mechanism of how Dhr1 interacts with the pre-small subunit to bind and unwind the U3 substrate was unclear. Further, although there was evidence of the assembly factor Utp14 being critical for Dhr1 recruitment to the SSU processome and for Dhr1 activation, the mechanisms of these interactions were also unclear. Our goal was to understand the general architecture of Dhr1 helicase and to understand in greater mechanistic detail the activation of Dhr1 by Utp14.

Malik Chaker-Margot helped me design and clone constructs of Dhr1 and helped me optimize the purification of Dhr1 helicase core for structural studies. Sebastian and Malik fished and cryo-protected the Dhr1 core crystals for data collection at the NSLS-II beamline. Malik also helped build the structure of the Dhr1 core, and constructed several of the plasmids expressing Dhr1 variants with GFP tags used for in vivo assays. I performed all other cloning, protein purification, and biochemical analysis for various Utp14 and Dhr1 constructs. Deena Oren is responsible for the fishing and cryo-protection of almost all Dhr1-Utp14 crystals. She also ran the remote synchrotron sessions with me for all the attempts at co-crystallizing Dhr1 and Utp14 at the NSLS-II beamline and APS beamline. Data from these collections resulted in an additional structure of Dhr1 with the C-terminal domain resolved, which I subsequently built and refined. Sameer Singh and Arnaud Vanden Broeck have pioneered the study of ribosome assembly in human cells in our lab, and the structure of the Dhr1 helicase core presented here has been incorporated into their recent manuscript on maturing small subunit processomes from human cells.

3.1 Dhr1 contains a Dhr1-specific loop

To begin to study Dhr1 helicase, a careful consideration of its sequence and homology to other members of the DEAH-box helicase family was necessary (see chapter 1.3.1 on DEAH-box helicases). Close examination of the conserved DEAH-box core revealed an 84 amino acid stretch within the RecA2 domain that contained many negatively charged residues. This stretch is located between helicase motifs IV and V but was not found in any other DEAH-box helicases examined (**Fig 3.1A,B**). Intriguingly, this stretch is present in all Dhr1 homologs, consistently contains many negatively charged residues, and is especially well-conserved among Dhr1 homologs in metazoans (**Fig 3.1C**). Our first course of action to understand the role of this unusual sequence and further our overall understanding of Dhr1 was to crystallize Dhr1 helicase.

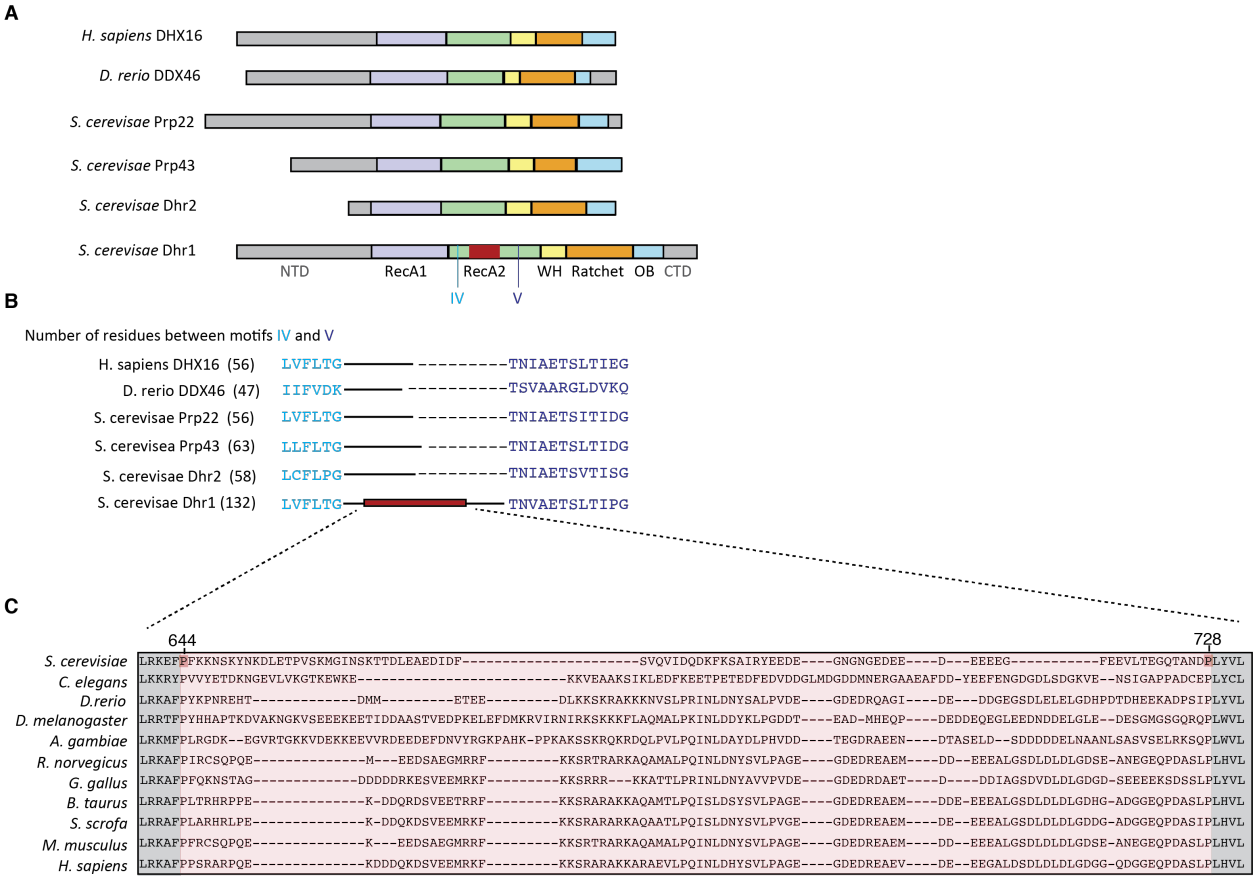

Figure 3.1 The Dhr1-loop is conserved among Dhr1 homologs but not other DEAH-helicases. **A**) Schematic of the structural domains of several non-Dhr1 homolog DEAH helicases. The location of the Dhr1-specific loop is highlighted in red, and the location of motifs IV and V within the RecA2 domain are labeled in blue. **B**) The Dhr1 loop is located between motifs IV and V. The number of amino acids between motifs IV and V in several other DEAH helicases is diagrammed here, to scale. **C**) Sequence alignment of Dhr1 homologs from several species. The region corresponding to the Dhr1-specific loop is highlighted in light red. The pink residues mark the beginning and end of the loop in *S. cerevisiae* Dhr1.

3.1.1 Crystallization of the Dhr1 helicase core reveals the Dhr1-specific loop

In order to obtain Dhr1 protein of sufficient purity and quantity for use in crystallographic and further biochemical studies, several constructs of Dhr1 were overexpressed in *E. coli*. In an attempt to facilitate crystallization, a construct of Dhr1 containing only the helicase core (N- and C-terminal extensions were truncated) was utilized. The Dhr1 helicase core was successfully crystalized in the presence of ADP-Mg. Similar to other DEAH-box helicases of the SF2 superfamily, the Dhr1 core contains the RecA1, RecA2, Winged Helix, Ratchet-like and OB-fold domains. The ADP molecule is wedged between the two RecA domains, as previously observed for other DEAH-box structures (**Fig 3.2A,B**). Intriguingly, the Dhr1-specific 84 amino acid loop within the RecA2 domain winds between the RecA2 and Ratchet-like domains (**Fig 3.2**).

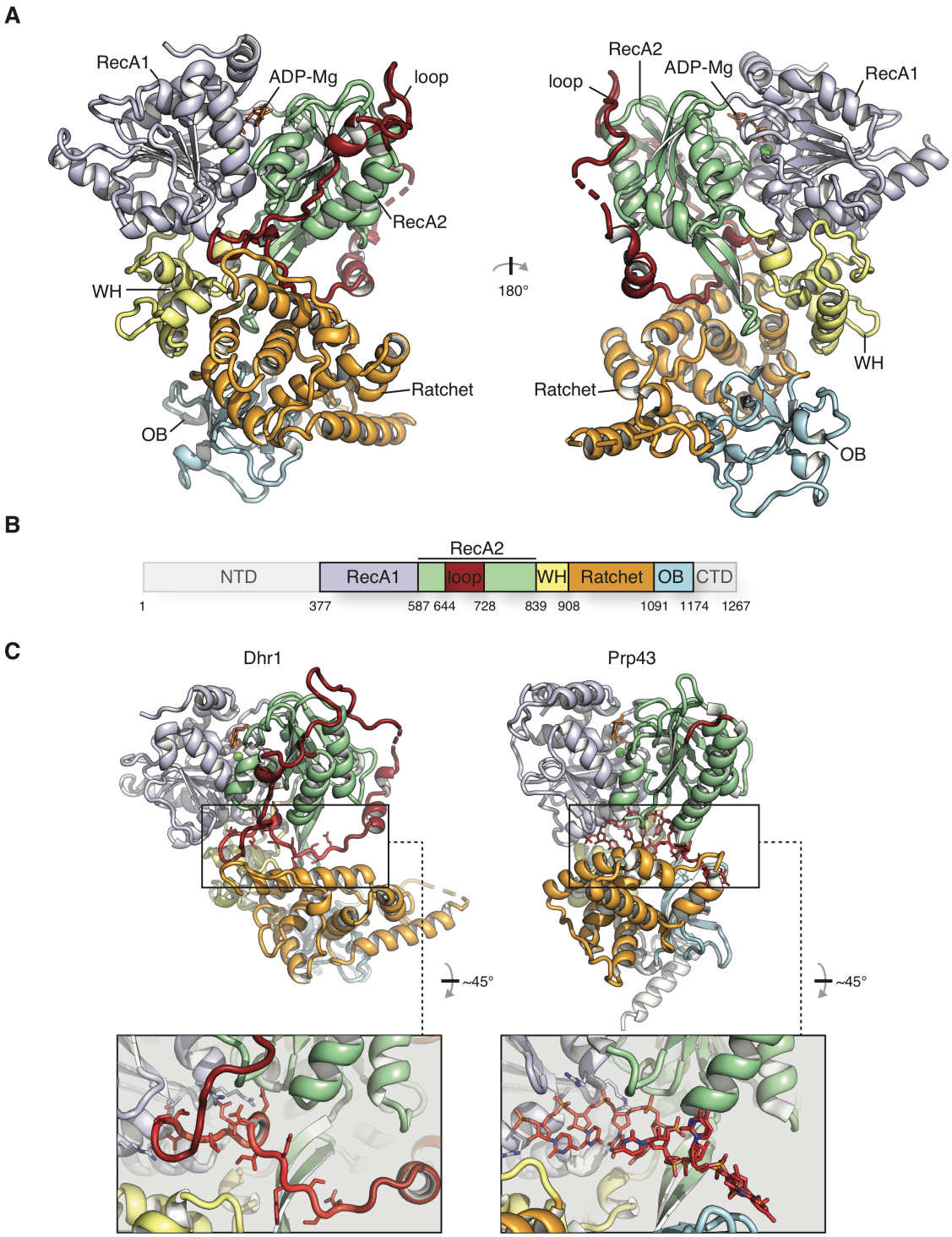

Figure 3.2 Structure of yeast Dhr1 helicase core reveals a loop that occupies the substrate-binding cleft. A) Structure of Dhr1 bound to ADP, with helicase core domains labeled. WH= Winged Helix. **B**) Domain architecture of Dhr1, regions missing from the crystallization construct are in gray. **C**) Comparison of Dhr1 and Prp43-U7-ADP-BeF_3. Insets highlight the substrate-binding cleft with the loop or RNA and select residues of the RecA1 domain shown as sticks.

A comparison of Dhr1 with the structurally well-characterized DEAH-box helicase Prp43 in its RNA- and ADP-BeF_3–bound forms (Tauchert et al., 2017) provides insights into the function of the Dhr1-specific loop (**Fig 3.2C, Fig 3.3A**). The Dhr1-specifc loop binds in the same cleft that is occupied by the poly-Uracil RNA in the closed conformation of Prp43 (**Fig 3.2C**) and further interacts with residues of DEAH motifs Ia and Ib, which typically interact with the substrate RNA backbone (**Fig 3.3**). Surprisingly, the binding of the loop in Dhr1 favors an open conformation of the enzyme with a dramatic rearrangement of the Ratchet-like and OB-fold domains that has only been observed in ATP-bound forms of Prp43 (**Fig 3.4A**). Taken together, we hypothesize that the Dhr1-specific loop is a negative regulatory element that, when bound, occupies the RNA-substrate cleft and maintains the enzyme in an open conformation poised for RNA-substrate engagement.

A

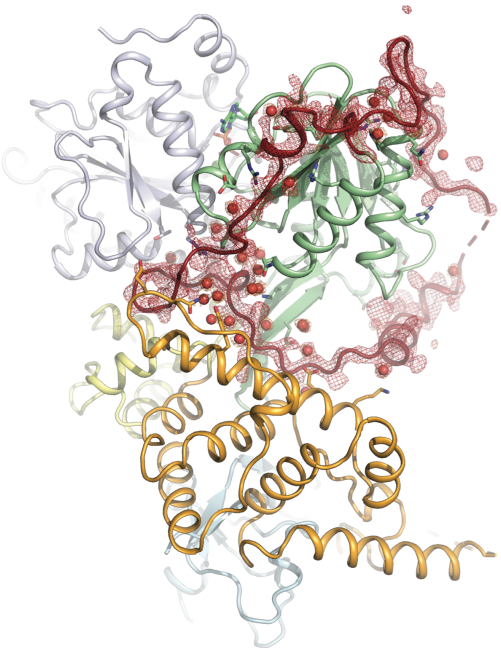

B

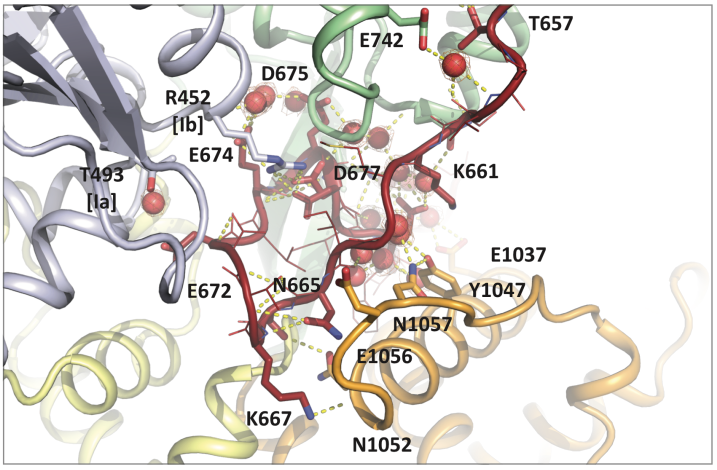
T657
E742
D675
R452
[Ib]
E674
T493
[Ia]
D677
K661
E1037
E672
N665
Y1047
N1057
E1056
K667
N1052

50°

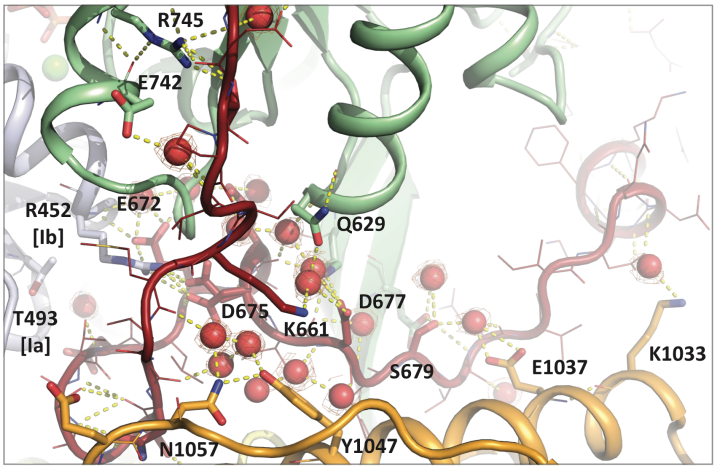
R745
E742
R452
[Ib]
E672
Q629
T493
[Ia]
D675
K661
D677
S679
E1037
K1033
N1057
Y1047

Figure 3.3 Residues from the RecA1, RecA2, and Ratchet-like domains interact with the loop directly or via coordinating waters. A) The 2Fo-Fc electron density map for the loop and coordinating waters is contoured at 1.6 σ and shown as red mesh. **B**) Residues from other domains that interact with the loop directly or via coordinating waters are shown as sticks, including residues of motif Ia (R452) and Ib (T493).

Since the structure of the Dhr1 core was attained, two additional crystal structures of Dhr1 have been solved (Boneberg et al., 2019; Roychowdhury et al., 2019). One of these was *S. cerevisiae* Dhr1 in the absence of ADP and in the absence of the loop. Here, the loop and several other linker regions had been removed as proteolysis digestion was used in order to facilitate crystallization. The CTD of Dhr1 was present, and visualized, revealing the overall fold of the yeast Dhr1 CTD. The second structure was of the *Mus musculus* homolog of Dhr1, DHX37. This structure revealed DHX37 bound to ssRNA. Comparison of our loop-bound structure to these Dhr1 structures reveals the same trend as comparisons to the various structures of Prp43 (**Fig 3.4B**). The Dhr1-loop bound structure is the most open, the "apo" Dhr1 bound to no loop or nucleotide has a core in a moderately closed state, and the RNA-bound DHX37 features the most closed core structure.

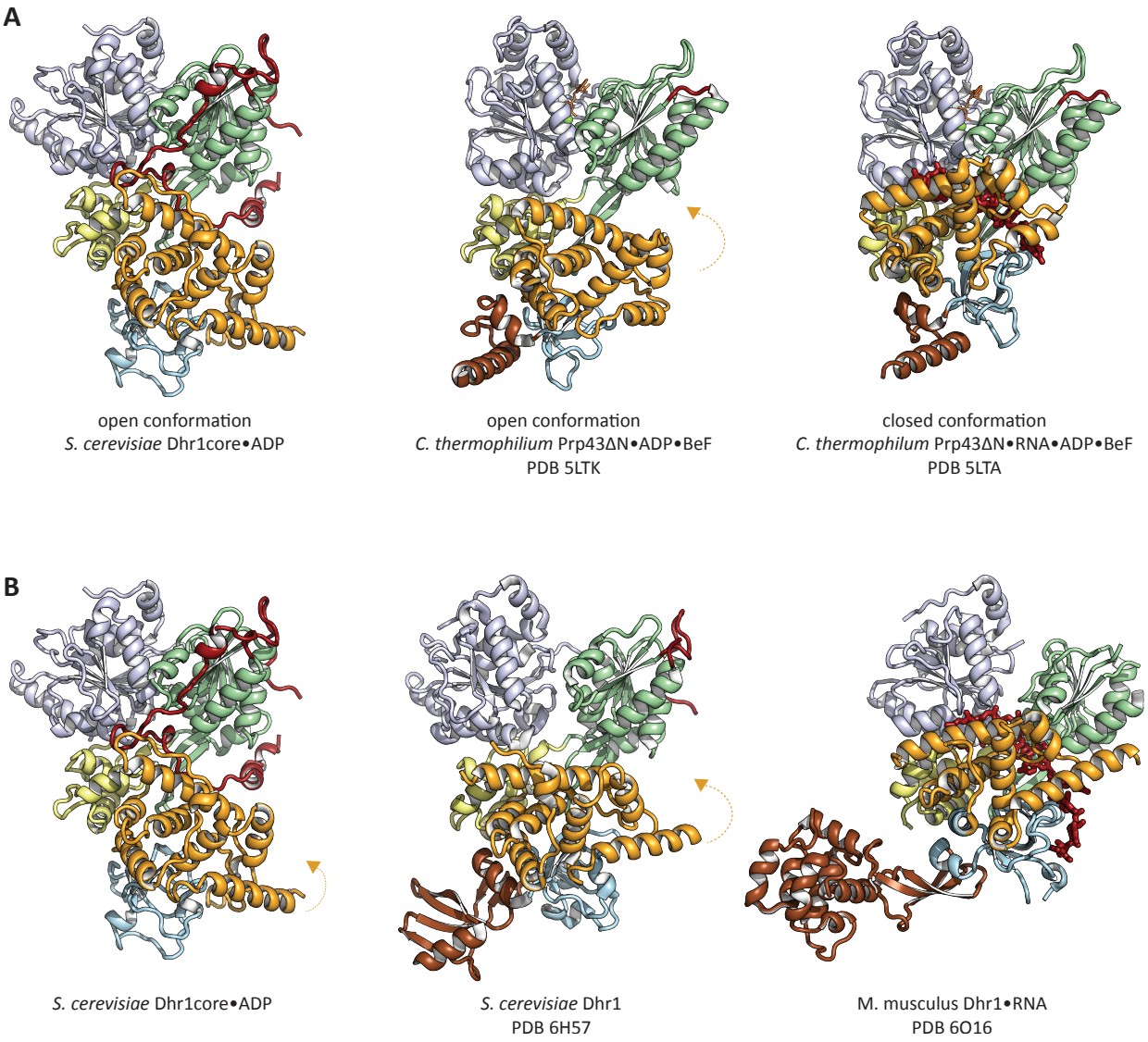

Figure 3.4 The Dhr1-specific loop confers an "open" state to the helicase. A) Comparison of Dhr1 with the open (PDB 5LTK) and closed (PDB 5LTA) structures of Prp43, domains colored as in Figure 1. **B**) Comparison of the published Dhr1 structures. The orange arrow indicates the movement of the Ratchet-like domain between the open, intermediate (B only), and closed conformations.

3.1.3 In vivo assays show the Dhr1 specific loop is non-essential, while Dhr1 CTD is essential

We further probed the role of the Dhr1-specific loop *in vivo* by performing yeast genetic studies in a Dhr1-depletable yeast strain. The deletion of the Dhr1-specific loop did not display any growth phenotype at 23 ˚C, 30 ˚C or 37 ˚C, as expected for the removal of a negative regulatory element (**Fig 3.5A**). By contrast, truncation mutants of Dhr1 either lacking the CTD or containing only the CTD exhibited lethality (**Fig 3.5A**). To test if the essential function of the CTD is solely to promote Utp14 binding and hence recruitment of the Dhr1 core to the SSU processome, we expressed Dhr1ΔCTD fused directly to Utp14 in the Dhr1 depletable strain. Since this fusion protein exhibited lethality, the functional role of the CTD likely extends beyond

recruitment of Dhr1 to the SSU processome and may include additional functions that require separation from Utp14 (**Fig 3.5A**). Expression of the different Dhr1 constructs in the yeast cells was confirmed using Western Blotting (**Fig 3.5B**). The essential nature of the CTD was also observed by Roychowdhury et al., who also expressed Dhr1 variants in yeast cells depleted of wild type Dhr1. Interestingly, they found that deletion of the entire CTD caused cell death, but deletion of the CTD except for alpha helix 24 (residues 1175-1188), partially complemented cell growth (Roychowdhury et al., 2019).

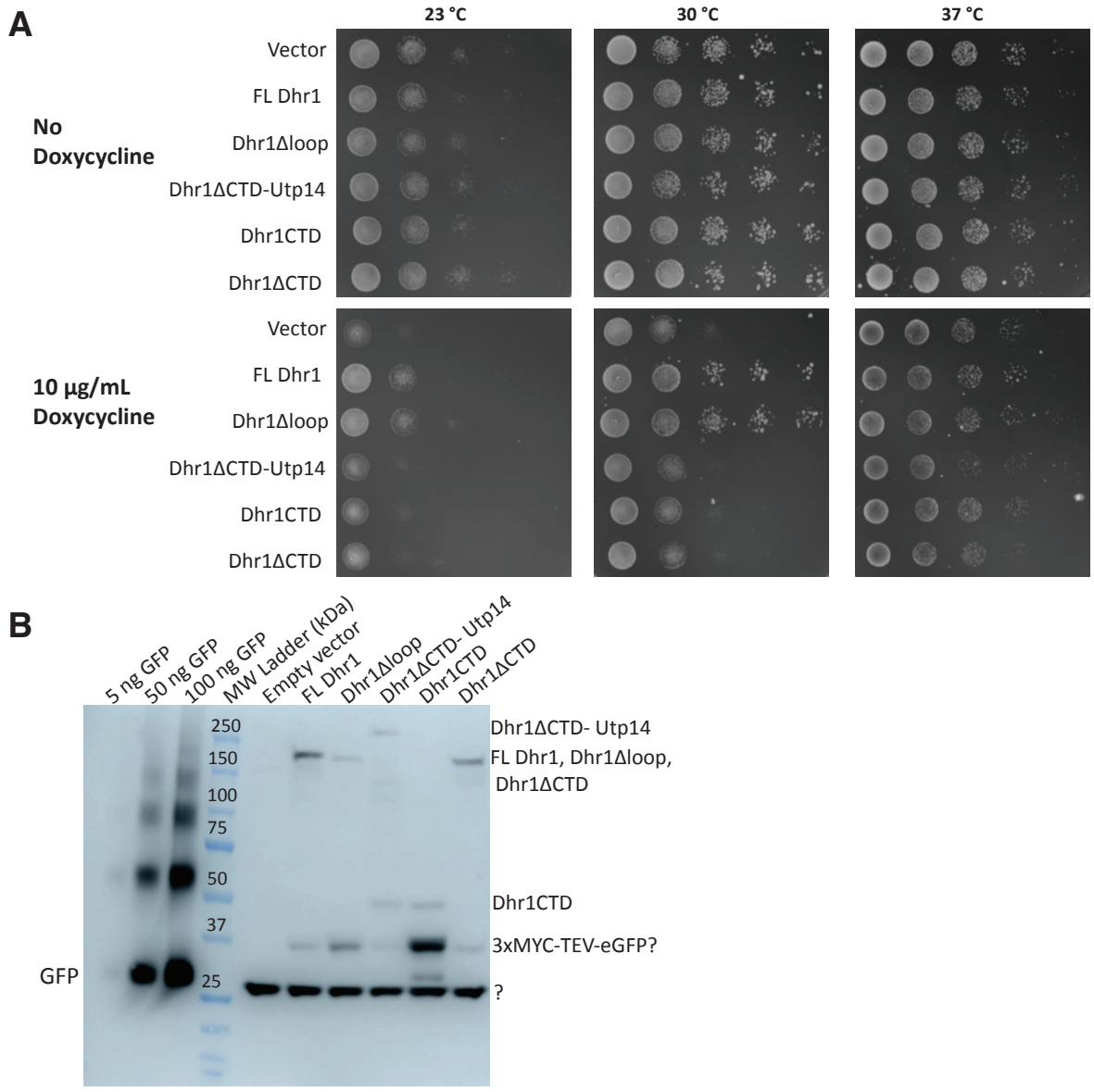

Figure 3.5 The Dhr1 specific loop is not essential to cell viability, while the Dhr1 CTD is. A) Serial dilutions yeast colonies where the indicated constructs of Dhr1 were expressed from plasmids and native Dhr1 was depleted in the presence of doxycycline, grown for 40 hours at the indicated temperatures. **B**) Western blot for anti-GFP, showing expression of Dhr1 constructs from A.

3.1.4 Auto-inhibited Dhr1 visualized in context of small subunit intermediates

Despite the wealth of information on the arrangement of the U3 snoRNA provided by the SSU processome structures, it remained unclear how Dhr1 could gain access to the U3 snoRNA and remove it from these structures. It was hypothesized that overall rearrangements and further maturation of these particles must occur in order for Dhr1 action. Recent data from the Hurt and Beckmann labs revealed several snapshots of assembly between the small subunit processome and the point of Dhr1 engagement with its substrate (Cheng et al., 2020). These structures show the change in composition of the SSU processome after A1 cleavage and exosome-mediated processing of the 5'ETS. These states are referred to as "Pre-A1", "Post-A1", referring to the status of A1 cleavage, followed by "Dis-A", "Dis-B" and "Dis-C" states, where "Dis" refers to the "disassociation" of early assembly factors (**Fig 3.6**).

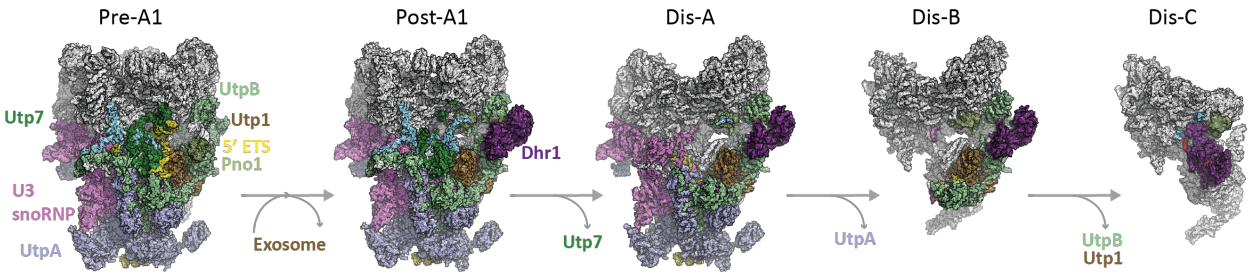

Figure 3.6 Dhr1 visualized in context in maturing small subunit processomes from yeast. Progression of states Pre-A1 to Dis-C from Cheng et al., highlighting the subcomplexes of the SSU processome (U3 snoRNP, UtpA, UtpB) and several key proteins that interact with Dhr1 or Utp14 (Utp7, Pno1, and Utp1 (part of UtpB). PDB 6ZQC (Pre-A1),6ZQD (Post-A1), 6ZQE (Dis-A), 6ZQF (Dis-B), and 6ZQG (Dis-C).

This work was particularly interesting, as Dhr1 was finally visualized in context of a pre-small subunit in four of these states. Additionally, regions of Utp14 that were not previously visualized in the context of the SSU processome were also revealed. Reanalyzing these structures in light of our biochemical and structural studies of Utp14 and Dhr1 revealed the regulation and activity of these factors at this junction of SSU assembly. In the Post-A1, Dis-A, and Dis-B states, Dhr1 helicase core is anchored to the periphery of the particle, away from its substrate U3 snoRNA. Dhr1 was observed in an open conformation that Cheng et al. hypothesized was due to ADP binding by the core. They also hypothesized that binding to nearby assembly factor Pno1 by the RecA2 domain was partially responsible for enforcing this open state of the enzyme. We re-examined the electron density in the proximity of Dhr1 in states Post-A1, Dis-A and Dis-B, and found that the Dhr1 apo structure did not fit into the density as well as our crystal structure of auto-inhibited Dhr1 occupies this density. The overall conformation of the loop-bound core fit more optimally into the density, and there is evidence of density for segments of the loop (**Fig 3.7**). This further supports our hypothesis that the loop-bound conformation of Dhr1 is the auto-inhibited state, as Dhr1 is loop-bound in context of the pre-SSU when it is sequestered from its substrate. Further, the open conformation of the loop is not caused ADP binding, as hypothesized by Cheng et al., but is enforced by the binding of the Dhr1-specific loop in the RNA substrate tunnel.

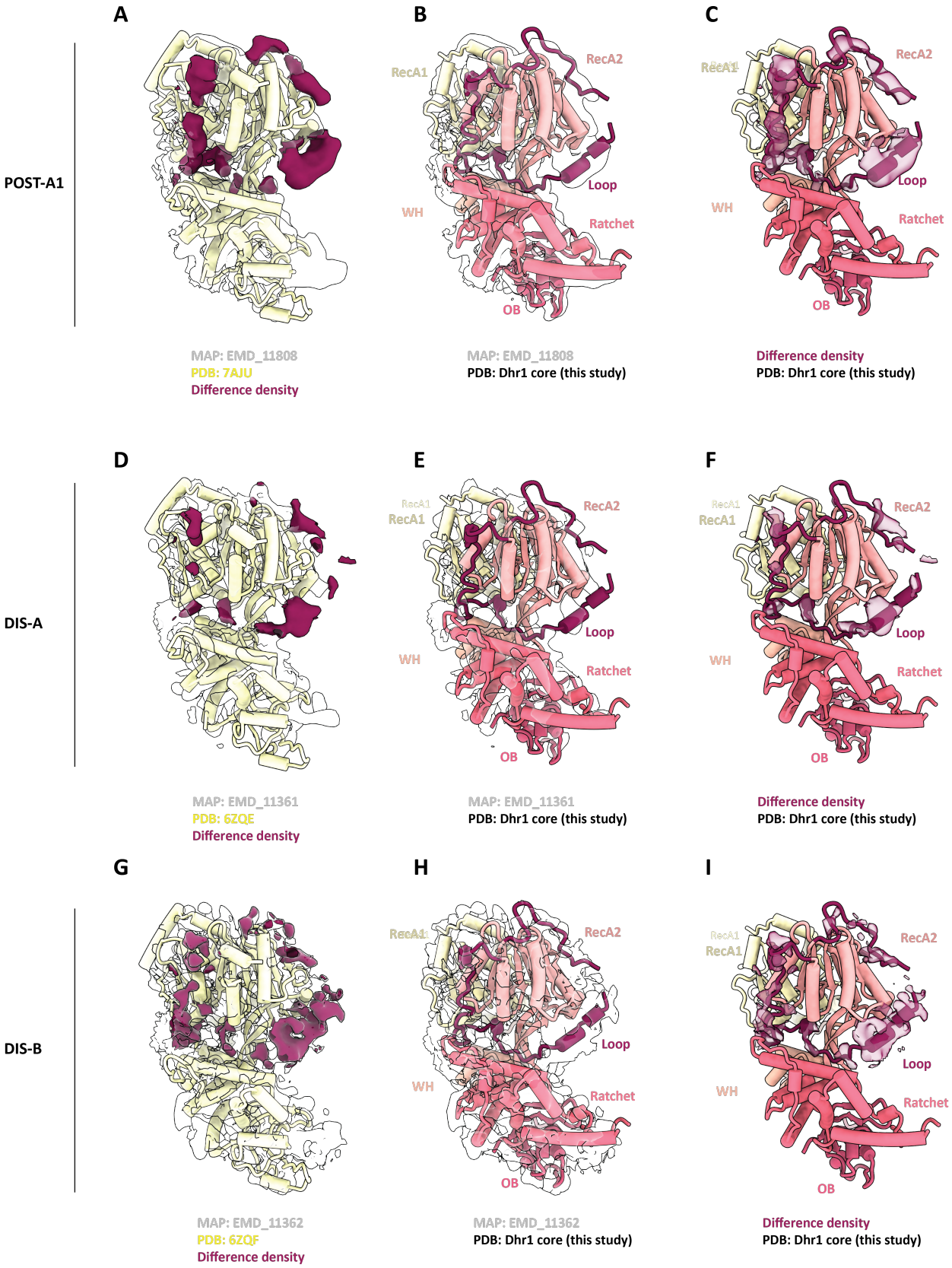
A
B
C
POST-A1
RecA1
RecA2
Loop
WH
Ratchet
OB
MAP: EMD_11808
PDB: 7AJU
Difference density
MAP: EMD_11808
PDB: Dhr1 core (this study)
Difference density
PDB: Dhr1 core (this study)
D
E
F
DIS-A
MAP: EMD_11361
PDB: 6ZQE
Difference density
MAP: EMD_11361
PDB: Dhr1 core (this study)
Difference density
PDB: Dhr1 core (this study)
G
H
I
DIS-B
MAP: EMD_11362
PDB: 6ZQF
Difference density
MAP: EMD_11362
PDB: Dhr1 core (this study)
Difference density
PDB: Dhr1 core (this study)

Figure 3.7 Dhr1 observed in states Post-A1, Dis-A and Dis-B is in the loop-bound conformation. (**A-C**) Analysis of Dhr1 in the yeast SSU processome state post-A1. (**A**) Original model (yellow) and map (transparent) as well as difference density (map vs model; dark red) are shown. (**B**) Dhr1 core structure (this study) docked in the yeast SSU processome state post-A1. (**C**) Dhr1 core structure (this study) shown with difference density from panel A. (**D-F**) Analysis of Dhr1 in the yeast SSU processome state DIS-A. (**D**) Original model (yellow) and map (transparent) as well as difference density (map vs model; dark red) are shown. (**E**) Dhr1 core structure (this study) docked in the yeast SSU processome state DIS-A. (**F**) Dhr1 core structure (this study) shown with difference density from panel D. (**G-I**) Analysis of Dhr1 in the yeast SSU processome state DIS-B. (**G**) Original model (yellow) and map (transparent) as well as difference density (map vs model; dark red) are shown. (**H**) Dhr1 core structure (this study) docked in the yeast SSU processome state DIS-B. (**I**) Dhr1 core structure (this study) shown with difference density from panel G.

In addition to visualizing the auto-inhibited state in context, these structures also revealed how Dhr1 associates with the pre-40S. In the Pre-A1, Dis-A, and Dis-B structures, the Dhr1 helicase core is anchored to the pre-SSU via interactions between its RecA2 and Ratchet domains and Pno1 residues 67-84. This segment of Pno1 is nestled between the Dhr1 core and Utp13. The Dhr1 CTD interacts with Utp21, Utp1, Utp13, and Utp12 (**Fig 3.8A**). Additionally, portions of the N-terminal extension of Dhr1 are visualized. They bind more centrally in the particle, interacting with the methylase Dim1, the GTPase Bms1, and the 5' and central domains of the 18S (**Fig 3.8B**). This region of the pre-40S undergoes little change over the course of the Post-A1 to Dis-C structures.

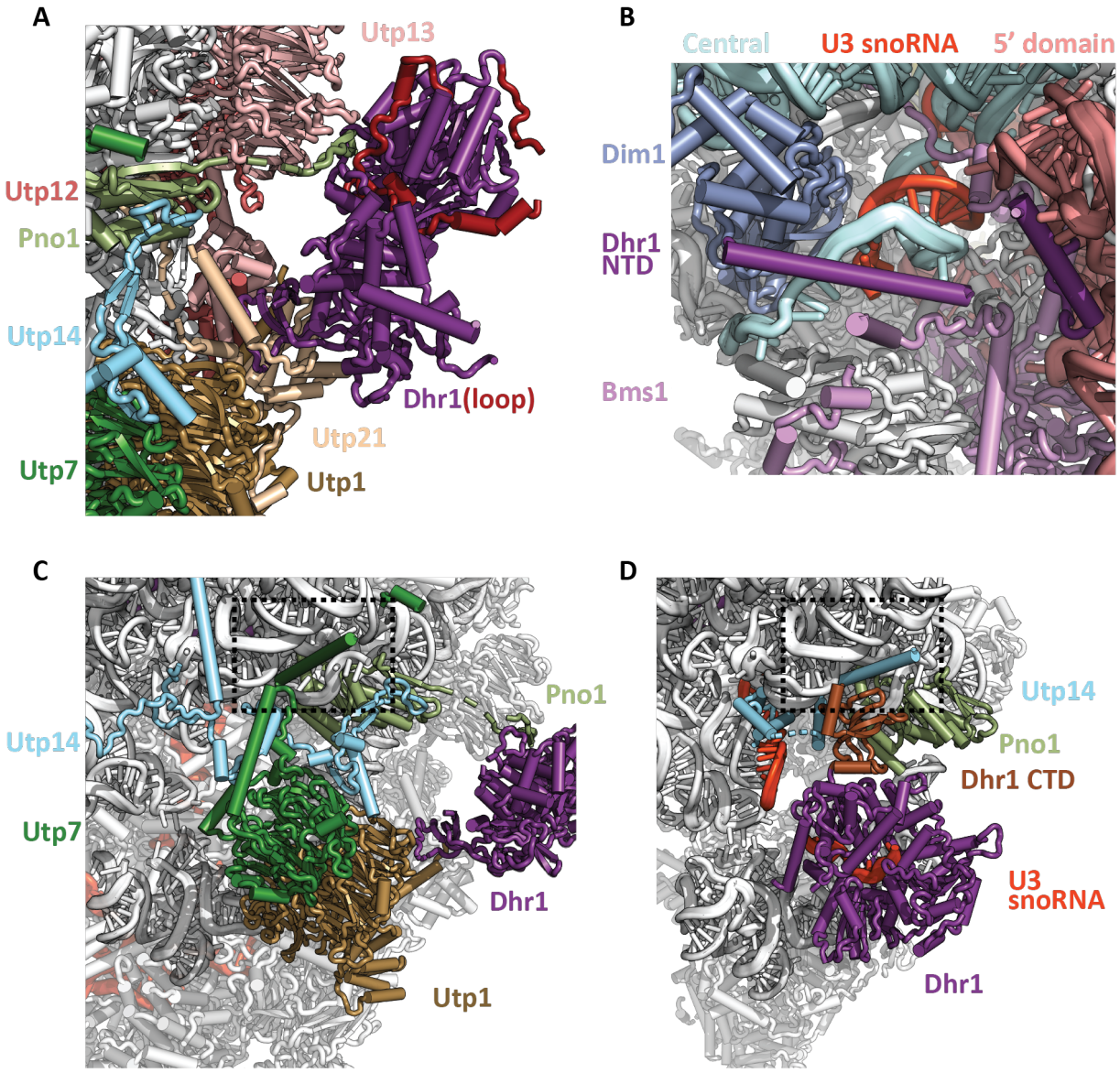

Figure 3.8 Dhr1 and Utp14 binding sites in the maturing SSU processome. A) Auto-inhibited Dhr1 interfaces with Utp13, Utp12, Utp1, and Pno1 in the Post-A1 state. PDB 6ZQD, auto-inhibited Dhr1 from this work. **B)** The Dhr1 NTD contacts several proteins and portions of the pre-18S closer to the core of the maturing SSU processomes. This image is from state Post-A1, but the area is very similar in all states. PDB 6ZQD **C)** The Utp14 binding site in state Post-A1. PDB 6ZQD **D**) Dhr1 shifts to its substrate U3 snoRNA in state Dis-C, its CTD interacts with Utp14 and the pre-18S. PDB 6ZQG. **C and D**) Black outlined box highlights the binding pocket first occupied by Utp7 (**C**) where Utp14 later binds to recruit Dhr1 to its substrate U3 (**D**).

In the final structure, “Dis-C”, Dhr1 makes a large movement from its “docked-away” conformation, and this change in binding site is regulated by the dissociation of proximal assembly factors. First, Utp7 dissociates from the pre-SSU during the transition from the Dis-A to Dis-B state. Then, Utp1, Utp21, and Utp13 dissociate in the transition from Dis-B to Dis-C, disengaging the helicase core and CTD from the “docked away” binding site. The Dhr1 CTD is now the major anchor point for the Dhr1 helicase core association with the pre-SSU in this region, where it interfaces with residues 370-421 of Utp14 near the U3 snoRNA. The binding site of Upt14 residues that serve as the platform for the Dhr1 CTD was previously blocked by Utp7 binding (**Fig 3.8C,D**).

In addition to illustrating the regulation of Dhr1 location by dissociation of early-SSU assembly factors, these structures also rationalize previous genetic data that identified the Dhr1 CTD as essential for viability and for recruitment of Dhr1 to the SSU processome, as the helicase core of Dhr1 is brought into proximity of the U3 snoRNA by the CTDs interactions with Utp14 and the 18S rRNA (Boneberg et al., 2019; Roychowdhury et al., 2019; **Fig 3.8D**). Although the Dhr1 NTD is making contacts in another region of the particle, this is far removed from the site where the Dhr1 core engages with the U3 snoRNA, and therefore sufficient interaction with the substrate U3 is likely impossible without the CTD.

There is also a wealth of information in these structures regarding the regulation of Utp14, the co-activator of Dhr1. In the Post-A1 state, the region of Utp14 of particular interest is residues 747 to 779, a region defined as necessary for stimulating RNA-dependent ATPase activity of Dhr1 (Boneberg et al., 2019; discussed in greater detail in section 3.2). In state Post-A1, these residues bind to Pno1 and in the proximity of Utp7 and Utp1 (**Fig 3.9B**). This allows us to re-analyze state Pre-A1 with fresh insight. In state Pre-A1, the region between Utp1 and Utp7 is occupied by a single stranded region of the 5’ETS. A double stranded region of the 5’ETS further blocks the Post-A1 conformation of Utp14 by interacting with the C-terminal extension of Utp7. Exosome-mediated rearrangement of the 5’ETS allows Utp14 to bind near Utp1 and Utp7, and in the proximity of Pno1 and the 18S, priming it for later recruitment of Dhr1 (**Fig 3.9**). After state Post-A1, Utp7 exits the particle, releasing the activating peptide, which is then disordered in all the remaining states (**Fig 3.6**). This should allow the activating peptide access to Dhr1 once it associates with the U3 snoRNA and begins unwinding, although this interaction is not observed in state Dis-C.

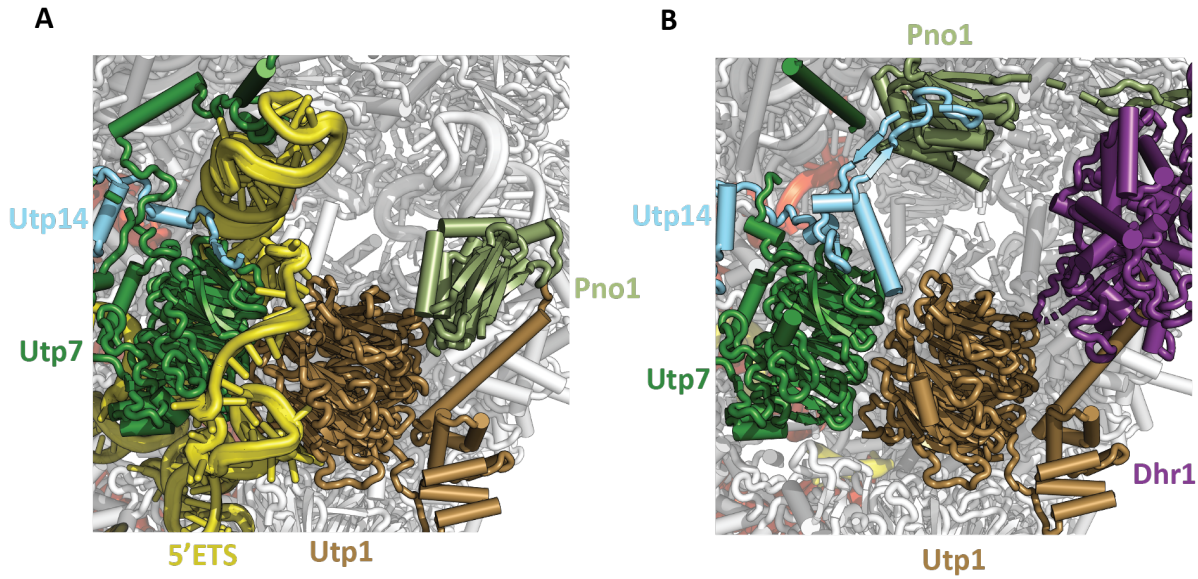

Figure 3.9 The binding site for Utp14 is occupied by the 5'ETS before the action of the exosome. A) The Pre-A1 state, where the 5'ETS occupies the site between Utp7 and Utp1. **B)** The Post-A1 state where the 5'ETS has been partially disordered after the activity of the exosome. The Utp14 segment that activates the ATPase activity can now bind in the proximity of Utp7 and Utp1.

This series of structures strengthens the understanding of how Dhr1 and Utp14 are regulated within the context of the maturing small subunit, but not how Utp14 works to increase Dhr1 activity as observed by *in vitro* biochemistry. So, despite the wealth of information about the progression of assembly past the SSU processome provided by Cheng et al., the central question of the mechanism of Dhr1 activation by Utp14 remains elusive.

3.2 Biochemical studies of Utp14 activation of Dhr1

To understand Utp14 activation of Dhr1, we sought to identify the minimum region of Utp14 responsible for Utp14 activation for use in biochemical and structural assays**.** Biochemical assays can provide us with a more fine-grained understanding of what aspects of Dhr1 activity are affected by Utp14. We can also use these assays to understand the contribution of the Dhr1 CTD to activity/ activation by Utp14, as the importance of the CTD has been demonstrated but is not mechanistically clear.

3.2.1 Identification of the minimal fragment of Utp14 necessary for Dhr1 activation

As discussed in Chapter 1.3, Boneberg et al. performed studies on *M. musculus* homolog of Dhr1 (DHX37) and Utp14. In addition to their structural studies of DHX37, they worked towards identifying a more minimal fragment of *M. musculus* Utp14 necessary to interact with DHX37 and activate DHX37 RNA-dependent ATPase activity. They identified a fragment containing Utp14 residues 555-619, which correspond to residues 747 to 779 in yeast Utp14 (Boneberg et al., 2019). Closer examination of several Utp14 homologs revealed that this segment of Utp14 contains several highly-conserved segments (**Fig 3.10A**). Secondary structure prediction identifies alpha helices for residues 750 to 759 and 764 to 778 with high confidence

(**3.10C**). Based on these predictions and sequence conservation, we expanded our range of interest to residues 747 to 827 and then subdivided this region into three segments: Utp14D (resi 747 to 780), Utp14E (resi 779 to 796) and Utp14F (resi 797 to 827) (**Fig 3.10B-D)**. These segments were cloned as N-terminal His14-SUMO fusions, and overexpressed and purified from *E. coli*. Additionally, to attempt to recapitulate an intermolecular reaction between Utp14 and Dhr1, a series of Utp14 and Dhr1 fusions were also expressed and purified (**Table 3.1**).

Table 3.1 Nomenclature used for Dhr1 and Utp14 constructs

Shorthand	Description	Residue Information
Dhr1core	Dhr1 helicase core (ΔNTDDhr1ΔCTD)	$Dhr1_{379-1185}$
Dhr1CTD	ΔNTDDhr1	$Dhr1_{379-1267}$
Utp14DEF	Utp14 DEF peptide	$Utp14_{747-827}$
Utp14D	Utp14 D peptide	$Utp14_{747-780}$
Utp14E	Utp14 E peptide	$Utp14_{779-796}$
Utp14F	Utp14 F peptide	$Utp14_{797-827}$
Utp14DE	Utp14 DE peptide	$Utp14_{747-796}$
Utp14EF	Utp14 EF peptide	$Utp14_{779-827}$
Dhr1CTD_Utp14D	C-terminal fusion of Dhr1CTD and Utp14D	$Dhr1_{379-1267}$-linker-$Utp14_{747-780}$
Dhr1CTD_Utp14DE	C-terminal fusion of Dhr1CTD and Utp14DE	$Dhr1_{379-1267}$-linker-$Utp14_{747-796}$
Dhr1CTD_Utp14DEF	C-terminal fusion of Dhr1CTD and Utp14DEF	$Dhr1_{379-1267}$-linker-$Utp14_{747-827}$
Dhr1CTD_Utp14EF	C-terminal fusion of Dhr1CTD and Utp14EF	$Dhr1_{379-1267}$-linker-$Utp14_{779-827}$

The first biochemical tool utilized to assess the effect of Utp14 fragments on Dhr1 activity was an RNA strand displacement assay. Here, a double stranded RNA substrate was generated where the longer strand is unlabeled, and the shorter strand is labelled with AlexaFluor487. This creates a substrate with both a 5' and 3' overhang and a 15 basepair double stranded region. In these assays, it was necessary to utilize a great excess of enzyme over RNA substrate, preventing proper Michealis-Menten kinetic analysis. Still, the relative effects of Utp14 on Dhr1 strand displacement activity could be assessed. This assay in isolation cannot identify exactly which aspect of helicase activity Utp14 engages. An increase in substrate recruitment, substrate loading, ATPase coupled substrate processing, or processivity are all aspects of Dhr1 activity that could be effected by Utp14 and observed as an increase in strand displacement in this assay.

These assays revealed that Utp14D was the fragment necessary for activation of strand displacement activity. Utp14E did not appear to have any effect on activity. Utp14F also did not affect activity, but shifted dsRNA bands in gels, indicating it may have an RNA binding ability (**Fig 3.10E**). The highest levels of activation caused by Utp14DEF, we hypothesize, are caused by the combination of the activation by Utp14D and substrate recruitment via the RNA binding ability of Utp14F (**Fig 3.10E**).

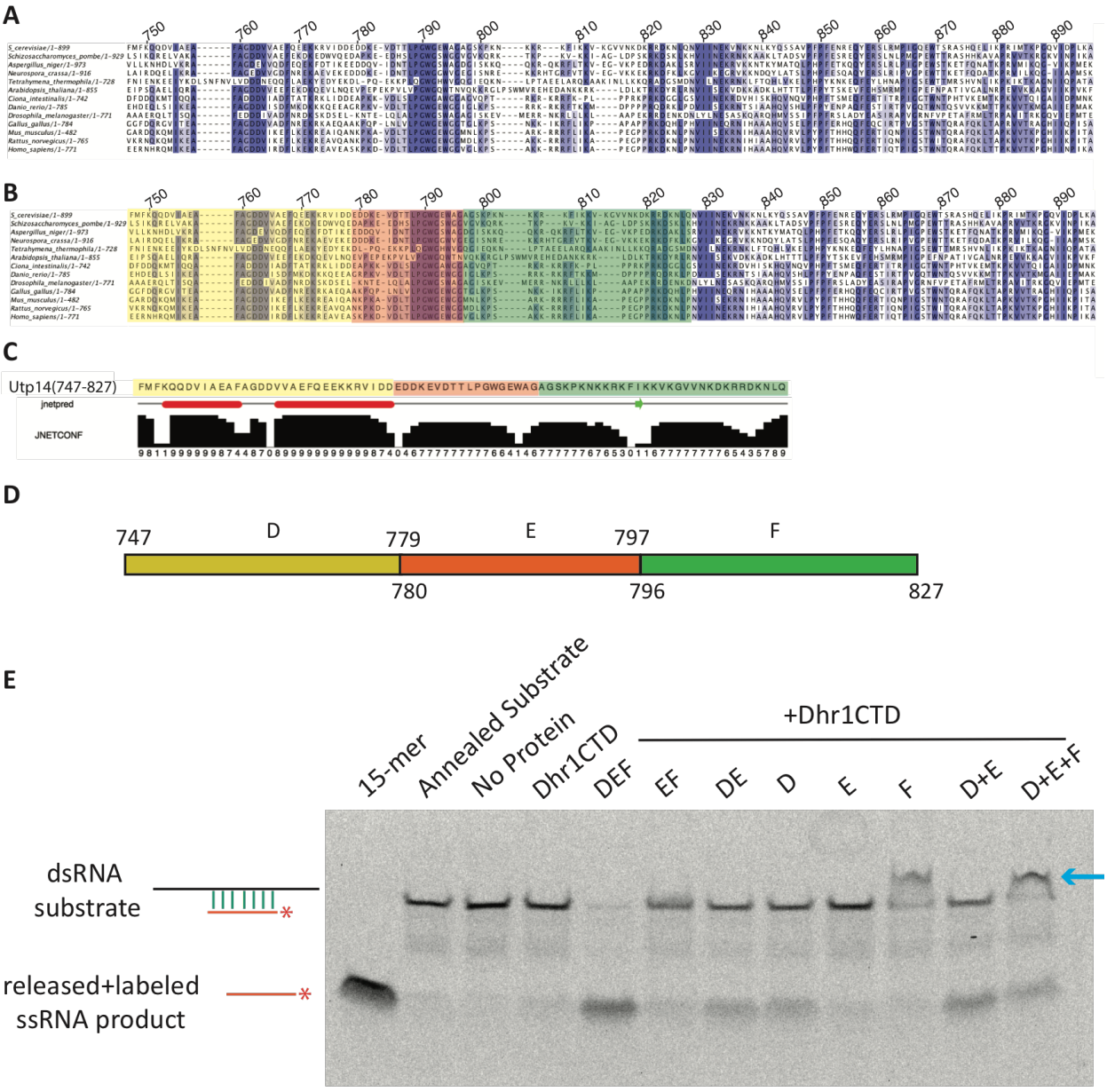

Figure 3.10 Identification of a more minimal segment of Utp14 responsible for Dhr1 activation. A) Sequence alignment for Utp14 C-terminal region. **B**) Alignment from A, highlighting the sub-regions that will be studied. **C**) Secondary structure prediction for Utp14 residues 747-827. **D**) Nomenclature for sub-regions of Utp14 constructs being studied. E) Representative image of a strand displacement assay 30 minute time point, utilizing Dhr1CTD in the presence of equimolar Utp14 segments. Blue arrow indicates super shifted dsRNA in reactions containing Utp14F.

The fusions of Utp14 and Dhr1 follow the same trends. Dhr1CTD_Utp14DEF is the most activated construct (**Fig 3.11A**). Dhr1CTD_Utp14DE and Dhr1CTD_Utp14D are nearly identical in activity, further indicating segment E does not contribute to activation. Dhr1CTD_Utp14EF exhibits slightly greater activity than Dhr1CTD on its own, which we hypothesize is due to substrate recruitment via segment F (**Fig 3.11A**). The difference in strand displacement activity observed between Dhr1CTD and Utp14DEF in trans versus the fusion of Dhr1CTD_Utp14DEF is also intriguing. In the reaction setup for these strand displacement assays, the concentration of Dhr1 and Utp14 constructs is equimolar, and relatively high at 8 µMolar. Still, a direct fusion of Utp14 and Dhr1 is necessary for near complete consumption of the substrate to be observed in our assay conditions (**Fig 3.11A**). Here, the fusion construct serves as a proxy for the essentially intramolecular reaction conditions forced by the architecture of the SSU processome, where Dhr1 helicase core is brought in proximity to U3 snoRNA and Utp14 in state Dis-C (**Fig 3.8D**).

The strand displacement assay also provided insights into the role of the Dhr1 CTD in activity. Dhr1CTD exhibits low levels of activity, displacing only about 20% single stranded RNA over the course of 60 minutes. But, the Dhr1 helicase core (both the NTD and CTD truncated) in isolation exhibits almost no activity (**Fig 3.11B**). Still, the Dhr1 core can be activated by Utp14, showing that the CTD is not strictly necessary for Dhr1 strand displacement activity or for activation by Utp14D (**Fig 3.11B**). The Dhr1 CTD can bind RNA, as seen in state Dis-C of the SSU processome where the CTD interacts with Utp14 and the backbone of the pre-18S **(Fig 3.8D).** It may be that the more productive strand displacement by CTD containing Dhr1 constructs may be due to increased RNA substrate recruitment. Although a direct comparison to the most recent studies on yeast and murine Dhr1 cannot be made as these studies only utilized ATPase assays to assess Dhr1 activity, it is interesting that these studies found that ΔCTD constructs had almost the same level of RNA-dependent ATPase activity as full length constructs (Roychowdhury et al., 2019; Boneberg et al., 2019). Since these are measure of RNA-dependent ATPase activity, it is intriguing that the CTD had no effect on ATPase activity. Perhaps the substrate U_{10} RNA utilized in the ATPase assays was too short to bind to be recruited by the CTD and still access the RNA substrate pocket. Whereas the RNA substrate used in our strand displacement assay is much longer, at 45 bases on the longer strand, and may be able to be efficiently recruited to the RNA binding site of the core via binding to the CTD. Further study will be necessary to understand the role of the CTD in activity, and future biochemical studies are discussed in Chapter 5.3.2.

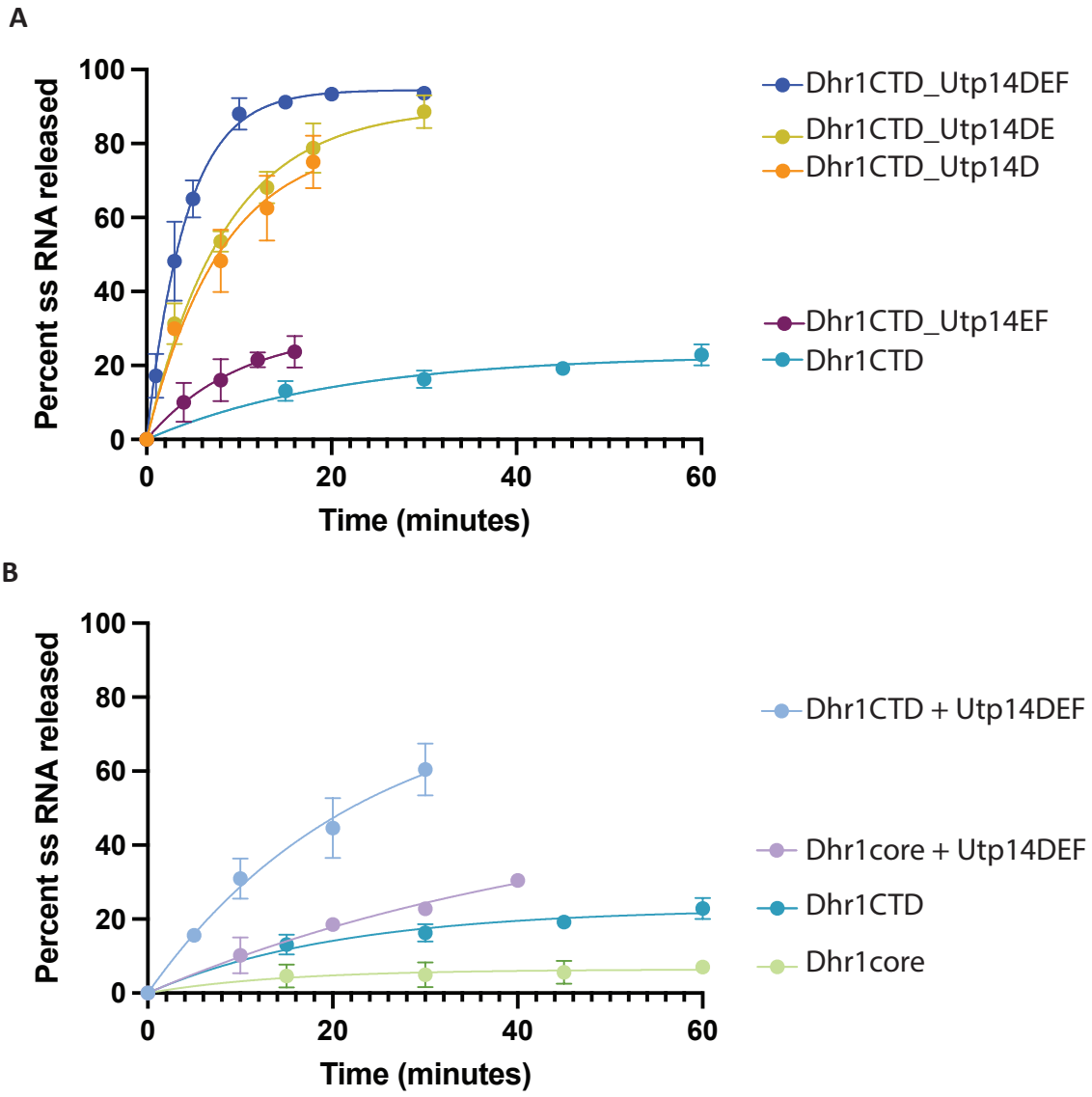

Figure 3.11 Strand displacement assays reveal the minimal segment of Utp14 for activation. Quantification of single strand displacement assays over the indicated time. **A**) Assays using fusions of Dhr1CTD (ΔNTDDhr1) and Utp14. **B**) Assays utilizing Dhr1 and Utp14DEF in trans. n=4, error bars represent calculated standard deviations.

3.2.2 Utp14 activating segment visualized in context of small subunit intermediates

Re-examination of the "Post-A1" state from Cheng et al. provided further insight into the regulation of Utp14 in light of our strand displacement assay data. Close inspection of the electron density in the proximity of Utp14, Utp1, and Utp7 revealed several more residues of Utp14 could be built, that weave between Utp1 and Utp7. These residues are the N-terminal region of Utp14D, so we now see that Utp14D is sequestered between Utp1 and Utp7 (**Fig 3.12**). This adds another aspect of control exhibited by Utp7: not only does the exit of Utp7 allow Dhr1 movement and the binding of the Dhr1-recruitment module of Utp14, it also controls the release of the activating segment Utp14D (**Fig 3.12**). Utp14E and F form a beta-hairpin with one strand in each segment, and interact with Pno1 in the area of residues 110-145. Utp14F may also help stabilize the location of Utp14D near Utp7 (**Fig 3.12**). Again, in the "Dis-C" structure where Dhr1 is bound to RNA and in close proximity to the U3 snoRNA, the segments Utp14DEF are not visualized, so no conclusions about their role can be made in the context of this structure (Section 3.1.4).

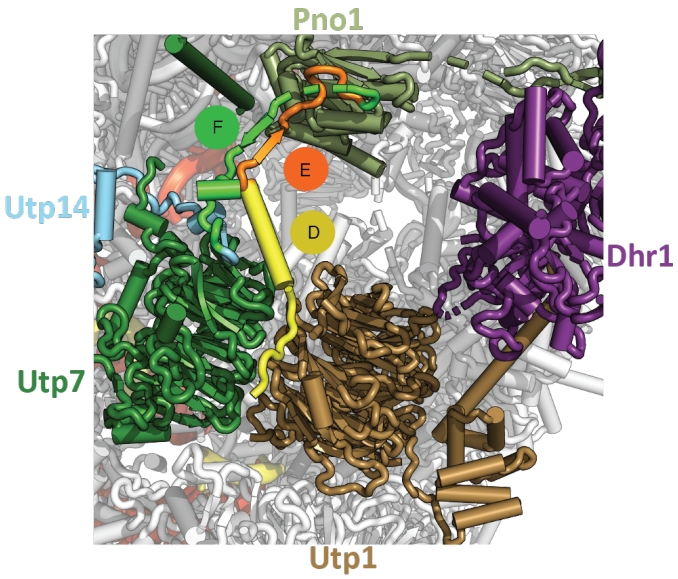

Figure 3.12 The activating segment of Utp14 is sequestered between Utp7 and Utp1. The same view as in **Fig 3.7C** from state Post-A1 is presented, now with the additional segment of Utp14 built between Utp7 and Utp1 based on EMD-11360 map. Segments Utp14D (yellow), E (orange), and F (light green) are highlighted.

3.2.3 Dhr1 and Utp14 observed in human small subunit assembly intermediates

In our lab, Sameer Singh pioneered study of small subunit assembly in human cells. After a recent breakthrough in sample preparation and data collection, Sameer Singh and Arnaud Vanden Broeck have solved the cryo-EM reconstructions of the human pre-40S before and after A1 cleavage. Comparison of the Post-A1 structures to the corresponding structure in yeast (Cheng et al., 2020) reveals a high level of conservation in the core architectures of these particles. These structures revealed that several of the mechanisms of Utp14 and Dhr1

regulation in yeast (to the extent we understand them currently) were largely conserved in humans (Singh et al., in review).

In the pre-A1 state, the pocket between Utp1 and Utp7 is occupied by the 5'ETS (**Fig 3.13A**). In the Post-A1 state, the action of the exosome has remodeled the 5' ETS and the binding site between Utp7 and Utp14 can now be occupied by Utp14D (**Fig 3.13B,C**). Additionally, the binding of the Utp14E and F segments is largely identical to that in yeast in the post-A1 state. Utp14E and F form a beta hairpin, with one strand from each segment, and the Utp14 segments are anchored to this region of the particle by binding to Pno1 (**Fig 3.13C**). Two highly conserved aromatic residues from segment Utp14EF are visualized in the proximity of the first base of the pre-18S (**Fig 3.13D**). Although the residues are from both Utp14E and F, only Utp14F interacts with RNA in our assays (**Fig 3.10E**). Residue Phe649 from Utp14F base stacks with pre-18S residue 1872, while residue Trp631 from Utp14E is not observed base stacking in the Post-A1 maps, but is at a distance from the 18S base where it may be able to (**Fig 3.13D**). Although they do not contribute to strand displacement activity in our assays, regions E and F may be highly conserved, at least in part, because of their contributions to the overall architecture of the assembly factors in this region of the pre-A1 state.

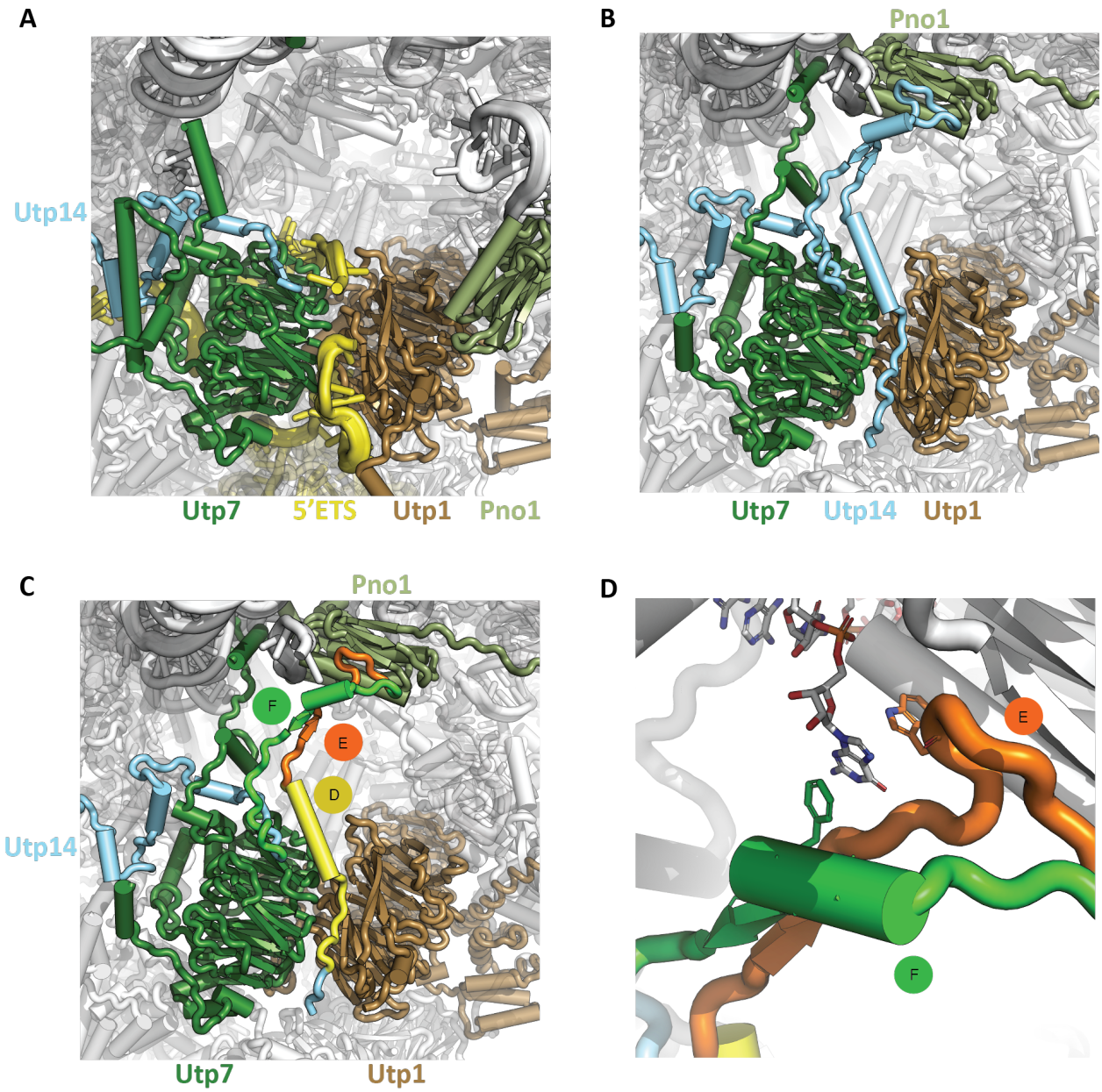

Figure 3.13 Regulation of Utp14 binding in maturing SSU processomes is conserved from yeast to humans. **A**) In the human SSU processome Pre-A1 state, the binding site between Utp7 and Utp1 is occupied by the 5' ETS. **B**) In the Post-A1 state, Utp14 now occupies the site between Utp7 and Utp1. **C**) This segment of Utp14 is homologous to the Utp14DEF segments identified in this work from yeast. **D**) Conserved residue Utp14F (Phe649) base stacks with 18S residue 1, while conserved residue Utp14E (Trp631) is not observed base stacking in the Post-A1 maps, but is at a distance from the 18S base where it may be able to.
Yeast nomenclature is used to label human homologs for simplicity. Regions of Utp14 upstream of segment D have been removed from these views for clarity.

The regulation of Dhr1 activity also appears well conserved. In the Post-A1 human structure, it is once again clear that Dhr1 is being held away from its U3 substrate, where the helicase core is bound on the periphery of the particles (**Fig 3.14A**). The helicase core does not appear to make direct contacts with the pre-SSU itself, rather it is tethered to the particle via its C-terminal and N-terminal extensions (**Fig 3.14A,B**). As discussed in Chapter 1.3, the NTD of Dhr1 is not well conserved from yeast to human, but the general path of the NTD is similar. The NTD still contacts Dim1, and the central and 5' domains of the pre-18S, while a human specific interaction is formed between DHX37 and the ribosomal protein S6 (**Fig 3.14B**). The DHX37 CTD interacts with Utp21 and Utp1 (**Fig 3.14A**). As in yeast, it is again clear that this "docked-away" DHX37 is in the auto-inhibited conformation, a conserved layer of control of Dhr1 activity. Although the density was not very high resolution in this region, the overall conformation of the auto-inhibited Dhr1 core fits best in the DHX37 density. The model for the core was built first based on the more closely related murine structure of DHX37, and then arranged in a conformation like the auto-inhibited Dhr1 core. This resulted in the best fit for the density (**Fig 3.14C-F**).

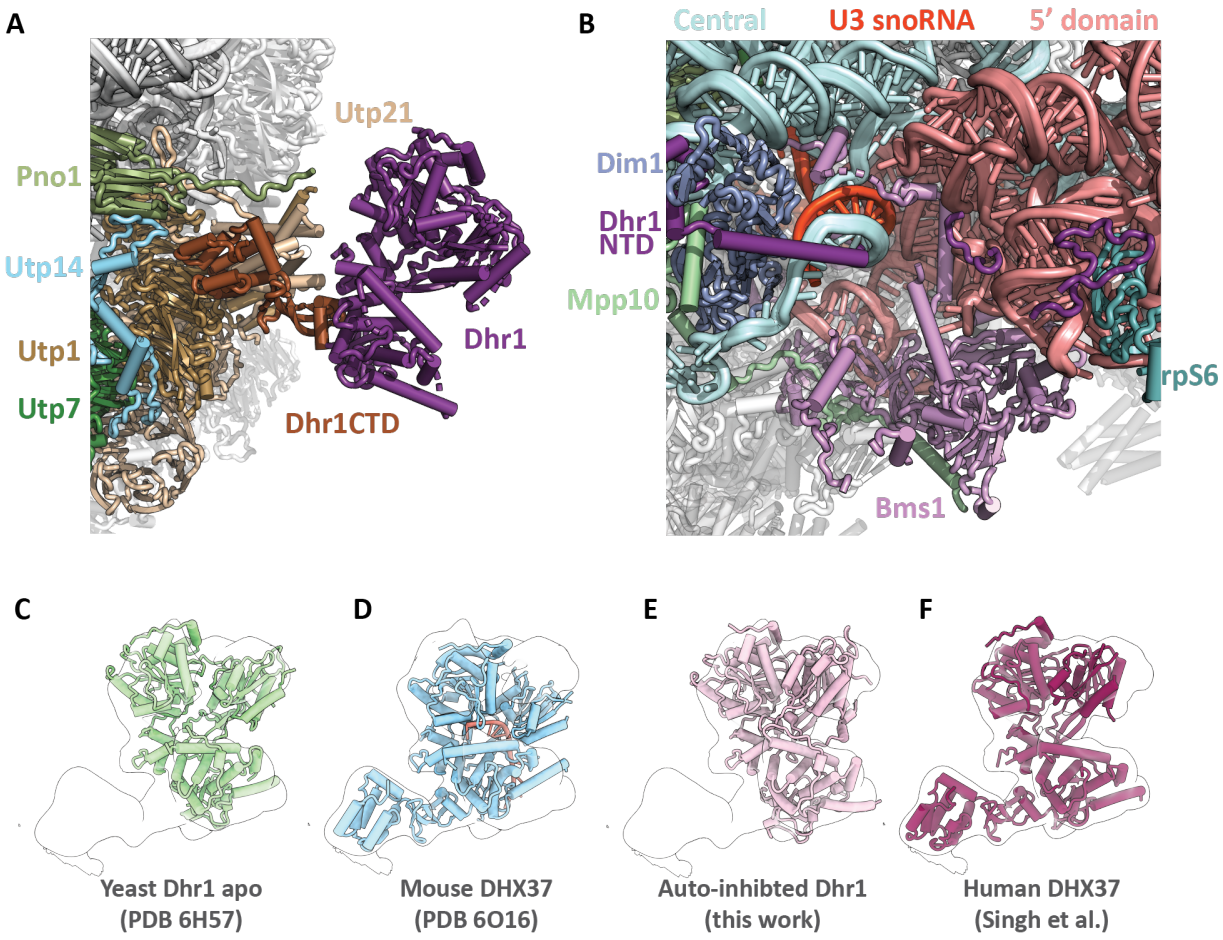

Figure 3.14 Several key Dhr1 interactions are conserved in human maturing SSU processomes. **A**) Dhr1s binding site in the Post-A1 state. **B**) Dhr1 NTD binding site in the Post-A1 state. (**C-F**) Fitting of Dhr1 structures into the human SSU processome post-A1 state electron density with yeast apo Dhr1 core (PDB 6H57, **C**), RNA-bound mouse DHX37 (PDB 6O16, **D**), auto-inhibited Dhr1 core (this study, **E**) and human DHX37 (Singh et al., **F**). (**A and B**) Yeast nomenclature is used to label human homologs for simplicity.

3.2.4 Co-crystallization of Dhr1 and Utp14 yields a more complete structure of auto-inhibited Dhr1, but not Utp14

There were several attempts at co-crystallization of Dhr1 and Utp14, in an attempt to gain structural insight into the effect of Utp14D on Dhr1 helicase core conformation. Crystallization trials utilizing either the fusion construct Dhr1CTD_Utp14D or Dhr1 co-crystalized with Utp14D peptide only revealed density for the Dhr1 helicase core and the CTD in the same, overall loop bound structure observed for the crystal structure of the Dhr1 core. Several crystallization conditions yielded essentially identical structures in one of two unit cells. The best resolution resulted from the crystallization of the fusion Dhr1CTD_Utp14D and this was used to build and refine the Dhr1CTD structure at a 2.4 Å resolution. The Dhr1CTD structure allowed us to visualize an auto-inhibited Dhr1 core in the absence of nucleotide and with the Dhr1 CTD (**Fig 3.15**). The helicase core is in a nearly identical conformation to our previously determined Dhr1 core structure, even in the absence of ADP. Meanwhile, the CTD is in largely the same conformation as observed by Roychowdhury et al.'s structure of Dhr1 (Roychowdhury et al., 2019). As the Dhr1CTD_Utp14D crystals were formed in conditions unique from the Dhr1core crystals, and also exhibited different crystal packing, we hypothesize the open conformation of the helicase core is enforced by loop-binding, as the same conformation is observed in both the presence and absence of ADP. Therefore, we now have a more complete structure of the auto-inhibited Dhr1.

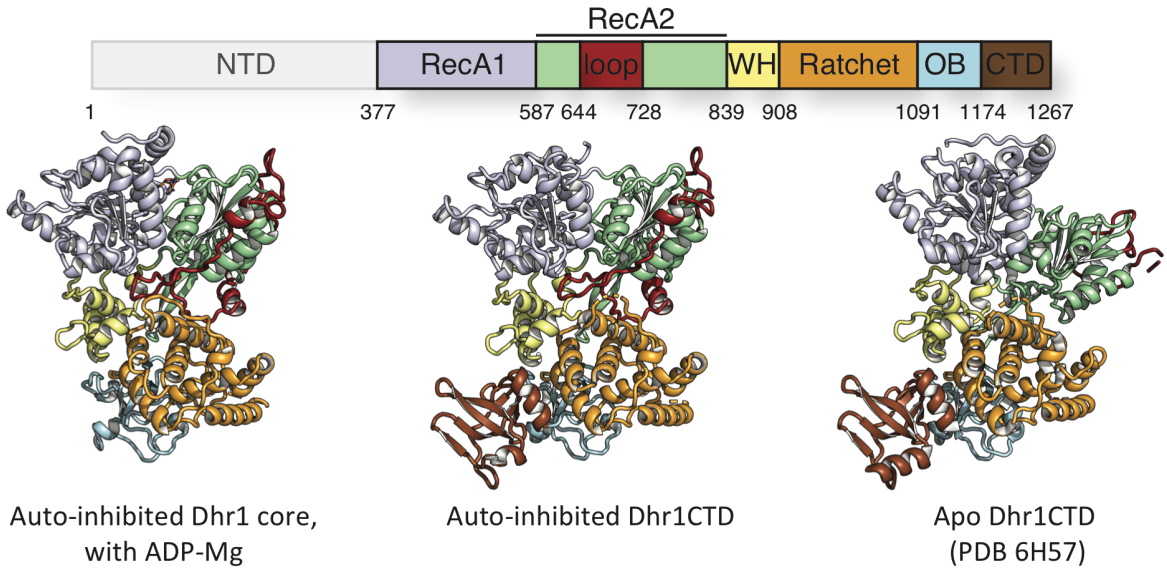

Figure 3.15 Structure of the more complete auto-inhibited Dhr1 helicase. Side by side comparisons of our auto-inhibited Dhr1 core with ADP, our more complete auto-inhibited Dhr1CTD, and the "apo" Dhr1 in the absence of nucleotide. Domain architecture of Dhr1 is displayed at the top of the figure, structures are colored accordingly.

3.3 Conclusions

Here, the Dhr1 specific loop was discovered and characterized structurally. This loop is within the RecA2 domain of the helicase core, and is present in all Dhr1 homologs, but not present in other members of the DEAH-box helicase family. Although non-essential, this feature of Dhr1 winds around the RecA2 domain of the helicase and occupies the substrate RNA tunnel. Our crystal structure of the Dhr1 helicase core bound to the loop allowed us to reinterpret published structures of maturing small subunit processomes from yeast, where Dhr1 that is docked away from its substrate U3 snoRNA is in a loop-bound conformation. We therefore refer to the loop-bound Dhr1 as the "auto-inhibited" state. Additionally, biochemical work towards understanding how Utp14 activates Dhr1 has set the foundation for identifying a more minimal segment of Utp14 required for activation and for the role of the CTD in activity. Again, we find a more minimal activating segment of Utp14, termed Utp14D, is also sequestered away from Dhr1 in a maturing small subunit structure where Dhr1 unwinding activity is not yet required. Additionally, utilizing fusions of Dhr1 and Utp14 in strand displacement assays served as a proxy for the close proximity of Utp14, Dhr1, and U3 snoRNA enforced in the maturing pre-ribosome structures, and highlighted how the coordination and proximity of these factors is necessary for efficient unwinding by Dhr1. Lastly, recent data from our lab characterizing maturing small subunit processomes isolated from human cells reveals that these regulations on Dhr1 activity and Utp14 binding are largely conserved from yeast to human.

Chapter 4:
Preliminary studies of the Urb subcomplex and Urb subcomplex-containing pre-60S particle

Our understanding of the nucleolar stages of assembly has greatly aided structural studies of 27SB rRNA containing pre-60S particles (Chapter 2). To understand even earlier stages of LSU assembly, we aimed to study assembly factors associated with an even earlier large subunit precursor- the 27SA rRNA. In particular, the "Urb subcomplex", composed of Urb1, Urb2, Dbp6, Nop8, and Rsa3, served as a specific target to begin studying the very early stages of assembly (see Chapter 1.3.2 for more information on the Urb subcomplex proteins). All of these proteins, except Rsa3, are essential for the very early maturation of the pre-60S in the nucleolus, but serve unclear functions. Of particular interest is Dbp6, a DEAD-box protein with an unknown RNA target. The 27SA containing pre-60S which also contains the Urb subcomplex is referred to as the "Urb particle" here.

This work was performed on my own, except for mass spectrometry analysis that was provided by members of the Proteomics Core at Rockefeller.

4.1 Purification of the Urb subcomplex

We aimed to isolate and study the composition of the Urb subcomplex in order to better understand the architectures and function of the essential members of this complex and contribute to the understanding of the very earliest stages of large subunit assembly. Urb1, Urb2, Rsa3, and Nop8 were endogenously tagged on their C-termini with affinity tags. It was observed that C-terminal tagging of Urb1 caused a slow growth defect, but tagging of Urb2, Nop8, and Rsa3 did not. Two step affinity purification of the Urb subcomplex was successful in purifying all five members of the Urb subcomplex, in good stoichiometry except for Dbp6, which was often substochiometric. This purification could be accomplished at low optical density when rates of ribosome biogenesis are high, and high optical densities, when rates of ribosome biogenesis are reduced. Higher purity of isolated Urb subcomplex and a reduction in background pre-ribosomes during purification could be encouraged using high salt, growing yeast at high optical densities, and utilizing two affinity capture steps.

Strikingly, two-step purification consistently co-purified the box C/D snoRNA machinery (Nop1, Nop56, Nop58, and Snu13), and purified particles had a high signal for nucleic acids, usually a 260/280 ratio of about 1.6-2.0 (**Fig 4.1A,** Table 7.5). Purification with RNAse/DNAse treatment during cell lysis and during the first affinity capture step still resulted in particles containing the Box C/D snoRNA machinery and high nucleic acid signal (**Fig 4.1A)** To assess the nucleic acid component of these particles, RNA isolation was performed on purified Urb subcomplex. Two bands were visualized on RNA gels, a major band at around 200 nucleotides and a less prominent band between 150 and 200 nucleotides (**Fig 4.1B**). This was highly suggestive that the Urb subcomplex associates with a specific box C/D snoRNA. This left several candidate snoRNAs of unknown function. Northern blotting using probes complementary to snr190 (190 nucleotides) and snr4 (186 nucleotides) only revealed signal for the snr190 probe (**Fig 4.1B**). The identity of the snoRNA was also confirmed by RNAseq, where RNA isolated from the purified subcomplexes was analyzed. It is intriguing that when snr190 was first identified, it was found to be non-essential for *S. cerevisiae* viability (Zagorski, Tollervey, & Fournier, 1988). Yet, our data indicate snr190 may be chaperoned by a set of essential assembly factors.

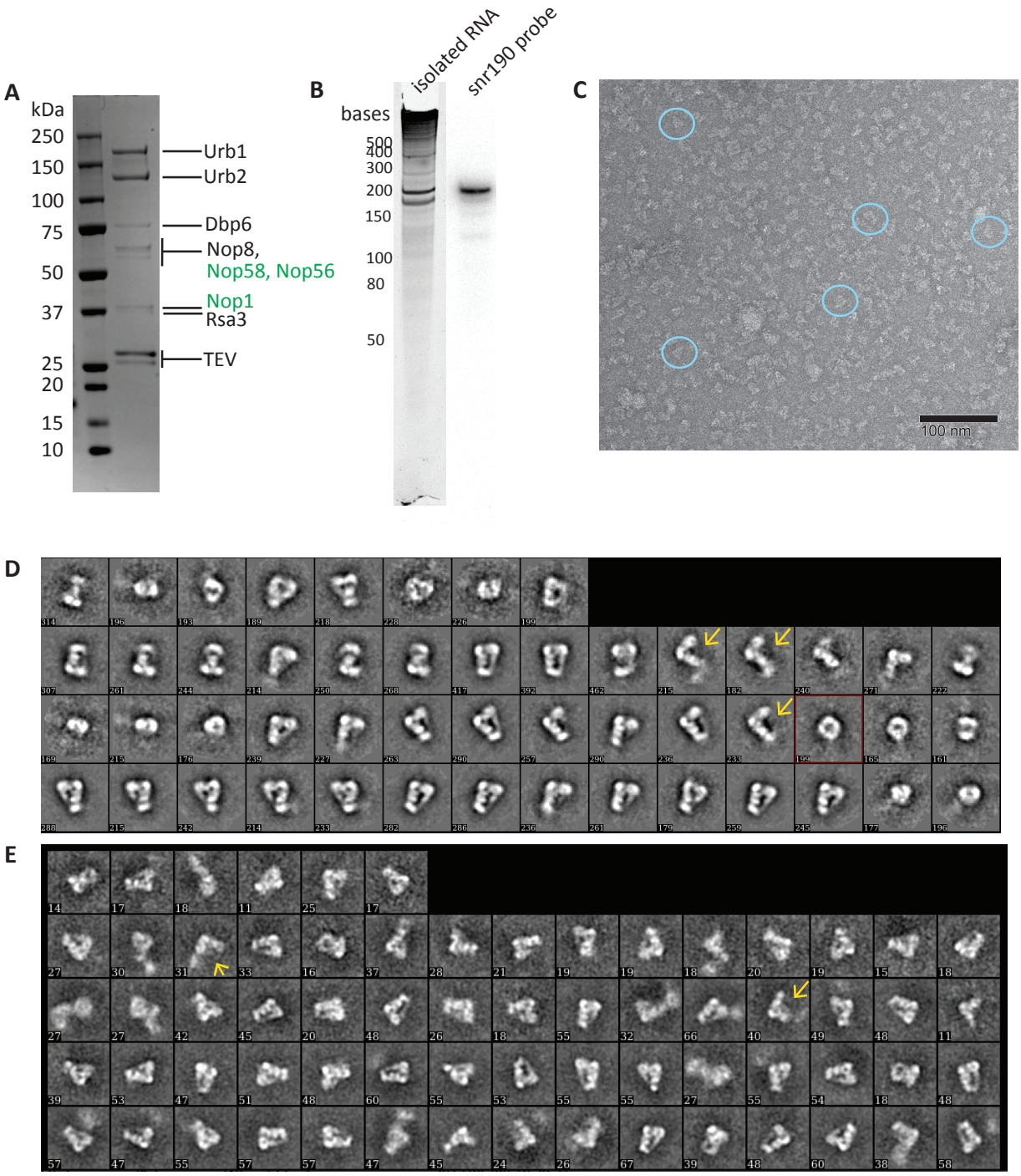

Figure 4.1 Preliminary work towards purification and structural characterization of the Urb subcomplex. A) Representative SDS-PAGE from Urb subcomplex purification. Green text is for proteins of the Box C/D snoRNA. **B**) RNA isolated from purified Urb subcomplexes (left), analyzed by Northern Blotting for snr190 (right). **C**) Negative stain micrograph of Urb subcomplexes, stained with rranyl acetate. **D,E**) 2D classes from negative stain datasets as produced by EMAN2 (**D**) or ISAC (**E**). Numbers in bottom right represent the number of particles in each class.

Our current understanding of the composition of the Urb subcomplex is in agreement with published data from the Henry lab (Joret et al., 2018). In this work, Joret and colleagues utilize a variety of biochemical and genetic methods to begin to assess the architecture of the Urb subcomplex and to identify RNA-protein crosslinking sites between Urb1 and the 25S rRNA and Urb1 and several snoRNAs. In agreement with our finding that the Urb subcomplex can still be purified during both low cell density (high rates of ribosome biogenesis) and high cell density (low rates of ribosome assembly), Joret et al. could isolate Urb subcomplexes when ribosome biogenesis was halted via depletion of a core Polymerase I component. Potential RNA binding sites for Urb1 were also identified using UV Cross-linking and Analysis of cDNAs (CRAC). One site was identified within domain I, another was identified at the junction of domain IV and V, while several sites were identified in domain VI. Pulldown studies from our lab by Malik Chaker-Margot that assessed the association of assembly factors with specific stages of 25S rRNA transcription found low signal for the Urb subcomplex only when domain V is first incorporated into the nascent transcript (Chaker-Margot & Klinge, 2019), so this may support the binding of the Urb subcomplex in the proximity of domains I, V, and VI. The Urb1 CRAC data also revealed potential interactions with several snoRNAs including snr190, in further agreement with our work. A new site of complementarity between snr190 and the 25S was postulated, where one basepairing site is within domain I and the other site is within domain V (Joret et al., 2018). Taken together, the Urb subcomplex and snr190 may interact with the pre-60S at the junction of domains I, V, and VI, but this will need to be verified with further biochemical and structural analysis.

4.1.1 Negative stain studies of the Urb subcomplex

The purity and stability of the Urb subcomplex was first analyzed using negative stain analysis. Micrographs revealed that a typical purification would yield a fairly high concentration of Urb subcomplexes that were fairly homogeneous in size with little aggregation. Negative stain images were analyzed using EMAN2 and stable 2D classes were identified both using EMAN2 2D classification and ISAC 2D classification (**Fig 4.1E,F**). These revealed an isosceles triangular shaped particle, but distinct features were hard to find from the limiting resolution provided by negative staining with uranyl acetate. It did appear that two “long sides” of the triangle may be flexible relative to each other, creating twisted conformations. Additionally, there may be some classes where one “side” is missing (**Fig 4.1 E, yellow arrows**).

Although there was evidence of conformational flexibility within the Urb subcomplex, the relatively high concentration, lack of aggregation, and ability to 2D classify in negative stain made it a promising candidate for cryo-EM trials. Trials utilized grids with open holes (C-flats) and carbon backing (Lacey Carbon grids). C-flat grids appeared empty, whereas the contrast in lacey carbon micrographs was often so poor that confident particle picking was not possible. With these issues, stable 2D classes could not be generated from a small dataset collected on Lacey Carbon grids.

4.1.2 Conclusions

Here, I was able to purify and characterize the components of the Urb subcomplex. It was revealed that the Urb subcomplex not only contains the previously categorized set of Urb1, Urb2, Nop8, and Dbp6, but also contains the box C/D snoRNA machinery (Nop1, Nop56, Nop58, Snu13) and the snoRNA snr190. Negative stain studies of the purified particles revealed a potentially promising target for high resolution structural work using cryo-EM. But, at this time, moving from negative stain to cryo-EM studies has been unsuccessful. The role of the subcomplex and of snr190 remains elusive. This would be best understood with a greater structural and biochemical understanding of the Urb subcomplex both in isolation and in the context of the large subunit intermediates.

4.2 Purification and composition of the Urb particle

In order to contribute to the overall understanding of the earliest stages of nucleolar assembly of the large subunit, we were interested in purification and structural studies of a 27SA rRNA containing pre-60S. In particular, the goal was to purify 27SA containing particles by way of the Urb subcomplex proteins, which are 27SA associated factors. In addition to providing an opportunity to understand some of the very earliest stages of LSU rRNA folding, this approach would also provide an opportunity to see a Box C/D snoRNA in context of a pre-ribosomal subunit. The previous section on the purification of the Urb subcomplex (Section 4.1) describes my work identifying that the Box C/D protein machinery and snr190 are components of the complete Urb subcomplex. At this time, only the U3 snoRNA has been visualized in the context of a pre-ribosome.

To purify intact 27SA particles containing the Urb complex proteins, Urb1, Urb2, Rsa3, and Nop8 were endogenously tagged on their C-termini with affinity tags. It was observed that C-terminal tagging of Urb1 caused a slow growth defect, and therefore was not utilized for the purification of Urb particles. Under exponential growth conditions, purification using two Urb subcomplex proteins as baits would always isolate Urb subcomplex (see section 4.1.1), but not full pre-60S particles. This was determined by the lack of other 27SA associated factors like Rrp5 and Mak21. Therefore, to ensure purification of pre-60S particles, the optimal scheme was to purify using one affinity handle on an Urb subcomplex component and one another non-subcomplex 27SA associated assembly factor. The most optimized strain for this purpose utilized affinity capture on Rrp5 and Rsa3. Rrp5 was used as first capture to avoid contamination with superstochiometric Urb subcomplex. This purification scheme produced particles that contained all the members of the Urb subcomplex along with several additional 27SA associated assembly factors like Mak21, Nop4, Cic1, and Erb1 which were visualized on SDS-PAGE and/or identified using mass spectrometry (**Fig 4.2A**, Appendix 7.5). The overall quality of the purified particles was assessed using negative stain, where it was clear that particles were aggregation prone, and heterogeneous in composition (**Fig 4.2B**). Stable 2D classes could not be generated from small negative stain data sets that were collected, although there were individual particles that appeared of interest (**Fig 4.2C**). Attempts at cryo-EM studies were performed using lacey carbon grids. Here, it was difficult to identify individual particles, and autopicking could not be used to reliably pick particles. Classification in 2D of the picked particles resulted in 2D classes lacking any features. Currently, this purification does not produce particles of high enough quality for study by cryo-EM. Considerations of why structural

studies of this particle have been unsuccessful despite promising mass spectrometry results are discussed in chapter 5.2.

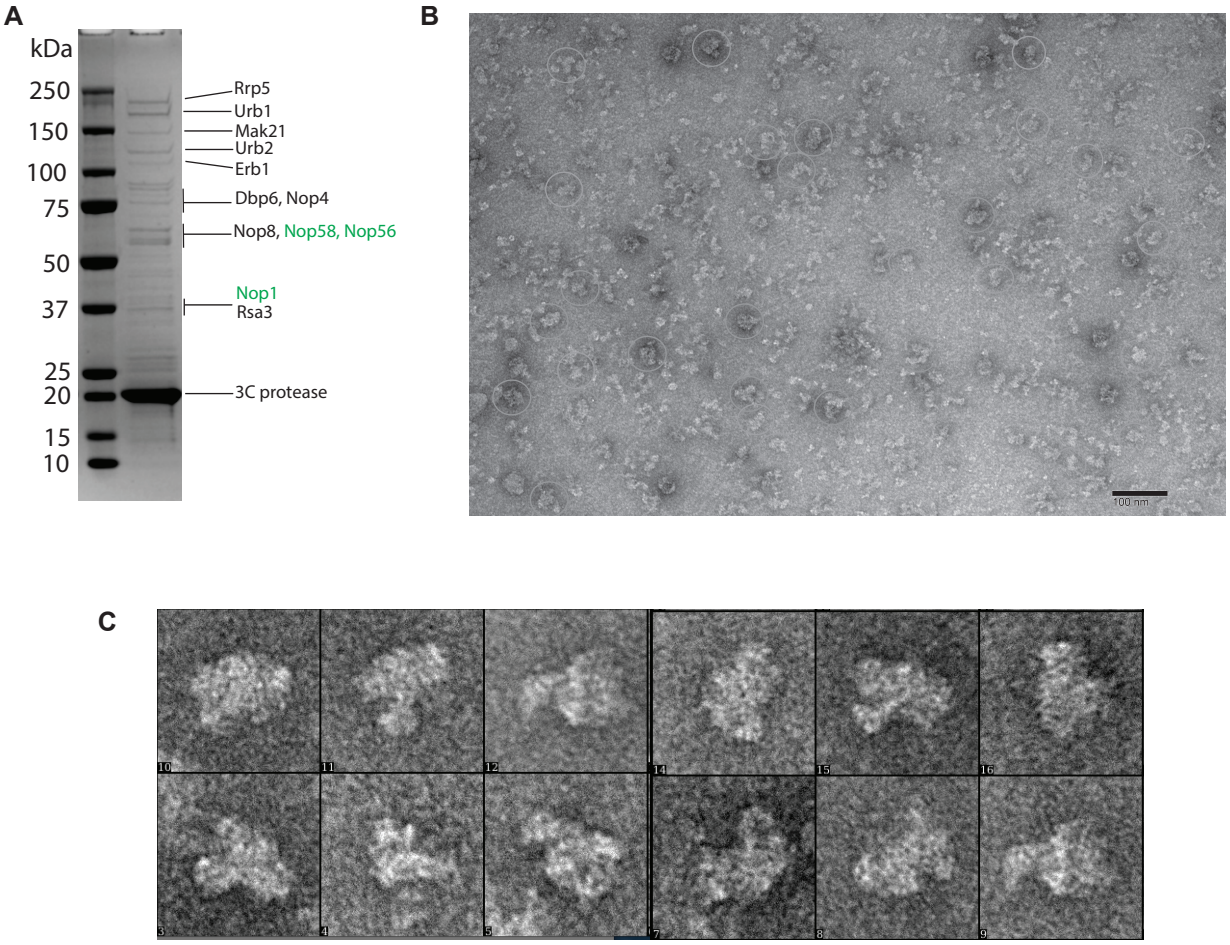

Figure 4.2 Preliminary work towards purification and structural characterization of the Urb particle. **A**) Representative SDS-PAGE from Urb particle purification, with certain assembly factors highlighted. Green text is for protein of the Box C/D snoRNA. **B**) Negative stain micrograph of Urb particles, stained with X% Uranyl acetate. **C**) Individual particles from negative stain images like (B).

4.2.1 Conclusions

Purification and structural studies of an Urb subcomplex and 27SA rRNA containing pre-60S particle could provide insight into the role of the Urb subcomplex in LSU assembly, provide another snapshot of a snoRNA in context of the pre-ribosome, and provide insight into the earliest stages of folding of the large subunit rRNA. So far, these structures have remained elusive. Still, this work has expanded our understanding of the composition of the Urb subcomplex, highlighting its association with the Box C/D snoRNA snr190.

Chapter 5: Discussion

5.1 The nucleolar pre-60S

5.1.1 Model of nucleolar pre-60S assembly

Before the start of this work, the Nog2 particle, a late nucleolar/early nucleolar pre-60S, was the earliest snapshot of large subunit biogenesis available (Wu et al., 2016). In these structures, a large proportion of the LSU rRNA was already folded in a near-mature conformation. The nascent active sites were strategically bound and protected by various assembly factors, and the particle was primed for processing by the exosome and the necessary next steps for becoming nuclear-export competent. These structures helped strengthen the observed trend, also seen in small subunit biogenesis, that the solvent exposed portion of the large subunit matures earlier in the assembly process, while the subunit interface and active centers of the LSU mature more gradually.

At the start of this work, many nucleolar assembly factors had not yet been structurally characterized in the context of pre-60S biogenesis, and their exact functions remained unknown. Our goal was to isolate and structurally characterize even earlier stages of large subunit assembly containing the 27SB rRNA, one of the earliest states of the pre-60S rRNA after transcription of the rDNA has been completed. Using these structures, we hoped to identify the roles of these factors and observe even earlier states of pre-rRNA folding.

Our work elucidated three unique states of the 27SB rRNA. We believe two of these, State 1 and state 2, are bona fide pre-60S intermediates. The last state, state 3, we believe may be a breakdown product of a later stage of assembly that was accumulated due to our purification conditions (the nature of state 3 is discussed in Chapter 5.1.2). The most striking feature of the early nucleolar pre-60S is the architecture of the rRNA. It was in line with the observed trend of pre-60S maturation to this point, but to the logical extreme. The base of the nucleolar pre-60S is formed by domains I, II, and the 5.8S rRNA, of which large portions of these domains are in a near-mature conformation (**Fig 2.6**). In contrast, domain IV, which interfaces with the small subunit, and domain V, which makes up the peptidyl transferase center and tRNA binding sites in the mature LSU, are almost completely disordered. Another key feature of the mature LSU is the polypeptide exit tunnel, through which nascent polypeptides exit the ribosome. Throughout assembly, there is great care taken by the cell to occupy the nascent polypeptide tunnel with an assembly factor until the very last stages of assembly (Chapter 1.2.2). In the nucleolar pre-60S, the nascent polypeptide tunnel has not been formed, and the solvent exposed side of the PET is partially formed in states 2 and 3 (**Fig 2.9**).

The observed flexibility of the domains III, IV, and V is in agreement with mass spectrometry studies which identified the assembly factors recruited by each domain of the pre-LSU rRNA (**Fig 1.9**). These studies found that transcription of domains I, II, and VI recruits many assembly factors, while the transcription of the intervening domains (III, IV, and V) recruits almost no factors. This could be partially rationalized by our structure, where domains IV and V are flexible and it is possible they are not bound to any assembly factors at this point. The recruitment of the 5S RNP (the 5S rRNA, Rpf2, Rrs1, rpL5 and rpL11) by domain VI is an interesting caveat. We know the 5S RNP is present in our purified nucleolar pre-60S via both mass spectrometry analysis and northern blotting analysis. But, it does not appear that the 5S is

tethered to the particle via domain VI. In later structures (Nog2 particle, Wu et al., 2016) the 5S is finally stably incorporated into the pre-60S, where the base of the 5S RNP binding site is formed by domain V. The lack of stable incorporation of the 5S over the course of the pre-nucleolar 60S observed by Kater et al. implies that the incorporation of the 5S necessitates almost complete initial folding of domain V (Kater et al., 2017). Looking to our crosslinking data of the purified nucleolar pre-60S, Rpf2 forms few crosslinks, mostly with itself and rpL5. Rrs1 forms a large number of crosslinks to Loc1, a nucleolar assembly factor that is also recruited by domain VI. The exact function of Loc1 remains elusive, and its structure has not yet been observed in any pre-60S structures at this time. Although the transcription of domain VI is necessary for recruitment of the 5S RNP, it is likely that it is associated with the flexible domain V during the early stages of assembly as domain V constitutes the binding site of the 5S RNP and the 5S RNP assembly factors do not crosslink to any domain VI associated factors. Overall, this implies that the folding of domains IV and V, and the recruitment of assembly factors by these domains, must occur after the "base" of the pre-60S is formed by domains I, II, and VI (**Fig 5.1**).

This is contrast to the current understanding of the very beginning of small subunit assembly (**Fig 1.6**). Here, each domain of the 18S recruits assembly factors, and each domain remains flexible until they finally coalesce into the SSU processome upon complete transcription of the pre-18S (Hunziker et al., 2019). Still, many of the assembly factors that are recruited co-transcriptionally exit the assembly process before the formation of the SSU processome. In small subunit assembly, the base of the particle is formed by the 5'ETS particle, which contains the UtpA, UtpB, 5' ETS, and U3 snoRNP. These subcomplexes form many contacts with the 18S domains, but the base of early SSU assembly is made of assembly factors and RNA that will not be part of the mature subunit. In large subunit biogenesis, the base for early LSU assembly is largely made up of the domains that will constitute mature 25S.

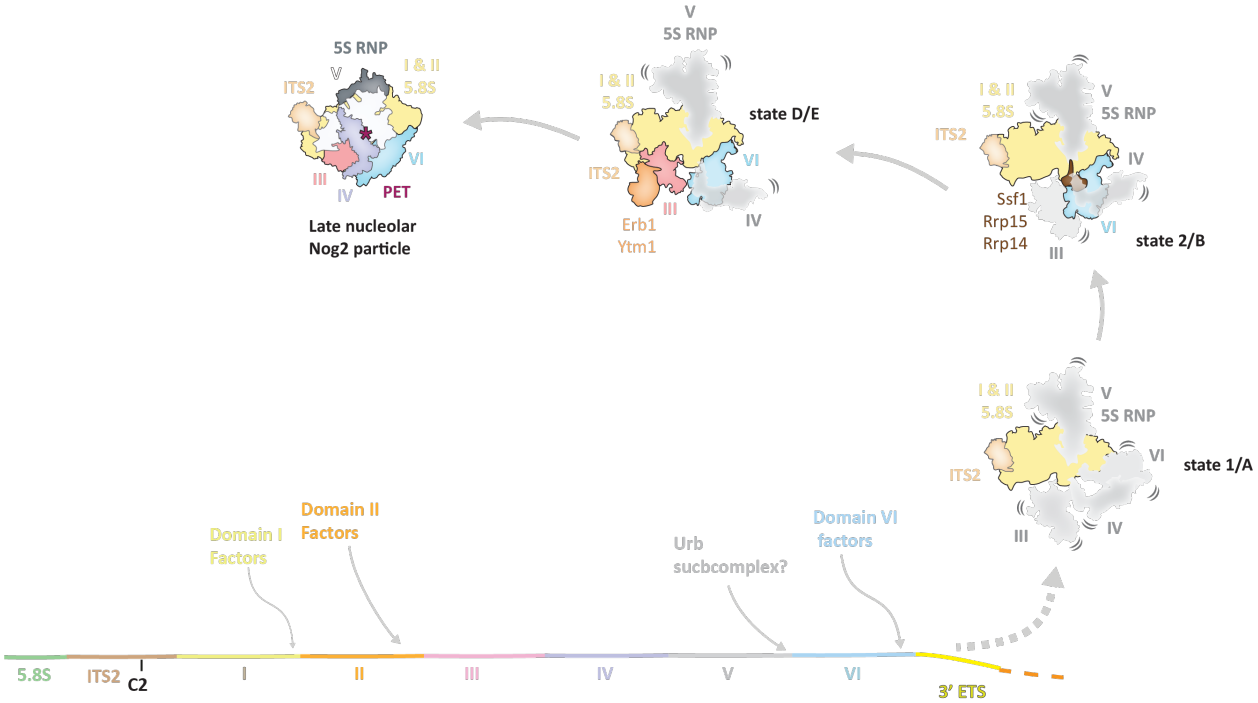

Figure 5.1 Model of pre-60S maturation in the nucleolus. Domains of the 25S rRNA are represented as separate segments that are flexible (in gray) or stably incorporated (in color). State 1 represents an intermediate in which domains I and II are ordered and subsequent folding of either VI will occur (state 2). Further folding of domain III (state D/E), allows for the folding and recruitment of assembly factors by domains IV and V, which leads to the formation of the late nucleolar Nog2 particle. States 1 and 2 were observed in our work, while states A-E were observed in work by Kater et al., 2017, and the Nog2 particle was studied by Wu et al., 2016.

5.1.2 State 3: On pathway intermediate, or degraded pre-60S?

Cryo-EM has revolutionized structural biology for many reasons- in particular, the ability to parse out several unique conformational states from heterogeneous samples has greatly aided the study of large molecular complexes, including ribosome assembly intermediates. With improvements in data collection speed, and data processing tools (Nakane & Scheres, 2021) more and more information can be gleaned from isolated pools of affinity purified assembly particles. There are some limitations to this computational assessment of the samples- how can one order the multiple states observed chronologically, and how can one be sure that the states are biologically relevant or "real"?

On chronology, it can often be determined with support from protein and RNA biochemistry, and previously determined structures. For example, it is almost certain that state 2 from the late-nucleolar/early nuclear Nog2 particles comes after state 1 due to the more mature conformation of the 5S module observed in state 2 (Wu et al., 2016). We know what a "more mature" conformation of the 5S module looks like because of the available structures of mature ribosomes, and so on. The question of order is much less clear when there are no such structural landmarks, and when multiple pathways for a process exist.

The question of whether a state is biologically relevant is especially important for our study of the pre-60S. Our state 3, which featured an ordered domain III and a disordered domain VI, was not observed by the complementary studies on the pre-60S (Kater et al., 2017; Zhou et al., 2018) Our original hypothesis was that state 3 was an alternate intermediate to state 2, where either domain III (state 3) or domain VI (state 2) could be the first to begin to stably fold into the pre-60S core. This hypothesis was particularly appealing, as it paralleled prokaryotic ribosome assembly, where there are multiple alternative orders of ribosomal protein binding that allow for productive ribosome assembly (Davis et al., 2016). Closely examining only our structural data, there are no clear assembly factor placements that would prevent domain III (state 3) from partially folding before domain VI (state 2). Our concern is that the state 3 could in fact not be an actual on-pathway intermediate, but a degraded pre-60S particle. Some level of degradation could have been encouraged by our purification conditions that utilized EDTA, which could destabilize RNA and RNA binding proteins, resulting in the small fraction of total good particles that comprised state 3. It should be noted that low particle number alone does not render a state non-physiological. Repeating the purification and structural characterization with particles purified in magnesium rich conditions could help validate state 3's existence as an on pathway intermediate, but this would take a considerable amount of time.

5.1.3 Accumulated pre-ribosomal particles during stress conditions

Typically, ribosome assembly is most active during exponential growth, but it has been observed that 23S and 27SB rRNA species accumulate under various stress conditions, like high optical densities and rapamycin treatment (Talkish et al., 2016; Kos-Braun et al., 2017). Our lab has taken advantage of this accumulation, and grown yeast under nutrient stress conditions in order to increase the abundance of early nucleolar intermediates of assembly containing these RNAs (Chaker-Margot et al., 2017; Barandun et al., 2017; Sanghai et al., 2018). In complementary work from the Hurt & Beckmann and Ye labs, structures of the 27SB containing pre-60S have been determined from particles isolated from yeast growing under exponential growth conditions (Zhou et al., 2018; Kater et al., 2017). Strikingly, the overall composition and conformation of these particles is, in consideration of the resolution currently available, nearly identical. That is to say that there are no obvious structural/compositional differences marking the particles that were accumulated under stress conditions as unique from those made during normal growth. Are the 27SB containing particles that accumulate under stress unique from the 27SB containing particles made during rapid growth? Additionally, do these accumulated particles reenter the ribosome biogenesis pathway and become mature ribosomal particles?

Our current hypothesis is that both the 23S and 27SB containing particles accumulate under stress so that yeast cells can rapidly return to ribosome assembly once satisfactory growth conditions reoccur. Currently, we have no concrete data supporting that these particles reenter the assembly process besides their highly similar structure to the particles purified from rapidly dividing cells. Researchers have tried to track if the 23S accumulated rRNA is processed into mature RNAs using a pulse-chase approach with radiolabeled uridine. But, it was inconclusive if the accumulated 23S RNAs were processed into mature ribosomes (Kos-Braun et al., 2017). Kos-Braun et al. comment that the rapid speed of ribosome assembly hinders the accuracy of their radiolabeled-Uracil based approach for this experiment. A more rapid

assessment of rRNA processing has been developed in the Tollervey lab using tritium, which allows for as short as 10 second intervals of changes in rRNA processing to be visualized (Kos & Tollervey, 2010). Perhaps utilizing this more rapid approach could conclusively detect if the accumulated 23S and 27SB rRNAs are processed to mature rRNAs.

An alternative hypothesis presented by Kos-Braun et al. is that these rRNAs are produced and accumulate under stress conditions to maintain nucleolar architecture. Even if these are non-productive pre-ribosomal particles, maintenance of the nucleolus by continuous levels of rDNA transcription and production of early intermediates could prevent dissolution of the nucleolus during stress, ensuring that the nucleolus is prepared for high levels of ribosome assembly once positive growth conditions return. To differentiate between the two hypotheses (that the pre-ribosomal particles are being stored for further maturation versus continually made/degraded to maintain nucleolar architecture) would require an experiment where the turn-over of these particles could be tracked.

Lastly, how does the cell signal for these particles to be made but not further processed? Post-translational modification of the pre-ribosomes is an intriguing option, as post translational modifications offer rapid tuning of cellular processes, and yeast cells would benefit from being able to quickly tune ribosome production to cell health/ nutrient availability. Work from Kos-Braun et al. assessed changes in phosphorylation of assembly factors under nutrient limitation, but there was no definitive link between the observed changes and the behavior of the particles and the kinase(s) responsible were not identified (Kos-Braun et al., 2017).

5.2 Capturing a 27SA containing pre-60S: The Urb particle/Urb subcomplex

Our study of the nucleolar pre-60S contributed to our understanding of the structure of 27SB containing pre-LSUs. This 27SA is an even earlier species of pre-60S rRNA, which contains unprocessed portions of ITS1 at its 5'end and the 3'ETS at its 3' end (**Fig 1.5**). To understand RNA folding and the overall architecture of the pre-60S containing a 27SA rRNA, I focused my studies on the Urb subcomplex (Chapter 4). This subcomplex of proteins associates with the 27SA specifically, and is of special interest as it contains a DEAD-box helicase (Dbp6), and our recent data found that it consistently associates with the Box C/D snoRNA machinery and snr190 (**Fig 4.1**). We aimed to study the Urb subcomplex in isolation, and the Urb subcomplex in the context of the pre-60S, referred to as the Urb particle. Structural studies of the Urb subcomplex and Urb particle proved difficult, and stalled at the stage of electron microscopy. Considering the flexibility of the rRNA domains in a 27SB containing particle (Chapter 2), it is very likely that an even earlier particle would contain as much, if not more, flexibility. There is the option, though, that binding of the Urb subcomplex to the pre-60S will create stability in the areas adjacent to the site of subcomplex binding. RNA-protein crosslinking data that identified the RNA in proximity to Urb1 (the largest member of the Urb subcomplex) places the binding site of the Urb subcomplex at the junction of domains I, V, and VI (Joret et al., 2018). Additionally, reassessment of the snr190 sequence found a new potential basepairing location for this snoRNA within domains I and V (Joret et al., 2018). Mass spectrometry based studies found low signal for recruitment of the Urb subcomplex only when domain V is first transcribed (Chaker-Margot & Klinge, 2019). Taken together the Urb subcomplex may interact with the very early pre-60S at the junction of domains I, V, and VI. If this is the case, it may temporarily stabilize this region of the pre-60S. Further, our data shows that the Urb subcomplex not only

contains the previously characterized five nucleolar proteins (Urb1, Urb2, Nop8, Dbp6, and Rsa3), but also consistently co-purifies with the Box C/D snoRNA machinery (**Fig 4.1**). This brings the total mass of the complex closer to 700 kDa. The addition of this over half MDa complex and the possibility of rRNA stabilization may render the Urb particle a promising structural target, despite early challenges in cryo-EM studies.

In particular, the study of these particles may still be successful in the future considering improvements in electron microscopy data collection and data processing that allow for larger datasets to be collected and processed more quickly. Biochemical optimization will also be necessary for successful study of the Urb subcomplex and Urb particle. For the Urb particle, sample quality and concentration could be improved by purifying the sample from yeast grown at a lower optical density. An OD of 2.0 is referred to as "mid-logarithmic" or rapid growth, but close examination of rRNA intermediates as a function of optical density performed by Talkish et al. reveal a more than two-fold greater abundance of 27SA rRNA at OD 1 versus OD 2 (Talkish et al., 2016).

Clever manipulation of the Dbp6 helicase may also aid in the stability or accumulation of the Urb subcomplex and Urb particle. Several dominant-negative mutants of Dbp6 have been identified (Bernstein et al., 2006), and could be expressed in cells depleted of wildtype Dbp6. These Dbp6 mutants may engage the pre-60S, but be unable to disengage, effectively trapping Dbp6-containing pre-60S.

5.3 Dhr1 and Utp14

5.3.1 Current model for Dhr1 regulation and activation

Dhr1 is the DEAH-box helicase responsible for removing the U3 snoRNA from the SSU processome, which is a required step for SSU assembly to progress into the nuclear stages. Before this work, it had been established that Dhr1 was recruited to the SSU processome by Utp14, and that Utp14 activated Dhr1s activity (Zhu et al., 2016). It was unclear the exact mechanism of how this recruitment and activation worked. In this work, biochemical and structural studies of Dhr1 and Utp14, combined with careful evaluation of structures of maturing small subunit processomes, have provided an understanding of the high level of regulation over Dhr1 helicase activity.

In maturing SSU processomes, before the helicase activity of Dhr1 is required, Dhr1 is part of the SSU processome, but bound docked-away from the U3 snoRNA. While docked away, Dhr1 activity is further regulated as Dhr1 is in an auto-inhibited loop bound conformation. The crystal structure of auto-inhibited Dhr1 was characterized in this work (Chapter 2.1). Meanwhile, Utp14, which both recruits Dhr1 to the U3 snoRNA substrate and activates Dhr1 is also being regulated by the rest of the SSU processome. Ours and others biochemical work determined that there are distinct regions of Utp14 which (1) activate Dhr1 ATPase and strand displacement activity and (2) recruit Dhr1 to its substrate U3 snoRNA (Boneberg et al., 2019; Cheng et al., 2020; **Fig 3.8, 3.10)**.

In earlier states of small subunit processome maturation, the future binding site of the recruitment segment of Utp14 is blocked by N-terminal regions of the assembly factor Utp7. Meanwhile, the activating segment of Utp14 (termed Utp14D) is sequestered between the beta-propellers of Utp7 and Utp1. Upon dissociation of Utp7 and other proximal factors that

have completed their roles in assembly, both Upt14D and Dhr1 are released from their previous binding sites, and the recruitment segment of Utp14 can bind near Pno1 and the pre-18S. The C-terminal domain of Dhr1 can now be recruited by Utp14, shifting the helicase core of the enzyme into close proximity of the U3 snoRNA, allowing it to bind to a single stranded region of the U3. Utp14D is now disordered, and should be available to interact with and increase Dhr1 catalytic activity (**Fig 5.2**).

Further, our biochemical data shows that activation by Utp14 is fine tuned to necessitate the essentially intramolecular reaction conditions that is created by the architecture of the maturing processome. These pre-ribosomal particles act as platforms to bring helicase, substrate, and activator into close proximity. In strand displacement assays, fusions of Dhr1 and Utp14 had much greater activity than reactions containing Dhr1 and Utp14 in trans. Despite high and equimolar concentrations of Dhr1 and Utp14, a fusion of the two proteins was necessary to achieve almost complete consumption of the RNA substrate in our assay (**Fig 3.11**). In these reactions, the fusion more closely mimics the enforced proximity of factors in the SSU processome, and the greater stand displacement activity of these fusion constructs indicates the necessity of this high level of coordination in the context of the SSU processome for efficient Dhr1 action. These observations are also in accordance with our understanding of DEAH-box helicase biology. DEAH-boxes have almost no specificity for RNA substrates in their helicase cores (Tauchert et al., 2017; Boneberg et al., 2019; reviewed in Sloan & Bohnsack, 2018). Therefore, to reduce their random action on off-target RNAs, it is ideal that the activity of DEAH-boxes is highly regulated.

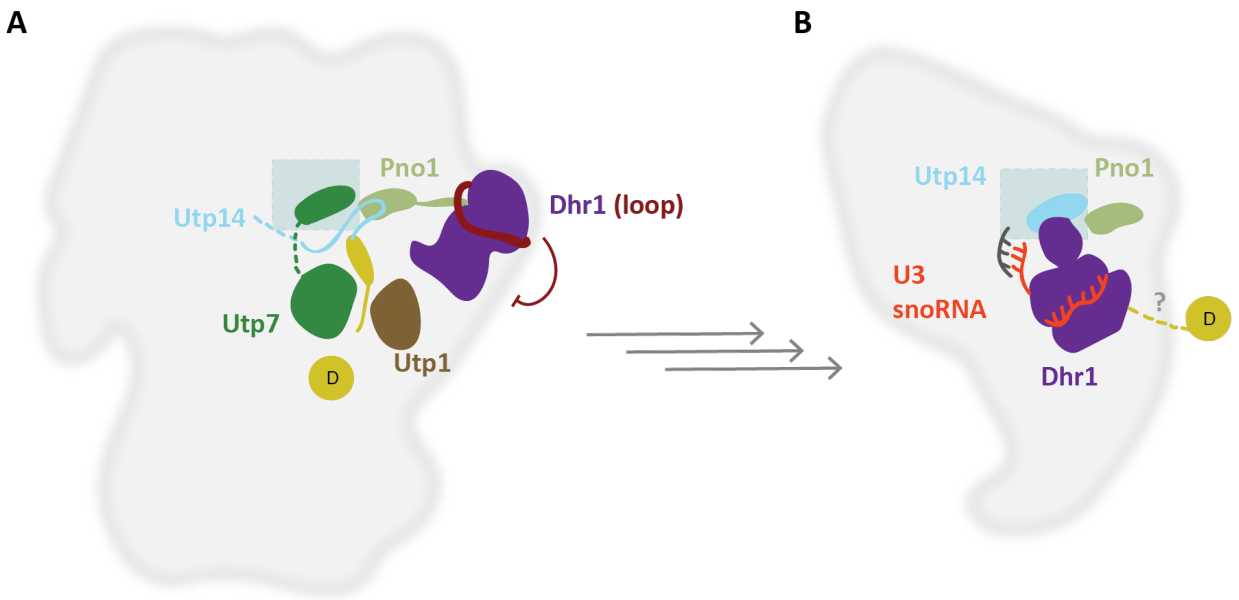

Figure 5.2 Utp14 and Dhr1 are tightly controlled in maturing SSU intermediates to tune Dhr1 helicase activity. A) Before the maturing SSU processome requires Dhr1 activity, Dhr1 is sequestered from its active site and is in its auto-inhibited state. Meanwhile the Utp14 activating segment (Utp14D, yellow) is held between Utp7 and Utp1, and the biding site for the segment of Utp14 that recruits Dhr1 is blocked by N-terminal region of Utp7 (light green box). **B**) After the dissociation of many early assembly factors, the binding site for the Utp14 segment that recruits Dhr1 is now available (green box). Dhr1 can interface with the recruitment segment of Utp14, engage a single stranded segment of U3 snoRNA, and begin helicase activity. Utp7 dissociation has also released the Utp14D activating segment, but Utp14D is disordered and its interaction with Dhr1 is not structurally understood.

The exact mechanism of how Utp14 influences Dhr1 catalytic activity is still elusive. The observed increase in strand displacement activity could be due to an influence of Utp14D on several aspects of the DEAH-box function. The DEAH-box catalytic cycle is discussed in Chapter 1.3 and is as follows: ATP binding causes the RecA domains to close and form a functional ATPase site, while the relative position of the RecA domains to the OB-fold, Ratchet-like, and Winged-Helix domains remains open for substrate RNA binding. When nucleotide and RNA substrate are bound, the OB-fold, Ratchet-like, and Winged-Helix domains rotate closer to the RecA domains and enclose the RNA substrate. The RecA2 domain shifts open after ATP hydrolysis, movement of RecA2 domain allows for an additional nucleotide at the 5' end of the substrate RNA to be accommodated into the RNA binding channel. Closure of the helicase core during the next round of ATP hydrolysis pushes a base at the 3' end of the substrate RNA out of the core. This allows the DEAH-boxes to translocate along RNA, and disrupt the basepairing of the upstream double stranded region of the RNA substrate (reviewed in Gilman et al., 2017 and K. E. Bohnsack et al., 2021) (**Fig 1.12B**). It has been observed in other work that Dhr1 ATPase activity is increased by Utp14 (Boneberg et al., 2019; Roychowdhury et al., 2019; Choudhury et al., 2019). ATP hydrolysis is a central step of the catalytic cycle, so an observed increase in ATPase activity still does not explain exactly how Utp14 is influencing activity.

Although we currently lack structural information for how Dhr1 and Utp14D interact, we can look to other DEAH-box helicases. Prp2 is essential for spliceosome assembly and is very similar to Dhr1 in that it is both recruited to its active site and has its ATPase activity increased by its cofactor Spp2. The interactions between Prp2 and Spp2 from both *C. thermophilum* and *S. cerevisiae* have been structurally characterized in isolation. Additionally, *S. cerevisiae* Prp2/Spp2 have been visualized in context of a spliceosome intermediate. Spp2 interacts with the side of Prp2 that is opposite to the face that opens to bind substrate RNA. Spp2 contacts the RecA2 domain and the Winged Helix domain (**Fig 5.3**).

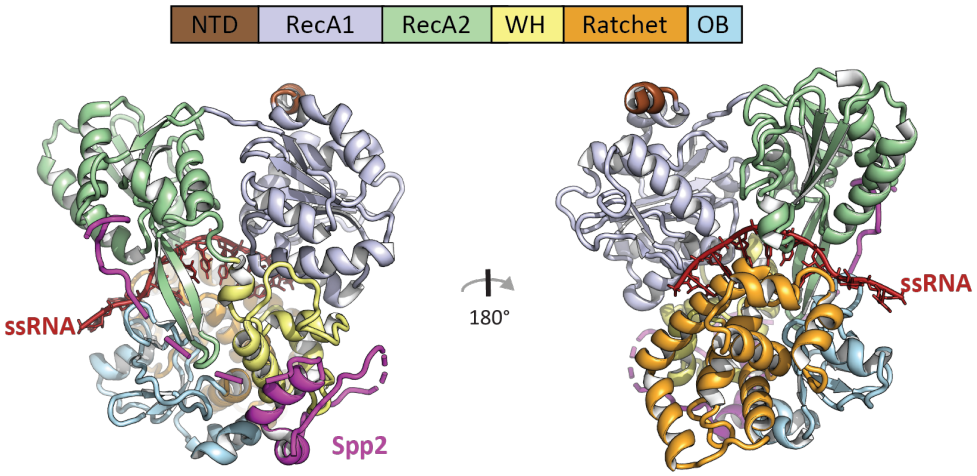

Figure 5.3 Prp2 helicase in complex with RNA and its co-activator, Spp2. Prp2 helicase is bound to ssRNA and the G-patch protein Spp2. Spp2 binds on the opposite face of ssRNA binding. PDB 7DD3

In *C. thermophilum*, the observed differences between Prp2-ADP and Prp22-ADP-Spp2 are subtle, where the Spp2 bound structure has a slight closing of the helicase core (Hamann et al., 2020). In the case of *S. cerevisiae*, there was no observed differences between Prp22 apo, Prp22-Spp2 complex, and Prp2-ADP-Spp2 complex structures (Bai et al., 2021). The binding site of Spp2 is away from the substrate RNA, so it appears unlikely that Spp2 directly influences RNA substrate recruitment. It may influence Prp2's activity by making other steps in the catalytic cycle more favorable. As it contacts both the RecA2 domain and the Winged-Helix domain, on the opposite side of the enzyme from the substrate RNA tunnel, perhaps it increases the processivity of the helicase. By linking the RecA2 domain and the more C-terminal domains of the enzyme, Spp2 could facilitate stability of the helicase core during the catalytic cycle, limiting the extent to which the helicase core can open during cycles of ATP hydrolysis/translocation, and therefore increasing processivity. Although the processivity of a DEAH-box helicase has not been studied specifically as of yet, studies applied to other DNA and RNA translocases could potentially be used for this purpose.

It is also unclear what role the CTD of Dhr1 plays in this process. The CTD is an essential feature of Dhr1, which is necessary for recruitment of Dhr1 to its active site by Utp14. The role of the CTD in Dhr1 helicase activity, if any, remains unclear. The Dhr1 helicase core (ΔNTDDhr1ΔCTD) displays almost no strand displacement activity in our assays, but Dhr1CTD (ΔNTDDhr1) has exhibits low levels of strand displacement. Both constructs can be activated by

Utp14, revealing that the CTD is not required for activation of strand displacement ability. The Dhr1 CTD can bind RNA, as observed in state Dis-C where Dhr1 is recruited to the U3 snoRNA substrate (**Fig 3.8D**). The CTD may only contribute to increased RNA substrate recruitment. Although a direct comparison to the most recent studies on yeast and murine Dhr1 cannot be made as these studies only utilized ATPase assays to assess Dhr1 activity, it is interesting that these studies found that ΔCTD constructs had almost the same level of RNA-dependent ATPase activity as full length constructs (Roychowdhury et al., 2019; Boneberg et al., 2019). Since these are measure of RNA-dependent ATPase activity, it is intriguing that the CTD had no effect on ATPase activity. This may be different due to differences in the RNA substrate utilized in the assays, where our substrate is very long (45 bp on the longer strand) with potential to be contacted simultaneously by the CTD and the RNA substrate tunnel. The ATPase assays performed by other groups utilized a much shorter, U10 RNA strand (Roychowdhury et al., 2019; Boneberg et al., 2019).

To further understand the molecular mechanism of how Utp14 affects Dhr1 activity and what role the CTD plays in activity generally, further biochemical study is required and is described in the next section.

5.3.3 Future experiments towards elucidation of Utp14-Dhr1 interactions and the role of the Dhr1 CTD

Additional biochemistry is necessary to understand the mechanism of Dhr1 activation by Utp14. ATPase assays will complement the strand displacement assays by allowing study of another aspect of Dhr1 activity in the presence and absence of RNA. Fluorescence polarization assays will provide insight into how Dhr1's affinity for its substrate is modulated. This may aid our understanding of what steps of the Dhr1 catalytic cycle are affected by Utp14.
Lastly, structural studies of Utp14 and Dhr1 can reveal the interaction surface of Utp14 and Dhr1, and reveal if Utp14 binding encourages large scale conformational changes in Dhr1.

ATPase assays and Fluorescence Anisotropy Assays

Strand displacement assays have been effective at providing a foundation for understanding how Utp14 and the Dhr1 CTD play a role in Dhr1 activity. A more complete understanding of Dhr1 will come with additional biochemical assays, namely ATPase assays and fluorescence polarimetry assays. ATPase assays will allow us to assess an aspect of Dhr1 activity both in the absence and presence of RNA. Previous work has shown that Dhr1 ATPase activity is stimulated by RNA and can be greater stimulated by Utp14 (Boneberg et al., 2019; Roychowdhury et al., 2019; Choudhury et al., 2019). But, there is very little data explaining how Utp14 affects Dhr1 ATPase activity in the absence of RNA. In an RNA free assay, we will also be able to confirm that the effects of Utp14F are strictly RNA-binding dependent if Utp14D and Utp14DEF activate Dhr1 ATPase activity to the same extent. RNA-free assays will also be important for assessment of the role of the Dhr1 CTD, which also has RNA binding ability (as seen in maturing SSU processome structures, **Fig 3.8D**).

Fluorescence polarimetry (FP) is a powerful tool to assess the affinity of a molecule of interest for a fluorescently labelled moiety. Currently, I have labelled U10 RNA and labelled Utp14D peptide available for FP analysis. Here we can figure out if Dhr1 has increased affinity for RNA in the presence of Utp14. We can also find the reverse- does ssRNA RNA binding by

Dhr1 increase the enzyme's affinity for Utp14D? FP assays will also allow further study of the role of the CTD, as in our ATPase assays. We can test how the CTD influences the affinity of Dhr1 for both ssRNA and Utp14D. These data could help us rationalize the trends observed in our strand displacement and ATPase assays, and allow us to make a more complete model of both the Dhr1 C-terminal domain's role in activity and the activation of Dhr1 by Utp14.

Potential for Dhr1 and Utp14 co-crystal structure

At the time of writing, our contribution to the understanding of Dhr1 activation by Utp14 has been through in vitro biochemical assays. Attempts at co-crystallizing Dhr1 and Utp14 have so far been unsuccessful. These attempts used both Dhr1 fused to Utp14, and Dhr1 co-crystallized with Utp14D peptide. The vast majority of 96-well crystallization condition screening was done in the presence of ADP and $MgCl_2$. Promising avenues for future crystallization studies could utilize other nucleotides (ATP analogs like AMP-PNP, transition state analogs like ADP-BeF_3) and could also include RNA. Insights from future experiments utilizing fluorescence polarimetry (described above) can be used to more logically plan future crystallography studies. For instance, if ssRNA increases Dhr1's affinity for Utp14D, it may be that co-crystallizing Dhr1, Utp1D, and ssRNA is worth pursuing. How different nucleotides affect Dhr1's affinity for Utp14D and RNA can also be revealed in these assays, and can help pick the ideal nucleotide for the most high-affinity co-crystallization conditions. We can also consider data on DHX37, the murine homolog of Dhr1. Fluorescence polarimetry assays found that affinity for ssRNA by DHX37 was reduced in the presence of ADP or AMPPNP. But, Utp14 increases the affinity of DHX37 for RNA, and further increases DHX37 affinity for RNA in the presence of nucleotides (Boneberg et al., 2019). Therefore, it may be promising to try crystallization with Utp14D, RNA, and in the presence and absence of nucleotide as well.

It is important to note that a co-crystal structure of Dhr1 and Utp14 would only contribute a piece to our understanding of the activation mechanism and may not provide clear mechanistic insight. A recent series of cryo-EM and crystal structures of a DEAH-box helicase, Prp2, and its cofactor illustrated how structural information may be not provide clear mechanistic details of co-activator function. As discussed above in section 5.3.1, the structures of Prp2 and Spp2 did not reveal any large conformational changes to the Prp2 helicase caused by Spp2 binding (Bai et al., 2021; Hamann et al., 2020). If structures between Utp14 and Dhr1 reveal similar results, where there is no clear, large scale rearrangement of the Dhr1 domains due to Utp14 binding, an understanding of the Utp14-Dhr1 surface interactions could still provide key information that could be used to design mutations for further biochemical studies.

5.4 The nucleolus: How is early assembly regulated in a membraneless organelle?

The rDNA loci are located in the nuclear subcompartment called the nucleolus. This is a non-membrane contained organelle defined by the presence of the rDNA. In most eukaryotic cells, the nucleolus has two phases. They have a single Fibrillar Component (FC) that is nested within the Granular Component (GC). In higher eukaryotes, the nucleolus has three phases. In these cells, nucleoli contain FCs, which are located within Dense Fibrillar Centers (DFCs). Multiple DFCs exist within the Granular Component, which remains outermost layer of the nucleolus.

At the time, the study of nucleoli from human cells has been the most thorough. The FC contains the rDNA loci and the RNA PolI machinery, the DFC contains fibrillarin (the human homolog of Nop1) and the proteins necessary for the very first steps of assembly. The granular component contains nucleophosmin, other assembly factors, and ribosomal proteins (reviewed in Lafontaine et al., 2021). As the nucleolus has a complex architecture, our future understanding of the earliest stages of ribosome biogenesis will be intimately tied to our understanding of the organization of the nucleolus. Currently, I believe there are many interesting basic and unanswered questions about nucleolar function and architecture, like: How are early assembly factors organized within the nucleolus? How are pre-ribosomes "moved" out of the nucleolus and into the nucleoplasm when there is no membrane or pore to transit? How exactly are nucleolar factors recruited to the nucleolus?

A detailed understanding of the movement throughout the nucleolus will likely be best answered with sophisticated live-cell super-resolution microscopy. Foundational works towards this goal have been accomplished in work in humans and yeast using fluorescently tagged factors involved in rDNA transcription, nucleolar integrity, and ribosome assembly (Yao et al., 2019; Tartakoff et al., 2021) Another emerging field is cryo-electron tomography. Work has already been done searching for pre-ribosomes in cells using tomography, and with greater improvements in this technique it may be able to better understand how ribosome assembly is organized within cellular compartments (Delavoie, 2019).

The architecture of the nucleolus is determined by both the RNA and protein identity and concentration. Several studies have highlighted how active rDNA transcription is necessary for the nucleolus to form, and how RNA binding by the RNA-interacting domains of nucleolar proteins is key to nucleolar architecture (Feric et al., 2016; reviewed in Lafontaine et al., 2021). It has now been well established that RNA is a key component for ribonucleoprotein granules, where the nature of the RNA involved can tune the biophysical properties of these granules (reviewed in Rhine, Vidaurre, & Myong, 2020). With the importance of RNA for phase separation in mind, we can return to the architecture of the nucleolus. Lafontaine et al. postulate that the recent evolutionary emergence of the three phase nucleoli (vs the two-phase nucleoli in lower eukaryotes like yeast) corresponds with an increase in the length of the non-transcribed spacer sequences in the rDNA loci (Lafontaine et al., 2021). Perhaps more convincingly, new data from our lab on small subunit assembly in human cells (Singh et al., in review) finds the same evolutionary increase in the length of the *transcribed* spacers: the 5'ETS sequences are also much longer in human than in yeast. Further, the structures of human small subunit intermediates show that only a small portion of the 5'ETS is necessary to form the base of the SSU processome by binding the necessary assembly factors and basepairing with the U3snoRNA (Singh et al., in review). A large majority of the 5'ETS is therefore unstructured, and may be free to form interactions that promote phase separation. Most strikingly, expression of truncated 5'ETS sequences lacking these expansion segments can still be processed into mature ribosomes. This implies that the expansion segments have other roles outside of pre-small subunit architecture, perhaps in nucleolar architecture and organization. This can let us return to the question of how pre-ribosomal particles transit out of the nucleolus at the appropriate time. The recent data on the human SSU processome suggests the 5'ETS has dual roles: a small portion serves a scaffold for the SSU processome formation and the remainder acts to promote nucleolar architecture. This has led to a hypothesis where removal of these elements, triggered

by the activity of the exosome, allows for the maturing SSU to exit from the nucleolus into the nucleoplasm via a reduction in the RNA-protein contacts directly linked to the maturing small subunit particles. It will be of great interest to see if sequence analysis of the other ribosomal spacer fits the trends of the non-transcribed spacers and 5'ETS that has been observed. In particular, if the length of ITS2 sequences are also greatly increased in the human genome versus the yeast genome, there is the opportunity that ITS2 acts in large subunit biogenesis as the 5'ETS does in small subunit biogenesis, serving roles in both nucleolar and pre-ribosomal architecture.

Proving the biological role of these expansion segments is a daunting task. Manipulating the rDNA in any cell is made difficult because of the large number of repeats and their essential nature. In yeast, there are several engineered strains of *S. cerevisiae* where rDNA repeats have been removed and the only rDNA present is expressed on plasmids (Wai, 2000). No equivalent strain has been made for the study of human cells as of yet. Further, reduction of native rDNA transcription via bypassing PolI transcription and expressing engineered rDNAs of interest using PolII specific promoters seems an unlikely option. In yeast, rDNA can be expressed on plasmids to appreciable levels using PolII promoters, but this does not seem possible in human cells (Arnaud Vanden Broeck, personal communication). A more indirect approach would be to utilize yeast instead, and attempt to "humanize" the yeast rDNA. Using the engineered yeast where the native rDNA has been removed, a plasmid expressing rDNA with humanized spacer sequences can be expressed and nucleolar architecture of the cells could be assessed using tools like transmission electron microscopy and fluorescence microscopy. I would hypothesize that the change in rRNA length could be enough to alter the nucleolar architecture to appear tripartite, and therefore more "human-like".

5.5 Outlook

Ribosome assembly is a complex process central to the survival of any living organism. Over 200 trans-acting assembly factors work to fold and chaperone the ribosomal RNA and recruit the ribosomal proteins to their proper binding sites. As the ribosome is a ribozyme, special effort is taken throughout ribosome biogenesis to form and protect the maturing active sites created by the rRNA. Structural snapshots of ribosome assembly intermediates have offered great insight into how this is accomplished in yeast cells. With structural information from the nucleolus, nucleus, and cytoplasm, we have attained a great wealth of knowledge spanning the roles of individual assembly factors to the overall trends of ribosome biogenesis of both the small and large subunit. There are still many areas of ribosome biogenesis left to explore. The very earliest stages of ribosome assembly at the interface of rDNA transcription and the recruitment of the first assembly factors and first steps of RNA folding are not fully understood. I think this will be especially interesting for the study of the large subunit, where the understanding of the very earliest stages of assembly have not been well-explored, and the cross-talk between small and large subunit biogenesis is still quite mysterious. The earliest steps of assembly are tied to the nature of the nucleolus, where the rDNA is located and ribosome biogenesis begins. Exactly how ribosome biogenesis is regulated in this membraneless sub-compartment of the nucleus is still an open question. Lastly, the understanding of human ribosome biogenesis is emerging due to improvements in techniques for the genetic manipulation of human cells and breakthroughs in cryo-electron microscopy. In the future, a fuller understanding of ribosome assembly in human cells will greatly complement the existing wealth of data on this process in yeast and hopefully lead to a more complete understanding of this critical cellular process.

Chapter 6: Methods

6.1 General methods

Molecular Cloning

All cloning of plasmids was carried out with standard restriction enzymes (New England Biolabs) and T4 DNA ligase (New England Biolabs), Phusion DNA polymerase (made in lab) and Dh5α or Stbl3 *E. coli* competent cells.

C-terminal Tagging of Endogenous Genes in Yeast

DNA fragments containing affinity tags (typically linker-protease site- affinity handle-antibiotic cassette) were amplified from tagging plasmids (**Table 6.1**). Primers were used that introduced 50 bp stretches that are homologous to the C-terminus of the target gene. Per yeast transformation, 10 mL of yeast culture were grown at 30 °C to an optical density of 0.4-0.5 and then pelleted. Pellets were washed twice with ddH_2O and once with 1x TE (100 mM Tris-HCl pH 7.5, 10 mM EDTA) supplemented with 100 mM Lithium Acetate. Cells were resuspended in 50 µL of 1x TE/100 mM Lithium acetate with 40% PEG 4000, 500 ng- 1 µg of tag DNA fragment, and 50 µg of salmon sperm DNA. Cells are incubated for 30 mins at 30 °C, and then heat shocked at 42 °C for 15 minutes. Cells are recovered at 30 °C for 2-4 hours in non-selective YPD media with 2% glucose and then plated on YPD-agar containing selection markers. All strains made are listed in Table 6.2.

Table 6.1 Plasmids used to generate affinity tags for endogenous yeast tagging.

Plasmid number	Description (base plasmid, affinity tags)	Yeast selection marker
pSKB392	pSK_B392-pFA6a-linker-tev-mCherry_G418	G418
pSKB378	pSK_B378-pFA6a-linker-tev-bc5_G418_clone1A	G418
pSKB407	pSK_B407_pFA6a-linker-H14-3c-GFP_hygromycinB	HygromycinB
pSKB372	pSK_B372_pFA6a-linker-sbp_Nourseothricin	Nourseothricin
pSKB395	pSK_B394_pFA6a-linker-3c-mCherry_G418	G418

Table 6.2 Yeast strains generated for this work.

Strain Name (Genes of interest)	Genotype	Yeast Selection Marker
Y305 (Rrp5-3c-bc5 and Rsa3-tev-mcherry)	MATa his3Δ leu2Δ0 met15Δ0 ura3Δ0 UTP1-3myc-GFP-3FLAG::HphMX4 Rrp5-linker-3c-bc5::ClonNat Rsa3-linker-tev-mCherry::kanMX6	HygromycinB/ Nourseothricin / G418
Y311 (Urb2-h14-3C-GFP and Rsa3-TEV-bc5)	MATa his3Δ leu2Δ0 met15Δ0 ura3Δ0 Urb2-linker-H14-3c-GFP::HphMX4 Rsa3-linker-TEV-bc5::kanMX6	HygromycinB/ G418
Y272 (Nsa1-linker-tev-GFP and Nop2-linker-sbp	MATa his3Δ leu2Δ0 met15Δ0 ura3Δ0 Nsa1-linker-tev-GFP::HphMX4 Nop2-linker-sbp::ClonNat	HygromycinB/ Nourseothricin
Y308 (Nsa1-linker-tev-GFP and Nop2-linker-3c-BC5)	MATa his3Δ leu2Δ0 met15Δ0 ura3Δ0 Nsa1-linker-tev-GFP::HphMX4 Nop2-linker-3c-bc5::kanMX6	HygromycinB/ G418
Y292 (Purchased from Yeast Tet-Promoters Hughes collection, doxycycline repressible Dhr1)	pECM16::kanR-tet07-TATA URA3::CMV-tTA MATa his3-1 leu2-0 met15-0	G418/ Uracil

Negative Stain

Carbon coated copper grids (Electron Microscopy Sciences, CF200-CU-50) were glow discharged for 30 seconds at 50% power under vacuum. 3.5 µL of protein samples were placed on the grids for 30 seconds, and blotted with filter paper. The grids were then washed with 2 x 5 µL of ddH2O and then 2 x 5 µL of 2% uranyl acetate (Electron Microscopy Sciences). Images were recorded on a Philips CM10 at 100 kV with a XR16-ActiveVu (AMT) camera at approximately 52,000 magnification and a pixel size of about 2.7 Å. Small negative stain datasets were processed using EMAN2 software (Tang et al., 2007) and 2D classification was performed in EMAN2 and also using the ISAC program (Z. Yang, Fang, Chittuluru, Asturias, & Penczek, 2012b).

RNA extraction and Northern blotting

Purified samples or whole cells were extracted using 0.5 – 1 mL of TRIzol (Life Technologies) according to the manufacturer's instructions. RNA samples were flash frozen and stored at -80 °C until further use.

For assessment of large RNA species (>500 bp), purified RNA was mixed with formaldehyde running buffer containing bromphenol blue dye and separated on denaturing 1.2% Formaldehyde-Agarose gel (SeaKem LE, Lonza) run at 75 volts. Large gels were run with 2 µL (2 ug) of Millenium and/or Century-Plus Markers (Thermofisher). For assessment of small RNA species (< 500 bases), pufied RNAs were mixed with Urea loading buffer and no dye and were separated on denaturing 10% Urea-PAGE run at a constant 5-10 Amps (must keep voltage below 140 V). Urea PAGE were run with 1 µL (1 ug) of Century-Plus Marker (Thermofisher) and/or 1 µL (0.5 µg) of low range ssRNA ladder (New England BioLabs). Wells of the Urea-PAGE were cleared of precipitated Urea immediately before loading the sample.

After staining the gel in 1X SYBR Green II (Lonza) ddH_2O solution (pH 7.5) for 30 min, RNA species were visualized with a Gel Doc EZ Imager (Bio-Rad) and then transferred onto a cationized nylon membrane (Zeta-Probe GT, Bio-Rad) using downward capillary transfer in case of the agarose gel and a Trans Blot SD semi-dry transfer cell (Bio-Rad) for the Urea-PAGE gel. Note here that for large agarose-formaldehyde gels, staining in SYBR Green II often produced images of RNA content that were misleading.

RNA was cross-linked to the membrane for Northern blot analysis by UV irradiation at 254 nm with a total exposure of 120 milli- joules/cm^2 in a UV Stratalinker 2400 (Stratagene). Here, cross linked membranes could be incubated with methylene blue to assess the level of RNA transfer and provide a chance to manually label the positions of the molecular weight ladder. Cross-linked membranes could also be sandwiched between blotting papers, wrapped in plastic wrap, and stored at -80 °C until radioactive probing.

Cross-linked membranes were incubated with hybridization buffer (750 mM NaCl, 75 mM trisodium citrate, 1% (w/v) SDS, 10% (w/v) dextran sulfate, 25% (v/v) formamide) at 65°C for 30 min prior to addition of γ-^{32}P-end-labeled DNA oligo nucleotide probes. Oligo nucleotides used for Northern Blotting are in Table 6.3.

Probes were hybridized for 1 hour at 65 °C and then overnight at 37 °C. Membranes were washed once with wash buffer 1 (300 mM NaCl, 30 mM trisodium citrate, 1% (w/v) SDS) and once with wash buffer 2 (30 mM NaCl, 3 mM trisodium citrate, 1% (w/v) SDS) for 20 min each at 45°C. Radioactive signal was detected by exposure of the washed membranes to a storage phosphor screen which was scanned with a Typhoon 9400 variable-mode imager (GE Healthcare).

6.2 Methods specific to the study of the nucleolar Pre-60S

Purification of the Nucleolar Pre-60S

Note: Purification of the nucleolar Pre-60s was first started by Sebastian Klinge and optimized by Zahra Sanghai.

The 27SB containing nucleolar pre-60S was purified from a *Saccharomyces cerevisiae* BY4741 strain containing a TEV protease-cleavable C-terminal GFP tag on Nsa1 (Nsa1-linker-TEV-GFP) and a C-terminal 5 x beta-catenin 3C protease-cleavable tag on Nop2 (Nop2-linker-3C-Bc5), for endogenous expression. Yeast cultures were grown in full synthetic drop-out (SD) media containing 2% raffinose (w/v) at 30 ºC to an optical density (OD) of 0.8-1, prior to addition of 2% galactose (w/v) for 16 hours, reaching saturation (OD 5-6). Cells were then harvested by centrifugation at 4000 x *g* for 10 minutes at 4 °C. The cell pellet was washed with ice cold ddH_2O twice, followed by a wash with ddH_2O containing protease inhibitors (E64, Pepstatin, PMSF). Washed cells were immediately flash frozen in liquid nitrogen and stored in -80 °C freezer. Cells were lysed by 4 cycles of cryogenic grinding using a Retsch Planetary Ball Mill PM100. Cell powder was stored in the -80 °C for a maximum of 24 hours before use in a purification.

The freshly ground yeast powder was resuspended by vortexing in buffer A (50 mM Tris-HCl, pH 7.6 (20 °C), 150 mM NaCl, 1 mM EDTA, 1 mM DTT, 0.1% Triton-X100, PMSF, Pepstatin, E-64), removing the insoluble fraction by centrifugation at 4 °C, 40,000 x *g* for 30 min. The supernatant was subsequently incubated with anti-GFP nanobody beads (Chromotek) for 3 hours at 4 °C, with agitation. The beads were washed four times in ice-cold buffer A before the bound proteins were eluted via TEV-protease cleavage (1 hour, 4 °C). The eluate was then incubated with NHS-sepharose beads (Sigma) coupled with anti-beta-catenin nanobody in buffer B (50 mM Tris-HCl pH 7.6 (20 °C), 150 mM NaCl, 1 mM EDTA, 1 mM DTT) for 1 hour at 4 °C with agitation. For electron microscopy (EM) sample preparation, the anti-beta catenin beads were washed once with buffer B, before cleavage by 3C protease for 1 hour at 4 °C, releasing the Nsa1-Nop2 containing nucleolar pre-60S. For protein-protein cross-linking analysis the eluate from GFP-nanobody beads was incubated with beta catenin-nanobody beads in buffer C (50 mM HEPES-NaOH pH 7.6 (4 °C), 150 mM NaCl, 1 mM EDTA) and eluted in the same buffer through 3C-protease cleavage. The eluted sample typically measured an absorbance at 260 nm (A260) of 2.4 to 4.5 mAU (Nanodrop 2000, Thermo Scientific).

Cryo-EM sample and grid preparation

Cryo-EM grids were prepared on four different occasions for the 4 data sets obtained (ds1-ds4). The nucleolar pre-60S eluate in sample buffer B (above) was left as is (ds1 only), or supplemented with 0.1% Triton X-100 and 5 mM $MgCl_2$ (final concentration, ds2-ds4). Copper grids of 400 mesh with lacey carbon and an ultra-thin carbon support film were used (Ted Pella Inc, product no. 01824) for data collection. A volume of 3 to 4 µl of nucleolar pre-60S sample (A260 of 2.5) was applied onto glow-discharged grids and plunged into liquid ethane using a Vitrobot Mark IV robot (FEI Company) (100 % humidity, blot force of 0 and blot time 3.5-4 s).

Cryo-EM data collection and image processing

A total of 14,201 micrographs were obtained over four data collections (ds1 - ds4) on a Titan Krios (FEI Company), at 300 kV, with a K2 Summit detector (Gatan, Inc.). SerialEM (Mastronarde et al., 2005) was employed for data acquisition using a defocus range of 1.0- 3.5 µm with a pixel size of 1.3 Å. Super-resolution movies with 32 frames were collected using a total dose of 10 electrons per pixel per second with an exposure time of 8 seconds and a total dose of 50 electrons per $Å^2$.

Upon data collection, the movies were gain corrected, dose weighted and aligned with Motioncor2 (Zheng et al., 2017), and the contrast transfer function (CTF) was estimated using CTFFIND 4.1.5 (Rohou & Grigorieff, 2015). Relion 2.1 (Kimanius, Forsberg, Scheres, & Lindahl, 2016) was used for all subsequent particle picking, classifications and refinements. Corrected and aligned micrographs were first subjected to autopicking in Relion, resulting in a total of 1,653,290 selected particles from all 4 data sets. After manual inspection of all micrographs, particles were extracted with a box size of 480 pixels (2X-binned to 240 pixels), and 2D-classified separately for each individual data set. After 2D classification, bad classes were removed, and the selected particles of each data set were 3D-classified into four classes using an initial 3D model obtained from cryoSPARC (Punjani et al., 2017), low-pass filtered to 60 Å. The best one to two classes from each 3D classification were selected and their particles were re-extracted with a box size of 480 pixels (un-binned). A combined total of 514,746 particles were finally used for 3D auto-refinement and post-processing with a solvent mask around the "core" containing domains I and II of the 25S rRNA, resulting in an overall resolution of 3.4 Å for state 1. A subsequent round of 3D classification without image alignment of these particles into 6 classes, was used to obtain the two classes that contained states 2 and 3 at 39% and 41% respectively of the total particles. A refinement of the class containing state 2 (201,114 particles) was performed using a mask to include the additional visible densities, comprising of domain VI and its associated proteins, to obtain a final map at 3.7 Å. By conducting an additional round of focused 3D classification without image alignment on this class with a mask around Mak11 and the neighboring segment of domain V of the 25S rRNA, a subset of particles emerged with improved density. This was refined to provide a more continuous map of Mak11 and domain V (state 2A).

Due to particle heterogeneity in the initial class containing state 3 (211,534 particles), a focused classification without image alignment of that class of particles was performed using a mask around the additional density containing domain III of the 25S rRNA, Erb1-CTD (WD40) and Ytm1 (WD40). The best class from this round of classification (31,419 particles) was refined with a mask around the entirety of state 3, to obtain a final map at 4.6 Å resolution. The local resolution of the maps were calculated using Resmap (Kucukelbir, Sigworth, & Tagare, 2014).

Model building and refinement

By using the structure of the late nucleolar Nog2 particle (PDB 3JCT, Wu et al., 2016) as reference, common assembly factors and ribosomal proteins were manually located and fitted into the density, using Cic1 and Rpl7 as hallmark anchors. Protein-protein interactions were confirmed by crosslinking and mass spectrometry analyses (described below). New assembly factors Mak16, Rrp1, Nop16, Erb1-NTD, Rrp14, Rrp15 and Ebp2 and segments of rRNA were modeled *de novo*. Previously determined crystal structures of assembly factors Nsa1

(PDB 5SUI) (Y.-H. Lo, Romes, Pillon, Sobhany, & Stanley, 2017), Ytm1, Erb1-CTD (PDB 5CXB) (Wegrecki, Rodríguez-Galán, la Cruz, & Bravo, 2015) were docked and manually adjusted. Has1, Ssf1, Brx1, Rpf1 and Mak11 were docked from Phyre2 models initially and adjusted to fit the density (Kelley, Mezulis, Yates, Wass, & Sternberg, 2015). Model building was performed with COOT (Emsley & Cowtan, 2004). An annotated list of individual protein IDs, reference models and corresponding maps used for building, can be found in Table S2. The model was refined against a half-map1 from the overall 3.7 Å map of state 2 in PHENIX with phenix.real_space_refine using secondary structure restraints for proteins and RNAs (Adams et al., 2010). Refinement and model statistics can be found in Table 7.1

Map and model visualization

All map and model analyses and illustrations were made using Chimera (Pettersen et al., 2004) and PyMOL Molecular Graphics System, Version 1.8 Schrödinger, LLC. Density map visualization for certain figures was also performed on UCSF ChimeraX, developed by the Resource for Biocomputing, Visualization, and Informatics and the University of California, San Francisco (supported by NIGMS P41-GM103311).

DSS cross-linking sample preparation and mass spectrometry analysis

The tandem-affinity purified nucleolar pre-60S (Nsa1/Nog2-particle), eluted off anti-beta catenin nanobody beads (in 50 mM HEPES-NaOH pH 7.6 (4 °C), 150 mM NaCl, 1 mM EDTA, 1 mM DTT) at an absorbance of 1.0 at 260 nm (Nanodrop 2000, Thermo Scientific) were pooled (total volume 300 µl) and split into three 100 µl cross-linking reaction aliquots.
To each aliquot, 8.8 µl of Disuccinimidylsuberate (DSS; 25 mM in DMSO, Creative Molecules Inc.) was added to yield a final DSS concentration of 2.0 mM and samples were cross-linked for 30 minutes at 25 °C with 450 rpm constant mixing. The reactions were quenched with 50 mM ammonium bicarbonate (final concentration) and precipitated by adding methanol (Alfa Aesar, LC-MS grade) to a final concentration of 90% followed by incubation at -80 °C overnight. Precipitated cross-linked nucleolar pre-60S were combined into one tube by repeated centrifugation at 21,000 x *g*, 4 °C for 30 minutes. The resulting pellet was washed three times with 1 ml cold 90% methanol, air-dried and finally resuspended in 50 µl of 1X NuPAGE LDS buffer (Thermo Fisher Scientific).

DSS cross-linked samples were processed as in (Barandun et al., 2017), and as described below. DSS cross-linked nucleolar pre-60S in LDS buffer were reduced with 25 mM DTT, alkylated with 100 mM 2-chloroacetamide, separated by SDS-PAGE in three lanes of a 3-8% Tris-Acetate gel (NuPAGE, Thermo Fisher Scientific), and stained with Coomassie-blue. The gel region corresponding to cross-linked complexes was sliced and digested overnight with trypsin to generate cross-linked peptides. After digestion, the peptide mixture was acidified and extracted from the gel as previously described (Shi et al., 2014; Shi et al., 2015). Peptides were fractionated offline by high pH reverse-phase chromatography, loaded onto an EASY-Spray column (Thermo Fisher Scientific ES800: 15 cm × 75 µm ID, PepMap C18, 3 µm) via an EASY-nLC 1000, and gradient-eluted for online ESI-MS and MS/MS analyses with a Q Exactive Plus mass spectrometer (Thermo Fisher Scientific). MS/MS analyses of the top 8 precursors in each full scan used the following parameters: resolution: 17,500 (at 200 Th); AGC target: 2×10^5; maximum injection time: 800 ms; isolation width: 1.4 m/z; normalized collision energy: 24%;

charge: 3–7; intensity threshold: 2.5×10^3; peptide match: off; dynamic exclusion tolerance: 1,500 mmu. Cross-linked peptides were identified from mass spectra by pLink (B. Yang et al., 2012a). All spectra reported here were manually verified as previously (Shi et al., 2014).

Northern Blotting

RNA extraction from 33 grams of strain Y292 (Nop2 has sbp tag) purified as described above, except final elution was prepared using buffer C supplemented with 5 mM d-Biotin. Using three rounds of elution, 130 µL of total combined elution was extracted with 1 µL of Trizol. The extracted RNA yield was about 25 µg at 1 ug/µL. 1 µg of extracted RNA was used for visualizing on both Urea-PAGE and formaldehyde gels.

6.3 Methods specific to the study of the Urb subcomplex/ Urb particle

Purification of the Urb particle

The Urb particle was purified from a *Saccharomyces cerevisiae* BY4741 strain containing a TEV protease-cleavable C-terminal mCherry tag on Rsa3 (Rsa3-linker-TEV-mCherry) and a C-terminal 5 x beta-catenin 3C protease-cleavable tag on Rrp5 (Rrp5-linker-3C-Bc5), for endogenous expression. Cells were taken from glycerol stocks of this strain to grow fresh 5 mL starter cultures at 30 C, with shaking, in YPD media supplemented with ampicillin, 2% glucose, 0.4 mg/mL percent Hygromycin-B and 0.3 mg/mL G418 antibiotics. Once these starters reached saturation, they were used to inoculate medium scale cultures of 250 mL in the same media. These were also grown at 30 °C with 250 rpm shaking until saturation. These saturated cultures were diluted (typically 35 mL of saturated starter was diluted into 2 L of YPD media supplemented with 2% glucose and ampicillin) and grown at 30 °C with 250 rpm shaking until an OD of 1.8-2.0 was achieved. Cells were then harvested by centrifugation at 3000 x *g* for 10 minutes at 4 °C. The cell pellet was washed with ice cold ddH_2O twice, followed by a wash with ddH_2O containing protease inhibitors (E64, Pepstatin, PMSF). Washed cells were immediately flash frozen in liquid nitrogen and stored in -80 °C freezer. Cells were lysed by 4 cycles of cryogenic grinding using a Retsch Planetary Ball Mill PM100. Cell powder was stored in the -80 °C for a maximum of 24 hours before use in a purification.

For a large-scale prep (for negative stain grid preparation), approximately 30 grams of yeast powder would be utilized. The freshly ground yeast powder was resuspended by vortexing in buffer A (50 mM HEPES pH 7.6 (20 °C), 200 mM NaCl, 1 mM DTT, 0.1% NP40, PMSF, Pepstatin, E-64), removing the insoluble fraction by centrifugation at 4 °C, 40,000 x *g* for 30 min. The supernatant was subsequently incubated with anti-mCherry nanobody beads (Chromotek) for 3 hours at 4 °C, with agitation. The beads were washed with 200 mL of ice-cold buffer A before the bound proteins were eluted via TEV-protease cleavage (1 hour, 4 °C). The eluate was then incubated with NHS-sepharose beads (Sigma) coupled with anti-beta-catenin nanobody (*18*) in buffer B (50 mM HEPES pH 7.6, 200 mM NaCl, 1 mM DTT) for 1 hour at 4 °C with agitation. The anti-beta catenin beads were washed once with buffer B, before cleavage by 3C protease for 1 hour at 4 °C in buffer B supplemented with 0.05% C12E8 detergent, releasing the Urb particles.

Purification of the Urb subcomplex

The Urb subcomplex was purified from a *Saccharomyces cerevisiae* BY4741 strain containing a 3C protease-cleavable C-terminal GFP tag on Urb2 (Urb2-linker-3C-GFP) and a C-terminal 5 x beta-catenin TEV protease-cleavable tag on Rsa3 (Rsa3-linker-TEV-Bc5), for endogenous expression. Cells were taken from glycerol stocks of this strain to grow fresh 5 mL starter cultures at 30 C, with shaking, in YPD media supplemented with ampicillin, 2% glucose, 0.4 mg/mL Hygromycin-B and 0.3 mg/mL G418 antibiotics. Once these starters reached saturation, they were used to inoculate medium scale cultures of 50 mL in the same media. These were also grown at 30 °C with 250 rpm shaking until saturation. These saturated cultures were diluted (typically 5-10 mL of saturated starter was diluted into 2 L of YPD media supplemented with 2% glucose and ampicillin) and grown at 30 °C with 250 rpm shaking for 16 hours so that cultures were saturated (~OD 8). Cells were then harvested by centrifugation at 3000 x *g* for 10 minutes at 4 °C. The cell pellet was washed with ice cold ddH_2O twice, followed by a wash with ddH_2O containing protease inhibitors (E64, Pepstatin, PMSF). Washed cells were immediately flash frozen in liquid nitrogen and stored in -80 °C freezer. Cells were lysed by 4 cycles of cryogenic grinding using a Retsch Planetary Ball Mill PM100. Cell powder was stored in the -80 °C for a maximum of 24 hours before use in a purification.

For a large-scale prep (for negative stain grid preparation), approximately 30-40 grams of yeast powder would be utilized. The freshly ground yeast powder was resuspended by vortexing in buffer A (50 mM HEPES pH 7.6 (20 °C), 400 mM NaCl, 1 mM EDTA, 1 mM DTT, 0.1% NP40, PMSF, Pepstatin, E-64), removing the insoluble fraction by centrifugation at 4 °C, 40,000 x *g* for 30 min. The supernatant was subsequently incubated with anti-GFP nanobody beads (Chromotek) for 3 hours at 4 °C, with agitation. The beads were washed with 200 mL of ice-cold buffer A before the bound proteins were eluted via 3C-protease cleavage (1 hour, 4 °C). The eluate was then incubated with NHS-sepharose beads (Sigma) coupled with anti-beta-catenin nanobody in buffer B (50 mM HEPES pH 7.6 (20 °C), 200 mM NaCl, 1 mM DTT) for 1 hour at 4 °C with agitation. The anti-beta catenin beads were washed once with buffer B, before cleavage by TEV protease for 1 hour at 4 °C in buffer B supplemented with 0.05% C12E8, releasing the Urb subcomplexes.

RNA isolation and Northern Blotting from the Urb subcomplex

RNA isolation and Northern blotting was performed as described above for the isolation and study of RNA from the Nucleolar Pre-60S. We were interested in snoRNA species, which are less than 300 bases in size, so agarose gels and semi-dry transfer were utilized, as described for Northern Blotting of the 5S. The sequence of the probes for detection of snr190 and snr4 are described in table 5.3.

Table 6.3 Northern Blot Probes

SK lab primer number	RNA Target	Sequence
2222	snr4	ACACAGATGTTACACATGAAC
2223	snr45	GAATTGTTCGATTTGAAACGC
2224	snr190	CGTCATGGTCGAATCGG
1027	25S	TTTCACTCTCTTTTCAAAGTTCTTTTCATCT
2069	ITS2 C2 site	TGGTAAAACCTAAAACGACCGT
1314	5S	CTACTCGGTCAGGCTC
2068	ITS1 3' end	TTAATATTTTAAAATTTCCAG
2070	3' ETS 5' end	CCACTTAGAAAGAAATAAAAA

RNA Seq for the Urb subcomplex

RNA was isolated from purified Urb subcomplex as described above. This RNA was analyzed in a MiSeq Nano (Illumina) by Connie Zhao at the Rockefeller Genomics facility. The resulting reads were analyzed using BowTie 2 (Langmead & Salzberg, 2012) and the *S. cerevisiae* genome from Illumina iGenomes/NCBI.

6.4 Methods specific to the study of Dhr1 helicase and Utp14

Table 6.4 Plasmids used to determine the viability of Dhr1 constructs.

Yeast Plasmid Name	Description
Vector Control	LEU2
Dhr1 Full Length (FL)	$DHR1_{Promoter}$-DHR1-3myc-eGFP LEU2
Dhr1ΔLoop	$DHR1_{Promoter}$-dhr1$_{(\Delta 645\text{-}727,\ insert\ GGTSGG)}$-3myc-eGFP LEU2
Dhr1ΔCTD	$DHR1_{Promoter}$-*dhr1*$_{(1\text{-}1185)}$ LEU2
Dhr1CTD	$DHR1_{Promoter}$-dhr1$_{(1186\text{-}1267)}$ LEU2
Dhr1ΔCTD-Utp14	$DHR1_{Promoter}$-dhr1$_{(1\text{-}1185)}$-UTP14 LEU2

Screen to determine the viability of Dhr1 constructs

A yeast strain containing Dhr1 under the control of a doxycycline repressible promoter was purchased from the Yeast Tet-Promoter Hughes Collection (strain YMR128W). The genotype of this strain is pECM16::kanR-tet07-TATA URA3::CMV-tTA MATa his3-1 leu2-0 met15-0. This strain was transformed with LEU2 containing plasmids described in supplementary table X, according to standard procedures. Individual transformants were grown to saturation in synthetic drop out media containing 2% glucose, 0.3 mg/mL G418, and lacking Uracil and Leucine (SD Ura- Leu-). Saturated cultures were diluted in sterile ddH_2O to an optical density of 1 and serial 10-fold dilutions were prepared. Ten µL of each dilution were placed on SD Ura- Leu- agar plates supplemented with 10 µg/mL doxycycline and left to incubate at 23, 30, or 37 °C for 40 hours.

Expression of the Dhr1 constructs was confirmed using Western Blotting. Cells were taken from the plates used to screen viability of Dhr1 constructs (see above section) and grown until saturation in SD Ura- Leu- media. Cells were pelleted at 1,800 xg, and subsequently

resuspended in buffer (20 mM Tris pH 7.6, 500 mM NaCl, protease inhibitors (E64, Pepstatin, and PMSF). Cells were then lysed using autoclaved 0.4-0.6 mm glass beads by 5 rounds of high speed nutating for 20 seconds, alternating with resting on ice for 20 second periods. An additional 500 µL of buffer were added, the cells were mixed gently, and then spun at 14,000 xg for 15 minutes to remove cell debris. Supernatants were transferred into a fresh tube and frozen at -20 °C until further use.

Total protein samples were separated on a 4-12% SDS-PAGE (Genscript) and then transferred to PVDF membrane (BioRad) following standard procedures. Proteins were detected following manufacturer's instructions using the Amersham ECL Primer Western Blotting Detection Reagents (GE Healthcare) using primary antibody against GFP diluted 1:2,000 (Thermo Fischer, GF28R) and secondary antibody goat-antimouse diluted 1:5000. Blots were visualized on a Typhoon FLA 9500 scanner (GE Healthcare).

Table 6.5 Cloning, expression and purification of Dhr1 and Utp14 constructs for crystallography and biochemical assays

pSK Plasmid	Construct Name	Description
A100	Dhr1core	H14-SUMO-linker-Dhr1$_{379-1185}$
A175	Dhr1CTD	H14-SUMO-linker-Dhr1$_{379-1267}$
A216	Utp14DEF	H14-SUMO-Utp14$_{747 - 827}$
A210	Utp14D	H14-SUMO-linker-Utp14$_{747 – 780}$
A211	Utp14E	H14-SUMO-linker-Utp14$_{779 – 796}$
A212	Utp14F	H14-SUMO-linker-Utp14$_{797- 827}$
A208	Utp14DE	H14-SUMO-linker-Utp14$_{747-796}$
A215	Utp14EF	H14-SUMO-linker-Utp14 $_{779 – 827}$
A218	Dhr1CTD_Utp14D	H14-SUMO-linker-Dhr1$_{379-1267}$-linker-Utp14$_{747 – 780}$
A219	Dhr1CTD_Utp14DE	H14-SUMO-linker-Dhr1$_{379-1267}$-linker-Utp14$_{747-796}$
A220	Dhr1CTD_Utp14DEF	H14-SUMO-linker-Dhr1$_{379-1267}$-linker-Utp14$_{747 - 827}$
A225	Dhr1CTD_Utp14EF	H14-SUMO-linker-Dhr1$_{379-1267}$-linker-Utp14$_{779 – 827}$

Expression and Purification of Dhr1core for crystallization

Dhr1 (379-1185) was PCR amplified from *Saccharomyces cerevisiae* genomic DNA and cloned into an RSF-Duet1 vector containing an N-terminal His-14 SUMO tag (H14-SUMO) using BglII and XhoI restriction sites. This vector was transformed into RIL cells for expression. Large scale growth was done in 2x Yeast-Tryptone (2xYT) medium at 37 °C until an optical density (OD) of 1. At this point, expression was induced by the addition of 1 mM Isopropyl β-D-1-thiogalactopyranoside (IPTG) and growth was continued at 20 °C. Twenty hours after induction, cells were harvested by centrifugation at 8,000 x *g* and resuspended in buffer A (20 mM Tris/HCl pH 7.6, 500 mM NaCl, 0.1% Triton X-100) supplemented with protease inhibitors (E64, Pepstatin, and PMSF) and DNase/RNase. Cells were lysed at 4 °C by passing the cell suspension once through a Constant Systems cell disruptor at 30 kPSI. Lysates were centrifuged at 40,000 x *g* for 45 minutes, and clarified lysates were applied to a His-Trap HP column (GE Lifesciences). The column was washed with wash buffer (20 mM Tris/HCl pH 7.6, 30 mM imidazole, 500 mM NaCl) and then cleaved on-column with SUMO protease buffer (20 mM Tris/HCl pH 7.6, 500

mM NaCl and 15 µg/mL SUMO protease). Elutions were diluted to 125 mM NaCl with 20 mM Tris/HCl pH 7.6 and then loaded onto a HiTrap Heparin HP column (GE Lifesciences). The Heparin column was washed with two column volumes of 20 mM Tris/HCl pH 7.6 and 100 mM NaCl before being eluted with a salt gradient from 20 mM Tris/HCl pH 7.6, 100 mM NaCl to 20 mM Tris/HCl pH 7.6, 1 M NaCl. Fractions containing Dhr1 were pooled and concentrated before size exclusion chromatography on a HiLoad 16/600 Superdex 200 equilibrated with 20 mM Tris/HCl pH 7.6, 250 mM NaCl. Size exclusion fractions were concentrated to 8 mg/ml using a 30 kDa molecular weight cut-off Macrosep Advance centrifugal device (Pall Corporation).

Crystallization of Dhr1core

Purified Dhr1core at 8 mg/mL was supplemented with 1 mM adenosine 5'-diphosphate monopotassium salt and 1 mM magnesium chloride. Crystals were grown using the sitting drop vapor-diffusion method where 1 µL of Dhr1 was mixed with 2 µL well solution containing 10.5% PEG 6000 and 0.1 M HEPES pH 7.0 at 4 °C. Crystals were cryo-protected with a mix of 75% well solution and 25% PEG 400 before flash freezing in liquid nitrogen.

X-Ray Data Collection and Structure Determination for Dhr1 core

X-ray data was collected from beam line 24-ID-E of the Advanced Photon Source and Argonne National Laboratories (Chicago, IL) at a wavelength of 0.97919 Å. The Dhr1core crystal was solved using molecular replacement with Prp43 subdomains (PDB 2XAU) as search models using PHENIX. The Dhr1CTD_Utp14D crystal was solved using molecular replacement with the Dhr1core structure.

Expression and Purification of Dhr1 and Utp14 constructs for crystallographic studies and biochemical assays

Various constructs of Dhr1 and Utp14 (Table 6.5) were PCR amplified from *Saccharomyces cerevisiae* genomic DNA and cloned into an RSF-Duet1 vector containing an N-terminal His-14 SUMO tag (H14-SUMO). These vectors were transformed into RIL cells for expression. Large-scale growth was done in 2xYT medium at 37 °C until OD 0.6-0.8. At this point, expression was induced by the addition of 0.5 mM IPTG and growth was continued at 18 °C. Twenty hours after induction, cells were harvested by centrifugation at 4,000 x *g* and resuspended in buffer A (20 mM Tris/HCl pH 7.6, 500 mM NaCl, 0.1% Triton) supplemented with protease inhibitors (E64, Pepstatin, and PMSF) and DNase. Cells were flash frozen and stored at -80 °C until the time of protein purification. Cells were lysed at 4 °C by passing the resuspended cells once through a Constant Systems cell disruptor at 30 kPSI. Lysates were centrifuged at 40,000 x *g* for 30 minutes, and clarified lysates were applied to loose IMAC silica resin. Lysate was left to mix with resin at 4 °C while nutating for at least three hours. Beads were washed with 100 mL of buffer A, followed by 100 mLs of buffer B (20 mM Tris/HCl pH 7.6, 500 mM NaCl). The preparation of the proteins differs from this point for Dhr1 and Utp14 constructs and continues in the following sections.

Dhr1 and Dhr1CTD_Utp14 fusions purification continued

Elutions were diluted to 125 mM NaCl with 20 mM Tris/HCl pH 7.6 and then loaded onto a HiTrap Heparin HP column (GE Lifesciences). The Heparin column was washed with two

column volumes of 20 mM Tris/HCl pH 7.6 and 100 mM NaCl before being eluted with a salt gradient from 20 mM Tris/HCl pH 7.6, 100 mM NaCl to 20 mM Tris/HCl pH 7.6, 1 M NaCl. Fractions containing Dhr1 were pooled and concentrated before size exclusion chromatography on a HiLoad 16/600 Superdex 200 equilibrated with 20 mM Tris/HCl pH 7.6, 250 mM NaCl. Size exclusion fractions were concentrated to 8 mg/ml using a 30 kDa molecular weight cut-off Macrosep Advance centrifugal device (Pall Corporation).

Utp14 constructs purifications continued

Thoroughly washed beads were transferred to drip columns where protein was eluted with Buffer B supplemented with 300 mM imidazole buffer. Elutions were pooled, and salt levels were lowered to 250 mM by dilution with 20 mM Tris/HCl pH 7.6 and then loaded onto a HiTrap Heparin HP column (GE Lifesciences). The Heparin column was washed with two column volumes of 20 mM Tris/HCl pH 7.6 and 100 mM NaCl before being eluted with a salt gradient from 20 mM Tris/HCl pH 7.6, 100 mM NaCl to 20 mM Tris/HCl pH 7.6, 1 M NaCl. Fractions containing Utp14 were pooled and concentrated before size exclusion chromatography. Only Utp14 constructs containing segment F bound to the Heparin column at these salt levels. In the case of constructs that did not associate with Heparin, elutions from affinity beads were concentrated before size exclusion.

Size exclusion was performed on a Superose 6 (all Utp14 constructs except Utp14D) or a Superdex 75 (Utp14D) (GE Healthcare) with 20 mM Tris/HCl pH 7.6, 250 mM NaCl and 1 mM TCEP. Size exclusion fractions were concentrated from 5-8 mg/mL using a 10 kDa molecular weight cut-off Macrosep Advance centrifugal device (Pall Corporation). Utp14 constructs lacking aromatic residues had their concentrations quantified using Bradford assay (BioRad) and gel quantification.

Crystallization of Dhr1CTD_Utp14D

Purified Dhr1CTD_Utp14D at final concentration 6.6mg/mL was supplemented with 1 mM adenosine 5’-diphosphate monopotassium salt and 1 mM magnesium chloride. Crystals were grown using the sitting drop vapor-diffusion method where 0.3 µL of Dhr1 was mixed with 0.6 µL well solution containing 0.1 M Hepes pH 6.5 and 10% PEG 6K (final pH 7) at 19 °C. Crystals were cryo-protected with a mix of 75% well solution and 25% ethylene glycol before flash freezing in liquid nitrogen.

X-Ray Data Collection and Structure Determination for Dhr1CTD_Utp14D

X-ray data was collected from beam line 24-ID-E of the Advanced Photon Source and Argonne National Laboratories (Chicago, IL) at a wavelength of 0.97919 Å. The Dhr1core crystal was solved using molecular replacement with Prp43 subdomains (PDB 2XAU) as search models using PHENIX (Adams et al., 2010). The Dhr1CTD_Utp14D crystal was solved using molecular replacement with the Dhr1core structure.

Model building, refinement, visualization, and sequence alignments

Model building was performed with COOT (Emsley & Cowtan, 2004) and the structure was refined using PHENIX (Adams et al., 2010).

Dhr1core was refined to a R_{work}/R_{free} of 17.9/22.7 and good geometry (96.35% Ramachandran favored, 0.13% Ramachandran outliers). Dhr1CTD_Utp14D is not yet done being built so final refinement statistics have not yet been calculated.

All illustrations were made using PyMOL Molecular Graphics System, Version 2.1 Schrödinger, LLC. Sequence alignments were performed using Clustal Omega (Madeira et al., 2019). Secondary structure predictions were performed using Jpred 4 (Drozdetskiy, Cole, Procter, & Barton, 2015).

RNA Strand Displacement Assays

To assess Dhr1 activity, a RNA strand displacement assay was developed. Sequences of RNA strands utilized are described in Table 6.5. RNA was ordered from IDT with RNAse-free HPLC treatment.

RNA oligos were diluted to 1 millimolar concentration in DEPC-treated ddH_2O, and then subsequently diluted to 100 micromolar concentration in DEPC H_2O, aliquoted, flash frozen in liquid nitrogen, and stored at -80 °C.

Double stranded RNA substrate (ds substrate) was annealed fresh for every assay. Ds substrate was annealed in 10 µL reaction in a PCR tube: 1.55 µL of 100 µM unlabeled strand, 1.25 of 100 µM labeled strand, 5 µL of 2x annealing buffer (20 mM Tris pH 7.6, 2 mM EDTA, 200 mM NaCl), and 2.2 µL DEPC H_2O. Annealing reactions were placed in a pre-heated PCR machine (BioRad) starting at 95℃ and lowering to 4℃ over 90 minutes. The ds substrate was then diluted by taking 5 µL of the annealing reaction and mixing it with 2.5 µL of DEPC H_2O and 2.5 µL of annealing buffer. This should yield ds substrate at a concentration of about 6.25 µM.

A single RNA strand displacement reaction is 20 µL and contains final concentration: 8 µM Dhr1 construct, optional 8 µM Utp14 construct, 1.25 nM ds substrate, 20 units (1 µL) of SuperRNasin (Invitrogen), 65 mM NaCl, 0.5 mM $MgCl_2$, 2 mM ATP, and 0.25 mM TCEP. Reactions were stopped by the addition of 5 µL of loading dye (20 mM EDTA, 50% sucrose, bromophenol blue dye), and then placed on ice until gel loading. Reactions were visualized on non-denaturing 20% TBE gels (Novex) in 1X TBE buffer. Gels were run in the cold room at 100V for 180 minutes, in an ice bucket and on a stir plate to ensure buffer circulation. Gels were imaged using a Typhoon 9400 variable-mode imager (GE Healthcare). Band intensities were quantified using ImageJ. Percent of single stranded substrate released was calculated by:

(single stranded signal/ (single stranded signal + ds substrate signal) x 100%)

These values were analyzed using Prism 9 Software and nonlinear regression with the one phase exponential association (Y=Ymax*(1-exp(-K*X))).

Table 6.6 Sequence for RNA and DNA oligos utilized in the RNA strand displacement assay

Labeled 15-mer	5’ Alexa488-GCU UUA CGG UGC UAG 3’
Unlabeled strand, 3’ and 5’ overhang (45-mer)	5’ CUU UUC UUU UCU UUU CUU UUC UAG CAC CGU AAA GCU CUU UUC UUU 3’
DNA trap oligo	5’ GCT TTA CGG TGC TAG 3’

Chapter 7: Appendix

Table 7.1 Cryo-EM data collection parameters and refinement and validation statistics for the nucleolar pre-60S.

	core	state 2 EMD-7324 PDB 6C0F	state 2A	state 3 EMD-7445 PDB 6CB1
Data collection and processing				
Magnification	22,500X			
Voltage (kV)	300			
Pixel size (Å)	1.3			
Electron exposure (e- / Å^2)	47			
Defocus range (um)	1.0-3.5			
Symmetry imposed	C1			
Initial particle images	1,653,290			
Final particle images	514,746	201,114	75,512	31,419
Resolution (Å)	3.4	3.7	4.2	4.6
FSC threshold	0.143			
Map sharpening B-Factor (Å^2)	-68.7	-71.7	-83.0	-94.2
Refinement				
Model composition				
Non hydrogen atoms		91,741		69,945
Protein residues		7197		6347
RNA bases		1602		1615
Ligands		3		2
R.m.s. deviations				
Bond length (Å)		0.007		0.006
Angles (°)		1.11		1.10
Validation				
MolProbity score		1.91		1.68
Clashscore		10.67		5.96
Rotamer outliers (%)		0.30		0.13
Good sugar puckers (%)		98		97
Ramachandran				
Favored (%)		94.75		94.85
Allowed (%)		5.18		5.02
Outliers (%)		0.07		0.13

Table 7.2 Molecular models of the nucleolar pre-60S. Individual protein chains are listed with their initial PDB template (or built *de novo*) and the nucleolar pre-60S particle state(s) in which they are present.

Subgroup	Chain ID	SegID	Molecule name	Total residues or bases	Modelled (residue range)	Initial PDB template	Present in…
RNA	1	L1	25S	3,396	atomic (1,676 bases)	3JCT	All states
	2	L2	5.8S	158	atomic (158 bases)	3JCT	All states
	6	L6	ITS2	232	atomic (87 bases)	3JCT	All states
Ribosomal proteins	C	LC	Rpl4A_uL4	362	atomic (2-56, 89-347)	3JCT	All states
	E	LE	Rpl6A_eL6	176	atomic (7-176)	3JCT	All states
	e	SE	Rpl32_eL32	130	atomic (7-36, 47-130)	3JCT	All states
	F	LF	Rpl7A_uL30	244	atomic (3-244)	3JCT	All states
	f	SF	Rpl33A_eL33	107	atomic (2-107)	3JCT	All states
	G	LG	Rpl8A_eL8	256	atomic (53-239)	3JCT	All states
	h	SH	Rpl35A_uL29	120	atomic (2-120)	3JCT	All states
	i	SI	Rpl36A_eL36	100	atomic (17-100)	3JCT	All states
	L	LL	Rpl13A_eL13	199	atomic (22-127)	3JCT	All states
	M	LM	Rpl14A_eL14	138	atomic (11-138)	3JCT	All states
	N	LN	Rpl15A_eL15	204	atomic (2-68, 96-204)	3JCT	All states
	O	LO	Rpl16A_uL13	199	atomic (3-59, 73-199)	3JCT	All states
	Q	LQ	Rpl18A_eL18	186	atomic (15-146)	4v88, chain BQ	All states
	S	LS	Rpl20A_eL20	172	atomic (2-172)	3JCT	All states
	B	LB	Rpl3_uL3	387	atomic (17-224, 270-385)	4v88, chain DB	State 2
	P	LP	Rpl17A_uL22	184	atomic (10-64, 80-126, 140-161)	3JCT	All states
	V	LV	Rpl23A_uL14	137	atomic (16-137)	3JCT	State 2
	Y	LY	Rpl26A_uL24	127	atomic (2-127)	3JCT	All states
	j	SJ	Rpl37A_eL37	88	atomic (14-85, Zn)	3JCT	All states
	Z	LZ	Rpl27A_eL27	136	side-chain trimmed (2-136)	3JCT	State 3
	k	SK	Rpl38_eL38	78	side-chain trimmed (2-78)	3JCT	State 3
	g	SG	Rpl34A_eL34	121	side-chain trimmed (2-102)	3JCT	State 3
	c	SC	Rpl30_eL30	105	side-chain trimmed (9-105)	3JCT	State 3
	X	LX	Rpl25_uL23	142	side-chain trimmed (2-142)	3JCT	State 3
Assembly factors common to Nog2 particle (3JCT)	K	LK	Cic1	376	atomic (31-51, 64-302)	3JCT	All states
	n	SN	Nop7	605	atomic (13-43, 61-267, 351-396, 404-460)	3JCT	All states
	o	SO	Nop15	220	atomic (88-220)	3JCT	All states
	t	ST	Rlp7	322	atomic (54-105, 127-322)	3JCT	All states
	t	ST	Rlp7 (NTD)	322	poly-alanine (20-53)	De novo	State 3
	u	SU	Rlp24	199	atomic (2-130, Zn)	3JCT	State 2
	y	SY	Tif6	245	atomic (1-226)	3JCT	State 2
	W	LW	Nog1	647	atomic (373-470)	3JCT	State 2
New assembly factors	A	LA	Nsa1	463	atomic (1-78, 101-416)	5SUI	All states
	p	SP	Has1	505	atomic (42-252, 264-489)	Phyre model based on 2V1X	All states
	b	SB	Brx1	291	atomic (31-122, 132-164, 174-192, 211-290), poly-alanine (123-131, 165-173)	Model based on 5WLC, chain SM	All states
	m	SM	Ebp2	427	poly-alanine (196-269)	De novo	All states
	z	SZ	Rrp1	278	atomic (1-186, 197-253)	De novo	All states
	D	LD	Mak16	306	atomic (2-191, Zn)	De novo	All states
	I	LI	Rpf1	295	atomic (8-295)	Phyre model based on 5JPQ, chain c	All states
	s	SS	Erb1-NTD	807	atomic (239-298, 372-395), poly-alanine (299-371)	De novo	All states
	s	SS	Erb1-CTD	807	side-chain trimmed crystal structure (416-426, 428-534, 571-807)	4U7A	State 3
	v	SV	Ssf1	453	atomic (23-214, 324-356)	Phyre model based on 4XV9	State 2
	q	SQ	Mak11	468	poly-alanine (WD40, 285 residues)	Phyre model based on 3DM0	States 2 and 2A
	w	SW	Rrp15	250	atomic (174-243)	De novo	State 2
	d	SD	Ytm1	460	poly-alanine (*C. thermophilum*, 465 residues)	5CXB	State 3
	7	S7	Nop16	231	atomic (1-83, 156-228)	De novo	All states
	8	S8	Rrp14	434	atomic (296-393)	De novo	State 2
	x	SX	Brx1-associated peptide	unknown	poly-alanine (162-189)	De novo	All states

Table 7.3 Refinement statistics for the auto inhibited Dhr1 core bound to ADP.

	Dhr1 core
PDB entry	7MQJ
Crystal form	$P2_1$
Unit cell dimensions	
a, *b*, *c* (Å)	41.77, 130.94, 86.08
α, β, γ (°)	90.00, 106.483, 90.00
Data collection	
Wavelength (Å)	0.97919
Resolution (Å)	38.58-2.23 (2.31-2.23)*
Unique reflections	42918 (4275)
R_{meas} (%)	9.7 (61.9)
$CC_{1/2}$	99.7 (78.4)
Completeness (%)	99.34 (98.68)
$I / \sigma I$	11.89 (2.11)
Multiplicity	3.4 (3.3)
Model statistics	
Model composition	
No. atoms	
Protein	6303
Ligand/ion	28
Water	284
Refinement	
Resolution (Å)	38.58-2.23
No. reflections	42910
R_{work} / R_{free}	0.1794/0.2275
B-factors	
Protein	51.2
Ligand/ion	50.1
Water	43.5
R.m.s. deviations:	
Bond lengths (Å)	0.0082
Bond angles (°)	0.96
Ramachandran plot:	
favored (%)	96.35
allowed (%)	3.52
outliers (%)	0.28
Clashscore	6

*Values in parentheses are for highest-resolution shell.

Table 7.4 Refinement statistics for auto-inhibited Dhr1CTD at the time of writing. Building and refinement is not yet complete for this structure.

	Dhr1 core
PDB entry	XXXX
Crystal form	
Unit cell dimensions	
a, *b*, *c* (Å)	57.89, 69.73, 236
α, β, γ (°)	90, 90, 90
Data collection	
Wavelength (Å)	0.97919
Resolution (Å)	59 - 2.403 (2.489 - 2.403)
Unique reflections	38184 (3673)
R_{meas} (%)	0.1253 (0.3879)
$CC_{1/2}$	0.995 (0.959)
Completeness (%)	99.57 (97.64)
$I / \sigma I$	25.24 (7.69)
Multiplicity	6.7 (6.7)
Model statistics	
Model composition	
No. atoms	
Protein	6662
Ligand/ion	26
Water	187
Refinement	
Resolution (Å)	59 - 2.403
No. reflections	38043 (3648)
R_{work} / R_{free}	0.2123/0.2468
B-factors	
Protein	56.76
Ligand/ion	64.24
Water	51.95
R.m.s. deviations:	
Bond lengths (Å)	0.007
Bond angles (°)	0.85
Ramachandran plot:	
favored (%)	97.33
allowed (%)	2.55
outliers (%)	0.12
Clashscore	9

*Values in parentheses are for highest-resolution shell.

Table 7.5 Mass spectrometry results from purified Urb particles and purified Urb subcomplexes. Urb subcomplex proteins are bolded in black. Box C/D snoRNA proteins are in green. Ribosomal proteins are in blue. Other assembly factors are in purple. *YCR016W is a nucleolar protein of unknown function.

Urb particle

Protein	Area
Nop1	2.973E10
Snu13	2.369E10
Nop56	1.612E10
Cbf5	1.467E10
Smt3	1.262E10
Nop58	1.253E10
Rrp5	1.247E10
Nhp2	1.151E10
L7A	1.016E10
L7B	1.016E10
Rsa3	9.578E9
L8A	8.991E9
L8B	8.991E9
Nop8	8.957E9
Urb1	8.941E9
Gar1	8.413E9
Nop10	8.049E9
Rlp7	8.043E9
Nop7	7.906E9
Mak21	7.741E9
L13B	7.332E9
Nop4	7.020E9
Nop12	6.684E9
cic1	6.682E9
L27	6.398E9
L32	6.393E9

Urb particle cont.

Erb1	6.036E9
L4A	5.793E9
L4B	5.793E9
Ytm1	5.791E9
YCR016W	5.675E9
Rex4	5.665E9
Noc2	5.642E9
Urb2	5.639E9
L6A	5.450E9
L6B	5.450E9
Dbp6	5.017E9
L15A	4.994E9
L15B	4.994E9
Ebp2	4.937E9
L36A	4.831E9
L36B	4.831E9
Has1	4.730E9
L3	4.635E9
L14A	4.633E9
L14B	4.633E9
L24B	4.552E9
Srp40	4.428E9
L16B	4.418E9
L16A	4.418E9
L24A	4.397E9

Urb subcomplex

Protein	Area
Rsa3	4.521E10
Urb1	2.737E10
Urb2	2.418E10
Nop8	2.145E10
Snu13	1.505E10
Dbp6	1.371E10
Nop1	1.205E10
Nop56	6.789E9
Nop58	6.518E9
Pma1	3.743E9
Pma2	3.743E9
L8A	1.701E9
L8B	1.701E9
L13B	6.871E8
Rna14	6.650E8
Tdh2	5.543E8
Tdh3	5.543E8
Tdh1	5.543E8
L19A	5.458E8
Mrh1	4.950E8

Chapter 8: References

Adams, P. D., Afonine, P. V., Bunkóczi, G., Chen, V. B., Davis, I. W., Echols, N., et al. (2010). PHENIX: a comprehensive Python-based system for macromolecular structure solution. *Acta Crystallographica. Section D, Biological Crystallography*, *66*(Pt 2), 213–221. http://doi.org/10.1107/S0907444909052925

Albert, B., Knight, B., Merwin, J., Martin, V., Ottoz, D., Gloor, Y., et al. (2016). A Molecular Titration System Coordinates Ribosomal Protein Gene Transcription with Ribosomal RNA Synthesis. *Molecular Cell*, *64*(4), 720–733. http://doi.org/10.1016/j.molcel.2016.10.003

Allmang, C., Kufel, J., Chanfreau, G., Mitchell, P., Petfalski, E., & Tollervey, D. (1999). Functions of the exosome in rRNA, snoRNA and snRNA synthesis. *The EMBO Journal*, *18*(19), 5399–5410. http://doi.org/10.1093/emboj/18.19.5399

Allmang, C., Mitchell, P., Petfalski, E., & Tollervey, D. (2000). Degradation of ribosomal RNA precursors by the exosome. *Nucleic Acids Research*, *28*(8), 1684–1691. http://doi.org/10.1093/nar/28.8.1684

Andersen, C. B. F., Ballut, L., Johansen, J. S., Chamieh, H., Nielsen, K. H., Oliveira, C. L. P., et al. (2006). Structure of the exon junction core complex with a trapped DEAD-box ATPase bound to RNA. *Science (New York, N.Y.)*, *313*(5795), 1968–1972. http://doi.org/10.1126/science.1131981

Arenas, J. E., & Abelson, J. N. (1997). Prp43: An RNA helicase-like factor involved in spliceosome disassembly. *Proceedings of the National Academy of Sciences*, *94*(22), 11798–11802. http://doi.org/10.1073/pnas.94.22.11798

Bai, R., Wan, R., Yan, C., Jia, Q., Lei, J., & Shi, Y. (2021). Mechanism of spliceosome remodeling by the ATPase/helicase Prp2 and its coactivator Spp2. *Science (New York, N.Y.)*, *371*(6525). http://doi.org/10.1126/science.abe8863

Ballut, L., Marchadier, B., Baguet, A., Tomasetto, C., Séraphin, B., & Le Hir, H. (2005). The exon junction core complex is locked onto RNA by inhibition of eIF4AIII ATPase activity. *Nature Structural & Molecular Biology*, *12*(10), 861–869. http://doi.org/10.1038/nsmb990

Ban, N., Nissen, P., Hansen, J., Moore, P. B., & Steitz, T. A. (2000). The complete atomic structure of the large ribosomal subunit at 2.4 A resolution. *Science (New York, N.Y.)*, *289*(5481), 905–920. http://doi.org/10.1126/science.289.5481.905

Barandun, J., Chaker-Margot, M., Hunziker, M., Molloy, K. R., Chait, B. T., & Klinge, S. (2017). The complete structure of the small-subunit processome. *Nature Structural & Molecular Biology*, *24*(11), 944–953. http://doi.org/10.1038/nsmb.3472

Baßler, J., Kallas, M., Pertschy, B., Ulbrich, C., Thoms, M., & Hurt, E. (2010). The AAA-ATPase Rea1 drives removal of biogenesis factors during multiple stages of 60S ribosome assembly. *Molecular Cell*, *38*(5), 712–721. http://doi.org/10.1016/j.molcel.2010.05.024

Ben-Shem, A., Garreau de Loubresse, N., Melnikov, S., Jenner, L., Yusupova, G., & Yusupov, M. (2011). The structure of the eukaryotic ribosome at 3.0 Å resolution. *Science (New York, N.Y.)*, *334*(6062), 1524–1529. http://doi.org/10.1126/science.1212642

Bernstein, K. A., Granneman, S., Lee, A. V., Manickam, S., & Baserga, S. J. (2006). Comprehensive mutational analysis of yeast DEXD/H box RNA helicases involved in large ribosomal subunit biogenesis. *Molecular and Cellular Biology*, *26*(4), 1195–1208. http://doi.org/10.1128/MCB.26.4.1195-1208.2006

Bleichert, F., Granneman, S., Osheim, Y. N., Beyer, A. L., & Baserga, S. J. (2006). The PINc domain protein Utp24, a putative nuclease, is required for the early cleavage steps in 18S rRNA maturation. *Proceedings of the National Academy of Sciences*, *103*(25), 9464–9469. http://doi.org/10.1073/pnas.0603673103

Bohnsack, K. E., Ficner, R., Bohnsack, M. T., & Jonas, S. (2021). Regulation of DEAH-box RNA helicases by G-patch proteins. *Biological Chemistry*, *402*(5), 561–579. http://doi.org/10.1515/hsz-2020-0338

Bohnsack, M. T., Martin, R., Granneman, S., Ruprecht, M., Schleiff, E., & Tollervey, D. (2009). Prp43 bound at different sites on the pre-rRNA performs distinct functions in ribosome synthesis. *Molecular Cell*, *36*(4), 583–592. http://doi.org/10.1016/j.molcel.2009.09.039

Bond, A. T., Mangus, D. A., He, F., & Jacobson, A. (2001). Absence of Dbp2p alters both nonsense-mediated mRNA decay and rRNA processing. *Molecular and Cellular Biology*, *21*(21), 7366–7379. http://doi.org/10.1128/MCB.21.21.7366-7379.2001

Boneberg, F. M., Brandmann, T., Kobel, L., van den Heuvel, J., Bargsten, K., Bammert, L., et al. (2019). Molecular mechanism of the RNA helicase DHX37 and its activation by UTP14A in ribosome biogenesis. *Rna*, *25*(6), 685–701. http://doi.org/10.1261/rna.069609.118

Bono, F., Ebert, J., Lorentzen, E., & Conti, E. (2006). The crystal structure of the exon junction complex reveals how it maintains a stable grip on mRNA. *Cell*, *126*(4), 713–725. http://doi.org/10.1016/j.cell.2006.08.006

Bradatsch, B., Leidig, C., Granneman, S., Gnädig, M., Tollervey, D., Böttcher, B., et al. (2012). Structure of the pre-60S ribosomal subunit with nuclear export factor Arx1 bound at the exit tunnel. *Nature Structural & Molecular Biology*, *19*(12), 1234–1241. http://doi.org/10.1038/nsmb.2438

Briggs, M. W., Burkard, K. T., & Butler, J. S. (1998). Rrp6p, the yeast homologue of the human PM-Scl 100-kDa autoantigen, is essential for efficient 5.8 S rRNA 3' end formation. *The Journal of Biological Chemistry*, *273*(21), 13255–13263. http://doi.org/10.1074/jbc.273.21.13255

Brüning, L., Hackert, P., Martin, R., Gallesio, J. D., Aquino, G. R. R., Urlaub, H., et al. (2018). RNA helicases mediate structural transitions and compositional changes in pre-ribosomal complexes. *Nature Communications*, 1–14. http://doi.org/10.1038/s41467-018-07783-w

Burger, F., Daugeron, M. C., & Linder, P. (2000). Dbp10p, a putative RNA helicase from Saccharomyces cerevisiae, is required for ribosome biogenesis. *Nucleic Acids Research*, *28*(12), 2315–2323. http://doi.org/10.1093/nar/28.12.2315

Castle, C. D., Sardana, R., Dandekar, V., Borgianini, V., Johnson, A. W., & Denicourt, C. (2013). Las1 interacts with Grc3 polynucleotide kinase and is required for ribosome synthesis in Saccharomyces cerevisiae. *Nucleic Acids Research*, *41*(2), 1135–1150. http://doi.org/10.1093/nar/gks1086

Chaker-Margot, M., & Klinge, S. (2019). Assembly and early maturation of large subunit precursors. *Rna*, *25*(4), 465–471. http://doi.org/10.1261/rna.069799.118

Chaker-Margot, M., Barandun, J., Hunziker, M., & Klinge, S. (2017). Architecture of the yeast small subunit processome. *Science (New York, N.Y.)*, *355*(6321), eaal1880. http://doi.org/10.1126/science.aal1880

Chaker-Margot, M., Hunziker, M., Barandun, J., Dill, B. D., & Klinge, S. (2015). Stage-specific assembly events of the 6-MDa small-subunit processome initiate eukaryotic ribosome biogenesis. *Nature Structural & Molecular Biology*, *22*(11), 920–923. http://doi.org/10.1038/nsmb.3111

Cheng, J., Kellner, N., Berninghausen, O., Hurt, E., & Beckmann, R. (2017). 3.2-Å-resolution structure of the 90S preribosome before A1 pre-rRNA cleavage. *Nature Structural & Molecular Biology*, *24*(11), 954–964. http://doi.org/10.1038/nsmb.3476

Cheng, J., Lau, B., La Venuta, G., Ameismeier, M., Berninghausen, O., Hurt, E., & Beckmann, R. (2020). 90S pre-ribosome transformation into the primordial 40S subunit. *Science*, *369*(6510), 1470–1476. http://doi.org/10.1126/science.abb4119

Choudhury, P., Hackert, P., Memet, I., Sloan, K. E., & Bohnsack, M. T. (2019). The human RNA helicase DHX37 is required for release of the U3 snoRNP from pre-ribosomal particles. *RNA Biology*, *16*(1), 54–68. http://doi.org/10.1080/15476286.2018.1556149

Clemons, W. M., May, J. L., Wimberly, B. T., McCutcheon, J. P., Capel, M. S., & Ramakrishnan, V. (1999). Structure of a bacterial 30S ribosomal subunit at 5.5 A resolution. *Nature*, *400*(6747), 833–840. http://doi.org/10.1038/23631

Colley, A., Beggs, J. D., Tollervey, D., & Lafontaine, D. L. (2000). Dhr1p, a putative DEAH-box RNA helicase, is associated with the box C+D snoRNP U3. *Molecular and Cellular Biology*, *20*(19), 7238–7246.

Collins, R., Karlberg, T., Lehtiö, L., Schütz, P., van den Berg, S., Dahlgren, L.-G., et al. (2009). The DEXD/H-box RNA helicase DDX19 is regulated by an {alpha}-helical switch. *The Journal of Biological Chemistry*, *284*(16), 10296–10300. http://doi.org/10.1074/jbc.C900018200

Combs, D. J., Nagel, R. J., Ares, M., & Stevens, S. W. (2006). Prp43p is a DEAH-box spliceosome disassembly factor essential for ribosome biogenesis. *Molecular and Cellular Biology*, *26*(2), 523–534. http://doi.org/10.1128/MCB.26.2.523-534.2006

Crick, F. H. (1958). On protein synthesis. *Symposia of the Society for Experimental Biology*, *12*, 138–163.

Daugeron, M. C., & Linder, P. (1998). Dbp7p, a putative ATP-dependent RNA helicase from Saccharomyces cerevisiae, is required for 60S ribosomal subunit assembly. *Rna*, *4*(5), 566–581. http://doi.org/10.1017/s1355838298980190

Daugeron, M. C., & Linder, P. (2001). Characterization and mutational analysis of yeast Dbp8p, a putative RNA helicase involved in ribosome biogenesis. *Nucleic Acids Research*, *29*(5), 1144–1155. http://doi.org/10.1093/nar/29.5.1144

Daugeron, M. C., Kressler, D., & Linder, P. (2001). Dbp9p, a putative ATP-dependent RNA helicase involved in 60S-ribosomal-subunit biogenesis, functionally interacts with Dbp6p. *Rna*, *7*(9), 1317–1334. http://doi.org/10.1017/s1355838201010640

Davis, J. H., Tan, Y. Z., Carragher, B., Potter, C. S., Lyumkis, D., & Williamson, J. R. (2016). Modular Assembly of the Bacterial Large Ribosomal Subunit. *Cell*, *167*(6), 1610–1622.e15. http://doi.org/10.1016/j.cell.2016.11.020

Del Campo, M., & Lambowitz, A. M. (2009). Structure of the Yeast DEAD box protein Mss116p reveals two wedges that crimp RNA. *Molecular Cell*, *35*(5), 598–609. http://doi.org/10.1016/j.molcel.2009.07.032

Dembowski, J. A., Kuo, B., & Woolford, J. L. (2013). Has1 regulates consecutive maturation and processing steps for assembly of 60S ribosomal subunits. *Nucleic Acids Research*, *41*(16), 7889–7904. http://doi.org/10.1093/nar/gkt545

Demoinet, E., Jacquier, A., Lutfalla, G., & Fromont-Racine, M. (2007). The Hsp40 chaperone Jjj1 is required for the nucleo-cytoplasmic recycling of preribosomal factors in Saccharomyces cerevisiae. *Rna*, *13*(9), 1570–1581. http://doi.org/10.1261/rna.585007

Dever, T. E., Kinzy, T. G., & Pavitt, G. D. (2016). Mechanism and Regulation of Protein Synthesis in Saccharomyces cerevisiae. *Genetics*, *203*(1), 65–107. http://doi.org/10.1534/genetics.115.186221

Dez, C., Froment, C., Noaillac-Depeyre, J., Monsarrat, B., Caizergues-Ferrer, M., & Henry, Y. (2004). Npa1p, a Component of Very Early Pre-60S Ribosomal Particles, Associates with a Subset of Small Nucleolar RNPs Required for Peptidyl Transferase Center Modification. *Molecular and Cellular Biology*, *24*(14), 6324–6337.

Dragon, F., Gallagher, J. E. G., Compagnone-Post, P. A., Mitchell, B. M., Porwancher, K. A., Wehner, K. A., et al. (2002). A large nucleolar U3 ribonucleoprotein required for 18S ribosomal RNA biogenesis. *Nature*, *417*(6892), 967–970. http://doi.org/10.1038/nature00769

Drozdetskiy, A., Cole, C., Procter, J., & Barton, G. J. (2015). JPred4: a protein secondary structure prediction server. *Nucleic Acids Research*, *43*(W1), W389–94. http://doi.org/10.1093/nar/gkv332

Du, Y., An, W., Zhu, X., Sun, Q., Qi, J., & Ye, K. (2020). Cryo-EM structure of 90S small ribosomal subunit precursors in transition states. *Science (New York, N.Y.)*, *369*(6510), 1477–1481. http://doi.org/10.1126/science.aba9690

Emery, B., la Cruz, de, J., Rocak, S., Deloche, O., & Linder, P. (2004). Has1p, a member of the DEAD-box family, is required for 40S ribosomal subunit biogenesis in Saccharomyces cerevisiae. *Molecular Microbiology*, *52*(1), 141–158. http://doi.org/10.1111/j.1365-2958.2003.03973.x

Emsley, P., & Cowtan, K. (2004). Coot: model-building tools for molecular graphics. *Acta Crystallographica. Section D, Biological Crystallography*, *60*(Pt 12 Pt 1), 2126–2132. http://doi.org/10.1107/S0907444904019158

Fairman-Williams, M. E., Guenther, U.-P., & Jankowsky, E. (2010). SF1 and SF2 helicases: family matters. *Current Opinion in Structural Biology*, *20*(3), 313–324. http://doi.org/10.1016/j.sbi.2010.03.011

Feric, M., Vaidya, N., Harmon, T. S., Mitrea, D. M., Zhu, L., Richardson, T. M., et al. (2016). Coexisting Liquid Phases Underlie Nucleolar Subcompartments. *Cell*, *165*(7), 1686–1697. http://doi.org/10.1016/j.cell.2016.04.047

Fischer, U., Schäuble, N., Schütz, S., Altvater, M., Chang, Y., Faza, M. B., & Panse, V. G. (2015). A non-canonical mechanism for Crm1-export cargo complex assembly. *eLife*, *4*. http://doi.org/10.7554/eLife.05745

Fourmann, J.-B., Dybkov, O., Agafonov, D. E., Tauchert, M. J., Urlaub, H., Ficner, R., et al. (2016). The target of the DEAH-box NTP triphosphatase Prp43 in Saccharomyces cerevisiae spliceosomes is the U2 snRNP-intron interaction. *eLife*, *5*.

Fromm, L., Falk, S., Flemming, D., Schuller, J. M., Thoms, M., Conti, E., & Hurt, E. (2017). Reconstitution of the complete pathway of ITS2 processing at the pre-ribosome. *Nature Communications*, *8*(1), 1787–11. http://doi.org/10.1038/s41467-017-01786-9

Gasse, L., Flemming, D., & Hurt, E. (2015). Coordinated Ribosomal ITS2 RNA Processing by the Las1 Complex Integrating Endonuclease, Polynucleotide Kinase, and Exonuclease Activities. *Molecular Cell*, *60*(5), 808–815. http://doi.org/10.1016/j.molcel.2015.10.021

Gelperin, D., Horton, L., Beckman, J., Hensold, J., & Lemmon, S. K. (2001). Bms1p, a novel GTP-binding protein, and the related Tsr1p are required for distinct steps of 40S ribosome biogenesis in yeast. *Rna*, *7*(9), 1268–1283. http://doi.org/10.1017/s1355838201013073

Ghalei, H., Trepreau, J., Collins, J. C., Bhaskaran, H., Strunk, B. S., & Karbstein, K. (2017). The ATPase Fap7 Tests the Ability to Carry Out Translocation-like Conformational Changes and Releases Dim1 during 40S Ribosome Maturation. *Molecular Cell*, *67*(6), 990–1000.e3. http://doi.org/10.1016/j.molcel.2017.08.007

Gilman, B., Tijerina, P., & Russell, R. (2017). Distinct RNA-unwinding mechanisms of DEAD-box and DEAH-box RNA helicase proteins in remodeling structured RNAs and RNPs. *Biochemical Society Transactions*, *45*(6), 1313–1321. http://doi.org/10.1042/BST20170095

Gorbalenya, A. E., & Koonin, E. V. (1993). Helicases: amino acid sequence comparisons and structure-function relationships. *Current Opinion in Structural Biology*, *3*(3), 419–429.

Granneman, S., Petfalski, E., & Tollervey, D. (2011). A cluster of ribosome synthesis factors regulate pre-rRNA folding and 5.8S rRNA maturation by the Rat1 exonuclease. *The EMBO Journal*, *30*(19), 4006–4019. http://doi.org/10.1038/emboj.2011.256

Granneman, S., Petfalski, E., Swiatkowska, A., & Tollervey, D. (2010). Cracking pre-40S ribosomal subunit structure by systematic analyses of RNA-protein cross-linking. *The EMBO Journal*, *29*(12), 2026–2036. http://doi.org/10.1038/emboj.2010.86

Hamann, F., Schmitt, A., Favretto, F., Hofele, R., Neumann, P., Xiang, S., et al. (2020). Structural analysis of the intrinsically disordered splicing factor Spp2 and its binding to the DEAH-box ATPase Prp2. *Proceedings of the National Academy of Sciences of the United States of America*, *117*(6), 2948–2956. http://doi.org/10.1073/pnas.1907960117

Harnpicharnchai, P., Jakovljevic, J., Horsey, E., Miles, T., Roman, J., Rout, M., et al. (2001). Composition and functional characterization of yeast 66S ribosome assembly intermediates. *Molecular Cell*, *8*(3), 505–515.

Heuer, A., Thomson, E., Schmidt, C., Berninghausen, O., Becker, T., Hurt, E., & Beckmann, R. (2017). Cryo-EM structure of a late pre-40S ribosomal subunit from Saccharomyces cerevisiae. *eLife*, *6*. http://doi.org/10.7554/eLife.30189

Hierlmeier, T., Merl, J., Sauert, M., Perez-Fernandez, J., Schultz, P., Bruckmann, A., et al. (2013). Rrp5p, Noc1p and Noc2p form a protein module which is part of early large ribosomal subunit precursors in S. cerevisiae. *Nucleic Acids Research*, *41*(2), 1191–1210. http://doi.org/10.1093/nar/gks1056

Huang, H.-R., Rowe, C. E., Mohr, S., Jiang, Y., Lambowitz, A. M., & Perlman, P. S. (2005). The splicing of yeast mitochondrial group I and group II introns requires a DEAD-box protein with RNA chaperone function. *Proceedings of the National Academy of Sciences*, *102*(1), 163–168. http://doi.org/10.1073/pnas.0407896101

Hung, N.-J., & Johnson, A. W. (2006). Nuclear recycling of the pre-60S ribosomal subunit-associated factor Arx1 depends on Rei1 in Saccharomyces cerevisiae. *Molecular and Cellular Biology*, *26*(10), 3718–3727. http://doi.org/10.1128/MCB.26.10.3718-3727.2006

Hunziker, M., Barandun, J., Buzovetsky, O., Steckler, C., Molina, H., & Klinge, S. (2019). Conformational switches control early maturation of the eukaryotic small ribosomal subunit. *eLife*, *8*. http://doi.org/10.7554/eLife.45185

Iacovella, M. G., Golfieri, C., Massari, L. F., Busnelli, S., Pagliuca, C., Dal Maschio, M., et al. (2015). Rio1 promotes rDNA stability and downregulates RNA polymerase I to ensure rDNA segregation. *Nature Communications*, *6*(1), 6643–16. http://doi.org/10.1038/ncomms7643

Iost, I., Dreyfus, M., & Linder, P. (1999). Ded1p, a DEAD-box protein required for translation initiation in Saccharomyces cerevisiae, is an RNA helicase. *The Journal of Biological Chemistry*, *274*(25), 17677–17683. http://doi.org/10.1074/jbc.274.25.17677

Johnson, M. C., Ghalei, H., Doxtader, K. A., Karbstein, K., & Stroupe, M. E. (2017). Structural Heterogeneity in Pre-40S Ribosomes. *Structure (London, England : 1993)*, *25*(2), 329–340. http://doi.org/10.1016/j.str.2016.12.011

Johnson, S. J., & Jackson, R. N. (2013). Ski2-like RNA helicase structures: common themes and complex assemblies. *RNA Biology*, *10*(1), 33–43. http://doi.org/10.4161/rna.22101

Joret, C., Capeyrou, R., Belhabich-Baumas, K., Plisson-Chastang, C., Ghandour, R., Humbert, O., et al. (2018). The Npa1p complex chaperones the assembly of the earliest eukaryotic large ribosomal subunit precursor. *PLOS Genetics*, *14*(8), e1007597–30. http://doi.org/10.1371/journal.pgen.1007597

Kappel, L., Loibl, M., Zisser, G., Klein, I., Fruhmann, G., Gruber, C., et al. (2012). Rlp24 activates the AAA-ATPase Drg1 to initiate cytoplasmic pre-60S maturation. *The Journal of Cell Biology*, *199*(5), 771–782. http://doi.org/10.1083/jcb.201205021

Kargas, V., Castro-Hartmann, P., Escudero-Urquijo, N., Dent, K., Hilcenko, C., Sailer, C., et al. (2019). Mechanism of completion of peptidyltransferase centre assembly in eukaryotes. *eLife*, *8*. http://doi.org/10.7554/eLife.44904

Kater, L., Thoms, M., Barrio-Garcia, C., Cheng, J., Ismail, S., Ahmed, Y. L., et al. (2017). Visualizing the Assembly Pathway of Nucleolar Pre- 60S Ribosomes. *Cell*, *171*(7), 1599–1610.e13. http://doi.org/10.1016/j.cell.2017.11.039

Kelley, L. A., Mezulis, S., Yates, C. M., Wass, M. N., & Sternberg, M. J. E. (2015). The Phyre2 web portal for protein modeling, prediction and analysis. *Nature Protocols*, *10*(6), 845–858. http://doi.org/10.1038/nprot.2015.053

Khoshnevis, S., Askenasy, I., Johnson, M. C., Dattolo, M. D., Young-Erdos, C. L., Stroupe, M. E., & Karbstein, K. (2016). The DEAD-box Protein Rok1 Orchestrates 40S and 60S Ribosome Assembly by Promoting the Release of Rrp5 from Pre-40S Ribosomes to Allow for 60S Maturation. *PLoS Biology*, *14*(6), e1002480. http://doi.org/10.1371/journal.pbio.1002480

Kimanius, D., Forsberg, B. O., Scheres, S. H., & Lindahl, E. (2016). Accelerated cryo-EM structure determination with parallelisation using GPUs in RELION-2. *eLife*, *5*. http://doi.org/10.7554/eLife.18722

Klinge, S., Voigts-Hoffmann, F., Leibundgut, M., Arpagaus, S., & Ban, N. (2011). Crystal structure of the eukaryotic 60S ribosomal subunit in complex with initiation factor 6. *Science (New York, N.Y.)*, *334*(6058), 941–948. http://doi.org/10.1126/science.1211204

Konikkat, S., Biedka, S., & Woolford, J. L., Jr. (2017). The assembly factor Erb1 functions in multiple remodeling events during 60S ribosomal subunit assembly in S. cerevisiae. *Nucleic Acids Research*, gkw1361. http://doi.org/10.1093/nar/gkw1361

Kornprobst, M., Turk, M., Kellner, N., Cheng, J., Flemming, D., Koš-Braun, I., et al. (2016). Architecture of the 90S Pre-ribosome: A Structural View on the Birth of the Eukaryotic Ribosome. *Cell*, *166*(2), 380–393. http://doi.org/10.1016/j.cell.2016.06.014

Kos, M., & Tollervey, D. (2005). The Putative RNA Helicase Dbp4p Is Required for Release of the U14 snoRNA from Preribosomes in Saccharomyces cerevisiae. *Molecular Cell*, *20*(1), 53–64. http://doi.org/10.1016/j.molcel.2005.08.022

Kos, M., & Tollervey, D. (2010). Yeast pre-rRNA processing and modification occur cotranscriptionally. *Molecular Cell*, *37*(6), 809–820. http://doi.org/10.1016/j.molcel.2010.02.024

Kos-Braun, I. C., Jung, I., & Kos, M. (2017). Tor1 and CK2 kinases control a switch between alternative ribosome biogenesis pathways in a growth-dependent manner. *PLoS Biology*, *15*(3), e2000245. http://doi.org/10.1371/journal.pbio.2000245

Kressler, D., la Cruz, de, J., Rojo, M., & Linder, P. (1997). Fal1p is an essential DEAD-box protein involved in 40S-ribosomal-subunit biogenesis in Saccharomyces cerevisiae. *Molecular and Cellular Biology*, *17*(12), 7283–7294. http://doi.org/10.1128/mcb.17.12.7283

Kressler, D., la Cruz, de, J., Rojo, M., & Linder, P. (1998). Dbp6p Is an Essential Putative ATP-Dependent RNA Helicase Required for 60S-Ribosomal-Subunit Assembly in Saccharomyces cerevisiae. *Molecular and Cellular Biology*, *18*(4), 1855–1865. http://doi.org/10.1128/MCB.18.4.1855

Kucukelbir, A., Sigworth, F. J., & Tagare, H. D. (2014). Quantifying the local resolution of cryo-EM density maps. *Nature Methods*, *11*(1), 63–65. http://doi.org/10.1038/nmeth.2727

Kufel, J., Dichtl, B., & Tollervey, D. (1999). Yeast Rnt1p is required for cleavage of the pre-ribosomal RNA in the 3“ ETS but not the 5” ETS. *Rna*, *5*(7), 909–917. http://doi.org/10.1017/s135583829999026x

la Cruz, de, J., Kressler, D., Linder, P., Deloche, O., & Lacombe, T. (2004). The Putative RNA Helicase Dbp6p Functionally Interacts With Rpl3p, Nop8p and the Novel trans-acting Factor Rsa3p During Biogenesis of 60S Ribosomal Subunits in Saccharomyces cerevisiae. *Genetics*, *166*, 1687–1699.

la Cruz, de, J., Kressler, D., Rojo, M., Tollervey, D., & Linder, P. (1998). Spb4p, an essential putative RNA helicase, is required for a late step in the assembly of 60S ribosomal subunits in Saccharomyces cerevisiae. *Rna*, *4*(10), 1268–1281. http://doi.org/10.1017/s1355838298981158

Lafontaine, D. L. J., Riback, J. A., Bascetin, R., & Brangwynne, C. P. (2021). The nucleolus as a multiphase liquid condensate. *Nature Reviews. Molecular Cell Biology*, *22*(3), 165–182. http://doi.org/10.1038/s41580-020-0272-6

Lamanna, A. C., & Karbstein, K. (2009). Nob1 binds the single-stranded cleavage site D at the 3'-end of 18S rRNA with its PIN domain. *Proceedings of the National Academy of Sciences of the United States of America*, *106*(34), 14259–14264. http://doi.org/10.1073/pnas.0905403106

Langmead, B., & Salzberg, S. L. (2012). Fast gapped-read alignment with Bowtie 2. *Nature Methods*, *9*(4), 357–359. http://doi.org/10.1038/nmeth.1923

Lau, B., Cheng, J., Flemming, D., La Venuta, G., Berninghausen, O., Beckmann, R., & Hurt, E. (2021). Structure of the Maturing 90S Pre-ribosome in Association with the RNA Exosome. *Molecular Cell*, *81*(2), 293–303.e4. http://doi.org/10.1016/j.molcel.2020.11.009

Lebaron, S., Froment, C., Fromont-Racine, M., Rain, J.-C., Monsarrat, B., Caizergues-Ferrer, M., & Henry, Y. (2005). The splicing ATPase prp43p is a component of multiple preribosomal particles. *Molecular and Cellular Biology*, *25*(21), 9269–9282. http://doi.org/10.1128/MCB.25.21.9269-9282.2005

Lebaron, S., Schneider, C., van Nues, R. W., Swiatkowska, A., Walsh, D., Böttcher, B., et al. (2012). Proofreading of pre-40S ribosome maturation by a translation initiation factor and 60S subunits. *Nature Structural & Molecular Biology*, *19*(8), 744–753. http://doi.org/10.1038/nsmb.2308

Lebaron, S., Segerstolpe, Å., French, S. L., Dudnakova, T., de lima Alves, F., Granneman, S., et al. (2013). Rrp5 Binding at Multiple Sites Coordinates Pre-rRNA Processing and Assembly. *Molecular Cell*, *52*(5), 707–719. http://doi.org/10.1016/j.molcel.2013.10.017

Leeds, N. B., Small, E. C., Hiley, S. L., Hughes, T. R., & Staley, J. P. (2006). The splicing factor Prp43p, a DEAH box ATPase, functions in ribosome biogenesis. *Molecular and Cellular Biology*, *26*(2), 513–522. http://doi.org/10.1128/MCB.26.2.513-522.2006

Leulliot, N., Bohnsack, M. T., Graille, M., Tollervey, D., & van Tilbeurgh, H. (2008). The yeast ribosome synthesis factor Emg1 is a novel member of the superfamily of alpha/beta knot fold methyltransferases. *Nucleic Acids Research*, *36*(2), 629–639. http://doi.org/10.1093/nar/gkm1074

Lo, K.-Y., Li, Z., Bussiere, C., Bresson, S., Marcotte, E. M., & Johnson, A. W. (2010). Defining the pathway of cytoplasmic maturation of the 60S ribosomal subunit. *Molecular Cell*, *39*(2), 196–208. http://doi.org/10.1016/j.molcel.2010.06.018

Lo, K.-Y., Li, Z., Wang, F., Marcotte, E. M., & Johnson, A. W. (2009). Ribosome stalk assembly requires the dual-specificity phosphatase Yvh1 for the exchange of Mrt4 with P0. *The Journal of Cell Biology*, *186*(6), 849–862. http://doi.org/10.1083/jcb.200904110

Lo, Y.-H., Romes, E. M., Pillon, M. C., Sobhany, M., & Stanley, R. E. (2017). Structural Analysis Reveals Features of Ribosome Assembly Factor Nsa1/WDR74 Important for Localization and Interaction with Rix7/NVL2. *Structure (London, England : 1993)*, *25*(5), 762–772.e4. http://doi.org/10.1016/j.str.2017.03.008

Loewith, R., & Hall, M. N. (2011). Target of rapamycin (TOR) in nutrient signaling and growth control. *Genetics*, *189*(4), 1177–1201. http://doi.org/10.1534/genetics.111.133363

Lorsch, J. R., & Herschlag, D. (1998). The DEAD box protein eIF4A. 2. A cycle of nucleotide and RNA-dependent conformational changes. *Biochemistry*, *37*(8), 2194–2206. http://doi.org/10.1021/bi9724319

Lygerou, Z., Allmang, C., Tollervey, D., & Séraphin, B. (1996). Accurate processing of a eukaryotic precursor ribosomal RNA by ribonuclease MRP in vitro. *Science (New York, N.Y.)*, *272*(5259), 268–270. http://doi.org/10.1126/science.272.5259.268

Ma, C., Wu, S., Li, N., Chen, Y., Yan, K., Li, Z., et al. (2017). Structural snapshot of cytoplasmic pre-60S ribosomal particles bound by Nmd3, Lsg1, Tif6 and Reh1. *Nature Structural & Molecular Biology*, *24*(3), 214–220. http://doi.org/10.1038/nsmb.3364

Madeira, F., Park, Y. M., Lee, J., Buso, N., Gur, T., Madhusoodanan, N., et al. (2019). The EMBL-EBI search and sequence analysis tools APIs in 2019. *Nucleic Acids Research*, *47*(W1), W636–W641. http://doi.org/10.1093/nar/gkz268

Mastronarde, D. N. (2005). Automated electron microscope tomography using robust prediction of specimen movements. *Journal of Structural Biology*, *152*(1), 36–51. http://doi.org/10.1016/j.jsb.2005.07.007

Meyer, A. E., Hoover, L. A., & Craig, E. A. (2010). The cytosolic J-protein, Jjj1, and Rei1 function in the removal of the pre-60 S subunit factor Arx1. *The Journal of Biological Chemistry*, *285*(2), 961–968. http://doi.org/10.1074/jbc.M109.038349

Meyer, A. E., Hung, N.-J., Yang, P., Johnson, A. W., & Craig, E. A. (2007). The specialized cytosolic J-protein, Jjj1, functions in 60S ribosomal subunit biogenesis. *Proceedings of the National Academy of Sciences*, *104*(5), 1558–1563. http://doi.org/10.1073/pnas.0610704104

Miller, O. L., & Beatty, B. R. (1969). Visualization of nucleolar genes. *Science (New York, N.Y.)*, *164*(3882), 955–957. http://doi.org/10.1126/science.164.3882.955

Mitchell, P. (2010). Rrp47 and the function of the Sas10/C1D domain. *Biochemical Society Transactions*, *38*(4), 1088–1092. http://doi.org/10.1042/BST0381088

Mitterer, V., Shayan, R., Ferreira-Cerca, S., Murat, G., Enne, T., Rinaldi, D., et al. (2019). Conformational proofreading of distant 40S ribosomal subunit maturation events by a long-range communication mechanism. *Nature Communications*, *10*(1), 2754–15. http://doi.org/10.1038/s41467-019-10678-z

Moeller, von, H., Basquin, C., & Conti, E. (2009). The mRNA export protein DBP5 binds RNA and the cytoplasmic nucleoporin NUP214 in a mutually exclusive manner. *Nature Structural & Molecular Biology*, *16*(3), 247–254. http://doi.org/10.1038/nsmb.1561

Moriggi, G., Nieto, B., & Dosil, M. (2014). Rrp12 and the Exportin Crm1 participate in late assembly events in the nucleolus during 40S ribosomal subunit biogenesis. *PLOS Genetics*, *10*(12), e1004836. http://doi.org/10.1371/journal.pgen.1004836

Mougey, E. B., O'Reilly, M., Osheim, Y., Miller, O. L., Beyer, A., & Sollner-Webb, B. (1993). The terminal balls characteristic of eukaryotic rRNA transcription units in chromatin spreads are rRNA processing complexes. *Genes & Development*, *7*(8), 1609–1619. http://doi.org/10.1101/gad.7.8.1609

Nakane, T., & Scheres, S. H. W. (2021). Multi-body Refinement of Cryo-EM Images in RELION. *Methods in Molecular Biology (Clifton, N.J.)*, *2215*, 145–160. http://doi.org/10.1007/978-1-0716-0966-8_7

Nielsen, K. H., Chamieh, H., Andersen, C. B. F., Fredslund, F., Hamborg, K., Le Hir, H., & Andersen, G. R. (2009). Mechanism of ATP turnover inhibition in the EJC. *Rna*, *15*(1), 67–75. http://doi.org/10.1261/rna.1283109

Noller, H. F., Hoffarth, V., & Zimniak, L. (1992). Unusual resistance of peptidyl transferase to protein extraction procedures. *Science (New York, N.Y.)*, *256*(5062), 1416–1419. http://doi.org/10.1126/science.1604315

O'Day, C. L., Chavanikamannil, F., & Abelson, J. (1996). 18S rRNA processing requires the RNA helicase-like protein Rrp3. *Nucleic Acids Research*, *24*(16), 3201–3207. http://doi.org/10.1093/nar/24.16.3201

Palade, G. E. (1955). A small particulate component of the cytoplasm. *The Journal of Biophysical and Biochemical Cytology*, *1*(1), 59–68. http://doi.org/10.1083/jcb.1.1.59

Peña, C., Hurt, E., & Panse, V. G. (2017). Eukaryotic ribosome assembly, transport and quality control. *Nature Structural & Molecular Biology*, *24*(9), 689–699. http://doi.org/10.1038/nsmb.3454

Pertschy, B., Saveanu, C., Zisser, G., Lebreton, A., Tengg, M., Jacquier, A., et al. (2007). Cytoplasmic recycling of 60S preribosomal factors depends on the AAA protein Drg1. *Molecular and Cellular Biology*, *27*(19), 6581–6592. http://doi.org/10.1128/MCB.00668-07

Pertschy, B., Schneider, C., Gnädig, M., Schäfer, T., Tollervey, D., & Hurt, E. (2009). RNA helicase Prp43 and its co-factor Pfa1 promote 20 to 18 S rRNA processing catalyzed by the endonuclease Nob1. *The Journal of Biological Chemistry*, *284*(50), 35079–35091. http://doi.org/10.1074/jbc.M109.040774

Pettersen, E. F., Goddard, T. D., Huang, C. C., Couch, G. S., Greenblatt, D. M., Meng, E. C., & Ferrin, T. E. (2004). UCSF Chimera--a visualization system for exploratory research and analysis. *Journal of Computational Chemistry*, *25*(13), 1605–1612. http://doi.org/10.1002/jcc.20084

Pillon, M. C., Sobhany, M., Borgnia, M. J., Williams, J. G., & Stanley, R. E. (2017). Grc3 programs the essential endoribonuclease Las1 for specific RNA cleavage. *Proceedings of the National Academy of Sciences of the United States of America*, *114*(28), E5530–E5538. http://doi.org/10.1073/pnas.1703133114

Powers, T., & Walter, P. (1999). Regulation of ribosome biogenesis by the rapamycin-sensitive TOR-signaling pathway in Saccharomyces cerevisiae. *Molecular Biology of the Cell*, *10*(4), 987–1000. http://doi.org/10.1091/mbc.10.4.987

Punjani, A., Rubinstein, J. L., Fleet, D. J., & Brubaker, M. A. (2017). cryoSPARC: algorithms for rapid unsupervised cryo-EM structure determination. *Nature Methods*, *14*(3), 290–296. http://doi.org/10.1038/nmeth.4169

Rabl, J., Leibundgut, M., Ataide, S. F., Haag, A., & Ban, N. (2011). Crystal structure of the eukaryotic 40S ribosomal subunit in complex with initiation factor 1. *Science (New York, N.Y.)*, *331*(6018), 730–736. http://doi.org/10.1126/science.1198308

Reiter, A., Steinbauer, R., Philippi, A., Gerber, J., Tschochner, H., Milkereit, P., & Griesenbeck, J. (2011). Reduction in ribosomal protein synthesis is sufficient to explain major effects on ribosome production after short-term TOR inactivation in Saccharomyces cerevisiae. *Molecular and Cellular Biology*, *31*(4), 803–817. http://doi.org/10.1128/MCB.01227-10

Rhine, K., Vidaurre, V., & Myong, S. (2020). RNA Droplets. *Annual Review of Biophysics*, *49*, 247–265. http://doi.org/10.1146/annurev-biophys-052118-115508

Ripmaster, T. L., Vaughn, G. P., & Woolford, J. L. (1992). A putative ATP-dependent RNA helicase involved in Saccharomyces cerevisiae ribosome assembly. *Proceedings of the National Academy of Sciences*, *89*(23), 11131–11135. http://doi.org/10.1073/pnas.89.23.11131

Rohde, J., Heitman, J., & Cardenas, M. E. (2001). The TOR kinases link nutrient sensing to cell growth. *The Journal of Biological Chemistry*, *276*(13), 9583–9586. http://doi.org/10.1074/jbc.R000034200

Rohou, A., & Grigorieff, N. (2015). CTFFIND4: Fast and accurate defocus estimation from electron micrographs. *Journal of Structural Biology*, *192*(2), 216–221. http://doi.org/10.1016/j.jsb.2015.08.008

Rosado, I. V. (2004). Npa1p is an essential trans-acting factor required for an early step in the assembly of 60S ribosomal subunits in Saccharomyces cerevisiae. *Rna*, *10*(7), 1073–1083. http://doi.org/10.1261/rna.7340404

Rosado, I. V., Dez, C., Lebaron, S., Caizergues-Ferrer, M., Henry, Y., & la Cruz, de, J. (2007). Characterization of Saccharomyces cerevisiae Npa2p (Urb2p) Reveals a Low-Molecular-Mass Complex Containing Dbp6p, Npa1p (Urb1p), Nop8p, and Rsa3p Involved in Early Steps of 60S Ribosomal Subunit Biogenesis. *Molecular and Cellular Biology*, *27*(4), 1207–1221. http://doi.org/10.1128/MCB.01523-06

Roychowdhury, A., Joret, C., Bourgeois, G., Heurgué-Hamard, V., Lafontaine, D. L. J., & Graille, M. (2019). The DEAH-box RNA helicase Dhr1 contains a remarkable carboxyl terminal domain essential for small ribosomal subunit biogenesis. *Nucleic Acids Research*, *47*(14), 7548–7563. http://doi.org/10.1093/nar/gkz529

Samatanga, B., & Klostermeier, D. (2014). DEAD-box RNA helicase domains exhibit a continuum between complete functional independence and high thermodynamic coupling in nucleotide and RNA duplex recognition. *Nucleic Acids Research*, *42*(16), 10644–10654. http://doi.org/10.1093/nar/gku747

Sanghai, Z. A., Miller, L., Molloy, K. R., Barandun, J., Hunziker, M., Chaker-Margot, M., et al. (2018). Modular assembly of the nucleolar pre-60S ribosomal subunit. *Nature*, *556*(7699), 126–129. http://doi.org/10.1038/nature26156

Sardana, R., Liu, X., Granneman, S., Zhu, J., Gill, M., Papoulas, O., et al. (2015). The DEAH-box Helicase Dhr1 Dissociates U3 from the Pre-rRNA to Promote Formation of the Central Pseudoknot. *PLoS Biology*, *13*(2), e1002083–25. http://doi.org/10.1371/journal.pbio.1002083

Sardana, R., White, J. P., & Johnson, A. W. (2013). The rRNA methyltransferase Bud23 shows functional interaction with components of the SSU processome and RNase MRP. *Rna*, *19*(6), 828–840. http://doi.org/10.1261/rna.037671.112

Sardana, R., Zhu, J., Gill, M., & Johnson, A. W. (2014). Physical and functional interaction between the methyltransferase Bud23 and the essential DEAH-box RNA helicase Ecm16. *Molecular and Cellular Biology*, *34*(12), 2208–2220. http://doi.org/10.1128/MCB.01656-13

Sarkar, A., Pech, M., Thoms, M., Beckmann, R., & Hurt, E. (2016). Ribosome-stalk biogenesis is coupled with recruitment of nuclear-export factor to the nascent 60S subunit. *Nature Structural & Molecular Biology*, *23*(12), 1074–1082. http://doi.org/10.1038/nsmb.3312

Saveanu, C., Bienvenu, D., Namane, A., Gleizes, P. E., Gas, N., Jacquier, A., & Fromont-Racine, M. (2001). Nog2p, a putative GTPase associated with pre-60S subunits and required for late 60S maturation steps. *The EMBO Journal*, *20*(22), 6475–6484. http://doi.org/10.1093/emboj/20.22.6475

Scaiola, A., Peña, C., Weisser, M., Böhringer, D., Leibundgut, M., Klingauf-Nerurkar, P., et al. (2018). Structure of a eukaryotic cytoplasmic pre-40S ribosomal subunit. *The EMBO Journal*, *37*(7), e98499. http://doi.org/10.15252/embj.201798499

Schuller, J. M., Falk, S., Fromm, L., Hurt, E., & Conti, E. (2018). Structure of the nuclear exosome captured on a maturing preribosome. *Science (New York, N.Y.)*, *360*(6385), 219–222. http://doi.org/10.1126/science.aar5428

Seiser, R. M., Sundberg, A. E., Wollam, B. J., Zobel-Thropp, P., Baldwin, K., Spector, M. D., & Lycan, D. E. (2006). Ltv1 is required for efficient nuclear export of the ribosomal small subunit in Saccharomyces cerevisiae. *Genetics*, *174*(2), 679–691. http://doi.org/10.1534/genetics.106.062117

Sengoku, T., Nureki, O., Nakamura, A., Kobayashi, S., & Yokoyama, S. (2006). Structural basis for RNA unwinding by the DEAD-box protein Drosophila Vasa. *Cell*, *125*(2), 287–300. http://doi.org/10.1016/j.cell.2006.01.054

Sharma, S., Langhendries, J.-L., Watzinger, P., Kötter, P., Entian, K.-D., & Lafontaine, D. L. J. (2015). Yeast Kre33 and human NAT10 are conserved 18S rRNA cytosine acetyltransferases that modify tRNAs assisted by the adaptor Tan1/THUMPD1. *Nucleic Acids Research*, *43*(4), 2242–2258. http://doi.org/10.1093/nar/gkv075

Sharma, S., Yang, J., van Nues, R., Watzinger, P., Kötter, P., Lafontaine, D. L. J., et al. (2017). Specialized box C/D snoRNPs act as antisense guides to target RNA base acetylation. *PLOS Genetics*, *13*(5), e1006804. http://doi.org/10.1371/journal.pgen.1006804

Shi, Y., Fernandez-Martinez, J., Tjioe, E., Pellarin, R., Kim, S. J., Williams, R., et al. (2014). Structural characterization by cross-linking reveals the detailed architecture of a coatomer-related heptameric module from the nuclear pore complex. *Molecular & Cellular Proteomics : MCP*, *13*(11), 2927–2943. http://doi.org/10.1074/mcp.M114.041673

Shi, Y., Pellarin, R., Fridy, P. C., Fernandez-Martinez, J., Thompson, M. K., Li, Y., et al. (2015). A strategy for dissecting the architectures of native macromolecular assemblies. *Nature Methods*, *12*(12), 1135–1138. http://doi.org/10.1038/nmeth.3617

Silverman, E. J., Maeda, A., Wei, J., Smith, P., Beggs, J. D., & Lin, R.-J. (2004). Interaction between a G-patch protein and a spliceosomal DEXD/H-box ATPase that is critical for splicing. *Molecular and Cellular Biology*, *24*(23), 10101–10110. http://doi.org/10.1128/MCB.24.23.10101-10110.2004

Singleton, M. R., Dillingham, M. S., & Wigley, D. B. (2007). Structure and Mechanism of Helicases and Nucleic Acid Translocases. *Annual Review of Biochemistry*, *76*(1), 23–50. http://doi.org/10.1146/annurev.biochem.76.052305.115300

Sloan, K. E., & Bohnsack, M. T. (2018). Unravelling the Mechanisms of RNA Helicase Regulation. *Trends in Biochemical Sciences*, *43*(4), 237–250. http://doi.org/10.1016/j.tibs.2018.02.001

Sloan, K. E., Warda, A. S., Sharma, S., Entian, K.-D., Lafontaine, D. L. J., & Bohnsack, M. T. (2017). Tuning the ribosome: The influence of rRNA modification on eukaryotic ribosome biogenesis and function. *RNA Biology*, *14*(9), 1138–1152. http://doi.org/10.1080/15476286.2016.1259781

Soltanieh, S., Lapensée, M., & Dragon, F. (2014). Nucleolar proteins Bfr2 and Enp2 interact with DEAD-box RNA helicase Dbp4 in two different complexes. *Nucleic Acids Research*, *42*(5), 3194–3206. http://doi.org/10.1093/nar/gkt1293

Strunk, B. S., Novak, M. N., Young, C. L., & Karbstein, K. (2012). A translation-like cycle is a quality control checkpoint for maturing 40S ribosome subunits. *Cell*, *150*(1), 111–121. http://doi.org/10.1016/j.cell.2012.04.044

Studer, M. K., Ivanović, L., Weber, M. E., Marti, S., & Jonas, S. (2020). Structural basis for DEAH-helicase activation by G-patch proteins. *Proceedings of the National Academy of Sciences of the United States of America*, *117*(13), 7159–7170. http://doi.org/10.1073/pnas.1913880117

Sun, Q., Zhu, X., Qi, J., An, W., Lan, P., Tan, D., et al. (2017). Molecular architecture of the 90S small subunit pre-ribosome. *eLife*, *6*. http://doi.org/10.7554/eLife.22086

Talkish, J., Biedka, S., Jakovljevic, J., Zhang, J., Tang, L., Strahler, J. R., et al. (2016). Disruption of ribosome assembly in yeast blocks cotranscriptional pre-rRNA processing and affects the global hierarchy of ribosome biogenesis. *Rna*, *22*(6), 852–866. http://doi.org/10.1261/rna.055780.115

Tang, G., Peng, L., Baldwin, P. R., Mann, D. S., Jiang, W., Rees, I., & Ludtke, S. J. (2007). EMAN2: an extensible image processing suite for electron microscopy. *Journal of Structural Biology*, *157*(1), 38–46. http://doi.org/10.1016/j.jsb.2006.05.009

Tange, T. Ø., Nott, A., & Moore, M. J. (2004). The ever-increasing complexities of the exon junction complex. *Current Opinion in Cell Biology*, *16*(3), 279–284. http://doi.org/10.1016/j.ceb.2004.03.012

Tartakoff, A. M., Chen, L., Raghavachari, S., Gitiforooz, D., Dhinakaran, A., Ni, C.-L., et al. (2021). The nucleolus as a polarized coaxial cable in which the rDNA axis is surrounded by dynamic subunit-specific phases. *Current Biology : CB*. http://doi.org/10.1016/j.cub.2021.03.041

Tauchert, M. J., Fourmann, J.-B., Lührmann, R., & Ficner, R. (2017). Structural insights into the mechanism of the DEAH-box RNA helicase Prp43. *eLife*, *6*, 762. http://doi.org/10.7554/eLife.21510

Theissen, B., Karow, A. R., Köhler, J., Gubaev, A., & Klostermeier, D. (2008). Cooperative binding of ATP and RNA induces a closed conformation in a DEAD box RNA helicase. *Proceedings of the National Academy of Sciences of the United States of America*, *105*(2), 548–553. http://doi.org/10.1073/pnas.0705488105

Thomas, S. R., Keller, C. A., Szyk, A., Cannon, J. R., & Laronde-Leblanc, N. A. (2011). Structural insight into the functional mechanism of Nep1/Emg1 N1-specific pseudouridine methyltransferase in ribosome biogenesis. *Nucleic Acids Research*, *39*(6), 2445–2457.

Thoms, M., Thomson, E., Baßler, J., Gnädig, M., Griesel, S., & Hurt, E. (2015). The Exosome Is Recruited to RNA Substrates through Specific Adaptor Proteins. *Cell*, *162*(5), 1029–1038. http://doi.org/10.1016/j.cell.2015.07.060

Tomecki, R., Labno, A., Drazkowska, K., Cysewski, D., & Dziembowski, A. (2015). hUTP24 is essential for processing of the human rRNA precursor at site A1, but not at site A0. *RNA Biology*, *12*(9), 1010–1029. http://doi.org/10.1080/15476286.2015.1073437

Torreira, E., Louro, J. A., Pazos, I., González-Polo, N., Gil-Carton, D., Duran, A. G., et al. (2017). The dynamic assembly of distinct RNA polymerase I complexes modulates rDNA transcription. *eLife*, *6*. http://doi.org/10.7554/eLife.20832

Upadhya, R., Lee, J., & Willis, I. M. (2002). Maf1 is an essential mediator of diverse signals that repress RNA polymerase III transcription. *Molecular Cell*, *10*(6), 1489–1494. http://doi.org/10.1016/s1097-2765(02)00787-6

Venema, J., & Tollervey, D. (1996). RRP5 is required for formation of both 18S and 5.8S rRNA in yeast. *The EMBO Journal*, *15*(20), 5701–5714.

Walbott, H., Mouffok, S., Capeyrou, R., Lebaron, S., Humbert, O., van Tilbeurgh, H., et al. (2010). Prp43p contains a processive helicase structural architecture with a specific regulatory domain. *The EMBO Journal*, *29*(13), 2194–2204. http://doi.org/10.1038/emboj.2010.102

Warkocki, Z., Schneider, C., Mozaffari-Jovin, S., Schmitzová, J., Höbartner, C., Fabrizio, P., & Lührmann, R. (2015). The G-patch protein Spp2 couples the spliceosome-stimulated ATPase activity of the DEAH-box protein Prp2 to catalytic activation of the spliceosome. *Genes & Development*, *29*(1), 94–107. http://doi.org/10.1101/gad.253070.114

Warner, J. R. (1999). The economics of ribosome biosynthesis in yeast. *Trends in Biochemical Sciences*, 437–440.

Weaver, P. L., Sun, C., & Chang, T. H. (1997). Dbp3p, a putative RNA helicase in Saccharomyces cerevisiae, is required for efficient pre-rRNA processing predominantly at site A3. *Molecular and Cellular Biology*, *17*(3), 1354–1365. http://doi.org/10.1128/mcb.17.3.1354

Wegierski, T., Billy, E., Nasr, F., & Filipowicz, W. (2001). Bms1p, a G-domain-containing protein, associates with Rcl1p and is required for 18S rRNA biogenesis in yeast. *Rna*, *7*(9), 1254–1267. http://doi.org/10.1017/s1355838201012079

Wegrecki, M., Rodríguez-Galán, O., la Cruz, de, J., & Bravo, J. (2015). The structure of Erb1-Ytm1 complex reveals the functional importance of a high-affinity binding between two β-propellers during the assembly of large ribosomal subunits in eukaryotes. *Nucleic Acids Research*, *43*(22), 11017–11030. http://doi.org/10.1093/nar/gkv1043

Weis, F., Giudice, E., Churcher, M., Jin, L., Hilcenko, C., Wong, C. C., et al. (2015). Mechanism of eIF6 release from the nascent 60S ribosomal subunit. *Nature Structural & Molecular Biology*, *22*(11), 914–919. http://doi.org/10.1038/nsmb.3112

Wells, G. R., Weichmann, F., Colvin, D., Sloan, K. E., Kudla, G., Tollervey, D., et al. (2016). The PIN domain endonuclease Utp24 cleaves pre-ribosomal RNA at two coupled sites in yeast and humans. *Nucleic Acids Research*, *44*(11), 5399–5409. http://doi.org/10.1093/nar/gkw213

White, J., Li, Z., Sardana, R., Bujnicki, J. M., Marcotte, E. M., & Johnson, A. W. (2008). Bud23 methylates G1575 of 18S rRNA and is required for efficient nuclear export of pre-40S subunits. *Molecular and Cellular Biology*, *28*(10), 3151–3161. http://doi.org/10.1128/MCB.01674-07

Woolford, J. L., & Baserga, S. J. (2013). Ribosome biogenesis in the yeast Saccharomyces cerevisiae. *Genetics*, *195*(3), 643–681. http://doi.org/10.1534/genetics.113.153197

Wu, S., Tutuncuoglu, B., Yan, K., Brown, H., Zhang, Y., Tan, D., et al. (2016). Diverse roles of assembly factors revealed by structures of late nuclear pre-60S ribosomes. *Nature*, *534*(7605), 133–137. http://doi.org/10.1038/nature17942

Yang, B., Wu, Y.-J., Zhu, M., Fan, S.-B., Lin, J., Zhang, K., et al. (2012a). Identification of cross-linked peptides from complex samples. *Nature Methods*, *9*(9), 904–906. http://doi.org/10.1038/nmeth.2099

Yang, Z., Fang, J., Chittuluru, J., Asturias, F. J., & Penczek, P. A. (2012b). Iterative stable alignment and clustering of 2D transmission electron microscope images. *Structure (London, England : 1993)*, *20*(2), 237–247. http://doi.org/10.1016/j.str.2011.12.007

Yao, R.-W., Xu, G., Wang, Y., Shan, L., Luan, P.-F., Wang, Y., et al. (2019). Nascent Pre-rRNA Sorting via Phase Separation Drives the Assembly of Dense Fibrillar Components in the Human Nucleolus. *Molecular Cell*, *76*(5), 767–783.e11.

Yusupov, M. M., Yusupova, G. Z., Baucom, A., Lieberman, K., Earnest, T. N., Cate, J. H., & Noller, H. F. (2001). Crystal structure of the ribosome at 5.5 A resolution. *Science (New York, N.Y.)*, *292*(5518), 883–896. http://doi.org/10.1126/science.1060089

Zagorski, J., Tollervey, D., & Fournier, M. J. (1988). Characterization of an SNR gene locus in Saccharomyces cerevisiae that specifies both dispensible and essential small nuclear RNAs. *Molecular and Cellular Biology*, *8*(8), 3282–3290. http://doi.org/10.1128/mcb.8.8.3282

Zagulski, M., Kressler, D., Bécam, A.-M., Rytka, J., & Herbert, C. J. (2003). Mak5p, which is required for the maintenance of the M1 dsRNA virus, is encoded by the yeast ORF YBR142w and is involved in the biogenesis of the 60S subunit of the ribosome. *Molecular Genetics and Genomics : MGG*, *270*(3), 216–224. http://doi.org/10.1007/s00438-003-0913-4

Zemp, I., Wild, T., O'Donohue, M.-F., Wandrey, F., Widmann, B., Gleizes, P.-E., & Kutay, U. (2009). Distinct cytoplasmic maturation steps of 40S ribosomal subunit precursors require hRio2. *The Journal of Cell Biology*, *185*(7), 1167–1180. http://doi.org/10.1083/jcb.200904048

Zhang, Y., Smith, A. D., Renfrow, M. B., & Schneider, D. A. (2010). The RNA polymerase-associated factor 1 complex (Paf1C) directly increases the elongation rate of RNA polymerase I and is required for efficient regulation of rRNA synthesis. *The Journal of Biological Chemistry*, *285*(19), 14152–14159. http://doi.org/10.1074/jbc.M110.115220

Zheng, S. Q., Palovcak, E., Armache, J.-P., Verba, K. A., Cheng, Y., & Agard, D. A. (2017). MotionCor2: anisotropic correction of beam-induced motion for improved cryo-electron microscopy. *Nature Methods*, *14*(4), 331–332. http://doi.org/10.1038/nmeth.4193

Zhou, D., Zhu, X., Zheng, S., Tan, D., Dong, M.-Q., & Ye, K. (2018). Cryo-EM structure of an early precursor of large ribosomal subunit reveals a half-assembled intermediate. *Protein & Cell*, 1–11. http://doi.org/10.1007/s13238-018-0526-7

Zhu, J., Liu, X., Anjos, M., Correll, C. C., & Johnson, A. W. (2016). Utp14 Recruits and Activates the RNA Helicase Dhr1 To Undock U3 snoRNA from the Preribosome. *Molecular and Cellular Biology*, *36*(6), 965–978. http://doi.org/10.1128/MCB.00773-15